



UNIVERSITÉ  
CÔTE D'AZUR

ACADEMY OF EXCELLENCE

COMPLEX SYSTEMS

Proceedings of the  
**Complex Systems**

Academy of Excellence

2018



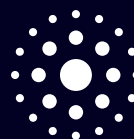
Edited by

M. Argentina, S. Barland, P. Reynaud-Bouret, F. Cauneau, K. Guillouzouic, U. Kuhl, T. Passot, F. Planchon



INITIATIVE D'EXCELLENCE

**UCA** J.E.D.I.  
UNIVERSITÉ CÔTE D'AZUR





Proceedings of the  
Complex Systems  
Academy of Excellence



# Proceedings of the Complex Systems Academy of Excellence



Edited by

M. Argentina, S. Barland, P. Reynaud-Bouret, F. Cauneau,  
K. Guillouzouic, U. Kuhl, T. Passot, F. Planchon

December 2018

Publisher: Université Côte d'Azur - Complex Systems Academy of Excellence, Nice  
Printed by: Centre de Production Numérique Universitaire - Université Nice Sophia Antipolis  
Avenue Joseph Vallot, 06103 Nice, France  
First published: December 2018  
Registration: December 2018  
©Université Côte d'Azur - All rights reserved  
**Print ISBN:** 978-2-9565650-0-0  
**ePDF ISBN:** 978-2-9565650-1-7

# Contents

<b>Preface</b> .....	ix
<b>Polynomial interpolation in higher dimensions</b> .....	1
Alexandru Dimca	
<b>Compressions of a polycarbonate honeycomb</b> .....	9
André Galligo, Jean Rajchenbach and Bernard Rousselet	
<b>Measurement of temperature and thermal gradients using fibre optic long period gratings</b> .....	17
Frédéric J Lesage	
<b>Nudging-based observers for geophysical data assimilation and joint state-parameters estimation</b> .....	25
Samira Amraoui, Didier Auroux, Jacques Blum, Blaise Faugeras	
<b>The retina: a fascinating object of study for a physicist</b> .....	35
Bruno Cessac	
<b>Modeling and computation of a liquid-vapor bubble formation</b> .....	45
André Galligo, Frédéric Lesage, Sebastian Minjeaud	
<b>New paradigms in nuclear human decorporation using macromolecular systems</b> .....	53
Laurane Léost, Florian Lahrouch, Christophe Den Auwer, Christophe Di Giorgio and coworkers.	
<b>Collective behaviours of light and matter</b> .....	59
Thibaut Flottat, Frédéric Hébert and George Batrouni	

<b>Extreme and rare events in hydrodynamical and optical systems</b> . . . . .	69
Giovanna Tissoni and Eric Simonnet	
<b>Complex molecule synthesis made easy</b> . . . . .	77
Nelli Elizarov, Pascal D. Giorgi, Alexandra Yeromina, Sylvain Antoniotti	
<b>Chaotic reverberation chambers for electromagnetic compatibility</b> . . .	87
Olivier Legrand, Ulrich Kuhl, Fabrice Mortessagne, Khalid Oubaha and Martin Richter	
<b>Collisional relaxation of long range interacting systems of particles</b> . .	95
Fernanda P. C. Benetti and Bruno Marcos	
<b>Optimal control of slow-fast mechanical systems</b> . . . . .	105
Jean-Baptiste Caillau, Lamberto Dell’Elce, Jean-Baptiste Pomet and Jérémy Rouot	
<b>Light-induced self-organization in cold atomic clouds</b> . . . . .	117
Guillaume Labeyrie and Robin Kaiser	
<b>Eco-evolutionary dynamics in complex ecological communities</b> . . . . .	123
Flora Aubree, Vincent Calcagno	
<b>The Nice Cube (Nice<sup>3</sup>) nanosatellite project</b> . . . . .	133
F. Millour, S. Ottogalli, M. Maamri, A. Stibbe, F. Ferrero, L. Rolland, S. Rebeyrolle, A. Marcotto, K. Agabi, M. Beaulieu, M. Benabdesselam, J.-B. Caillau, F. Cauneau, L. Deneire, F. Mady, D. Mary, A. Memin, G. Metris, J.-B. Pomet, O. Preis, R. Staraj, E. Ait Lachgar, D. Baltazar, G. Bao, M. Deroo, B. Gieudes, M. Jiang, T. Livio de Miranda Pinto Filho, M. Languery, O. Petiot, A. Thevenon	
<b>Modelling complex systems in Archaeology: general issues and first insights from the ModelAnSet project</b> . . . . .	146
Frédérique Bertocello, Marie-Jeanne Ouriachi, Célia Da Costa Pereira, Andrea Tettamanzi, Louise Purdue, Daniel Contreras, Dennis Fox, Nobuyuki Hanaki, Rami Ajroud, Jérémy Lefebvre	
<b>Enhancing magnetic separation of nanoparticles</b> . . . . .	155
Pavel Kuzhir, Hinda Ezzaier, Jessica A. Marins, Cécilia Magnet, Yaroslova Izmaylov, Cyrille Claudet	
<b>Semiconductor lasers: coherence and localized states</b> . . . . .	165
Stéphane Barland, Massimo Giudici, Gian Luca Lippi	
<b>Index of keywords</b> . . . . .	175

**Index of contributors** ..... 177



## Preface

*With the view that a complex system includes “any object whose behavior as a whole is not determined in a simple way by the behavior of its individual constituents”, the Complex Systems Academy covers a broad spectrum of scientific activities that often cross conventional scientific fields.*

*Following the first two years of existence of the Academy, this edition of the Proceedings of the Complex Systems Academy of Excellence was prepared in the wake of the first “Complex Days” Academy-wide meeting, which took place in Nice in January 2018. As such, this book is a non-exclusive window into the many research topics that are currently addressed at the Université Côte d’Azur within the scope of the Academy. Far from being an exhaustive list or final word, it is only a glimpse of the ongoing research at a very precise point in time.*

*Still, as will be evident to the reader, many topics are discussed in the following chapters, ranging from mathematics and physics to archeology, chemistry and space science or ecology and biophysics. Can such a diversity be categorized? Would it even be really productive at the time of writing? Inspired by one of the most emblematic phenomena encountered in complex systems, namely “self-organization”, the organizers of the meeting and the editors of this compendium deliberately decided *not* to categorize. Instead, the choice was to mix topics as much as possible and to leave the reader to construct from the parts his or her own vision of the whole, free from disciplinary silos.*

*The editors of this volume thank all the participants of the meeting, with special thanks to the contributing authors of the Proceedings.*

---



# Polynomial interpolation in higher dimensions

Alexandru Dimca

**Abstract** We describe a recent advance in the theory of interpolation in the plane, based on the theory of line arrangements in the complex projective plane.

## 1 Interpolation in dimensions one and two

### 1.1 Lagrange interpolation

We denote by  $\mathbb{R}$  the field of real numbers and by  $\mathbb{C}$  the field of complex numbers. Let  $p_1, \dots, p_n$  be  $n$  real numbers, thought of as  $n$  points on the real line.

Assume that each point  $p_i$  has an associated number  $c_i \in \mathbb{R}$ , thought of as the result of a measurement effectuated at the point  $p_i$ , for  $i = 1, 2, \dots, n$ , of a physical entity of interest to us, e.g., temperature, pressure, or density of a substance. Let  $S = \{p_1, p_2, \dots, p_n\}$  be the set of these  $n$  points, and

$$f : S \rightarrow \mathbb{R}$$

the function defined by  $f(p_i) = c_i$  for  $i = 1, 2, \dots, n$ . In order to move from experiment to theory, we would like to find a formula for this function  $f$ . The most natural idea is to look for a polynomial  $P(x)$  of minimal possible degree such that one has

---

Alexandru Dimca

Université Côte d'Azur, CNRS, LJAD, France, e-mail: [dimca@unice.fr](mailto:dimca@unice.fr)

$$f(p_i) = P(p_i) \text{ for all } i = 1, 2, \dots, n.$$

The hope is that this polynomial will in fact satisfy  $f(t) = P(t)$  for any real number  $t$ , and hence our discovered formula would allow us to make predictions as well.

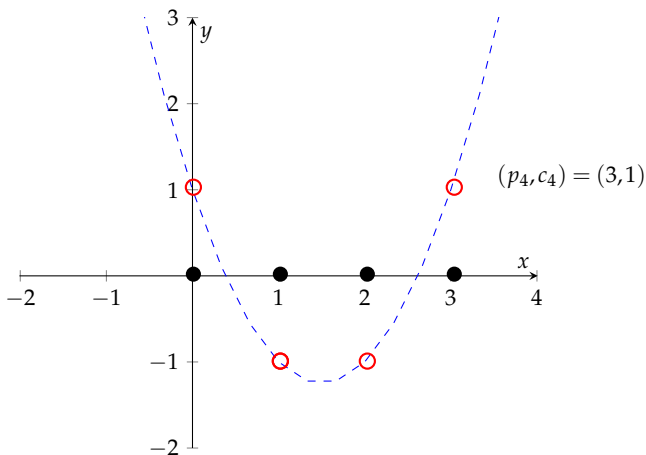


**Fig. 1** The  $n = 4$  points  $(p_i, c_i)$  are on the parabola  $y = P(x)$ , with  $P(x) = x^2 - 3x + 1$ .

The following result was first published by Waring in 1779, rediscovered by Euler in 1783, and published by Lagrange in 1795.

**Theorem 1.** For any  $n$  distinct real numbers  $p_i, i = 1, 2, \dots, n$ , and any given  $n$  values  $c_i, i = 1, 2, \dots, n$ , there is a unique polynomial  $P(x)$  of degree at most  $n - 1$ , such that  $P(p_i) = c_i$  for all  $i = 1, 2, \dots, n$ .

To give a formula for  $P(x)$ , consider, for any  $i = 1, 2, \dots, n$ , the degree  $n - 1$  polynomial

$$Q_i(x) = \frac{\prod_{j=1, n; j \neq i} (x - p_j)}{\prod_{j=1, n; j \neq i} (p_i - p_j)},$$

and note that  $Q_i(p_i) = 1$  and  $Q_i(p_k) = 0$  for any  $k \neq i$ . With this notation one has

$$P(x) = \sum_{i=1, n} c_i Q_i(x).$$

Consider the vector space of polynomials of degree at most  $d$ , denoted by  $\mathbb{R}[x]_{\leq d}$ , and the linear map given by evaluation

$$\epsilon_d : \mathbb{R}[x]_{\leq d} \rightarrow \mathbb{R}^S = \mathbb{R}^n, \quad \epsilon(Q)(p_i) = Q(p_i),$$

for any  $i = 1, 2, \dots, n$ , where  $\mathbb{R}^S$  denotes the vector space of all functions  $S \rightarrow \mathbb{R}$ . The above results say that  $\epsilon_d$  is injective if and only if  $d \leq n - 1$ , and  $\epsilon_d$  is surjective if and only if  $d \geq n - 1$ . Such results are true over any field:  $\mathbb{R}$ ,  $\mathbb{C}$  or even finite fields.

## 1.2 Interpolation in dimension 2

Let now  $p_i = (x_i, y_i)$  for  $i = 1, 2, \dots, n$  be  $n$  points in the plane  $\mathbb{R}^2$ . Assume each point has an associated value  $c_i \in \mathbb{R}$ , thought of as the result of a measurement at the point  $p_i$ . Let  $S = \{p_1, p_2, \dots, p_n\}$  be the set of these points, consider the associated function  $f : S \rightarrow \mathbb{R}$  given by  $f(p_i) = c_i$  and look for the minimal degree  $d$  such that there is a polynomial  $Q \in \mathbb{R}[x, y]$  of degree  $d$  satisfying

$$f(p_i) = Q(x_i, y_i) \text{ for all } i = 1, 2, \dots, n.$$

This is the old question, but the setting is new: the answer now depends on the position of the points  $p_i$  in the plane.

*Example 1 (3 points in the plane).* If the 3 points  $p_1, p_2$  and  $p_3$  are not collinear, then we can take  $d = 1$ . Indeed, as above, we can construct 3 polynomials  $Q_1, Q_2$  and  $Q_3$ , by taking the equations of lines passing through two of the points  $p_i$ . When the 3 points  $p_1, p_2$  and  $p_3$  are collinear, then the minimal degree is  $d = 2$ . Indeed, there are conics passing through two of these points and avoiding the remaining one.

We discuss now a special type of interpolation node, i.e., a special class of choices for the points  $p_i$ 's. Consider a finite family of lines  $L_j : \ell_j(x, y) = a_jx + b_jy + c_j = 0$  in the plane  $\mathbb{R}^2$ , for  $j = 1, 2, \dots, m$ . If these lines are generic, i.e., no two are parallel and no three are concurrent, then we get precisely

$$N = \binom{m}{2}$$

intersection points, which will play the role of our points  $p_i$ .

**Theorem 2.** *For any  $m$  generic lines in the plane and any given  $N$  values  $c_i$  associated to their intersection points  $p_i$ , there is a unique polynomial  $P(x, y)$  of degree at most  $m - 2$ , such that  $P(p_i) = c_i$  for all  $i = 1, 2, \dots, N$ . More precisely, the evaluation map*

$$\epsilon_d : \mathbb{R}[x, y]_{\leq d} \rightarrow \mathbb{R}^S = \mathbb{R}^N, \quad \epsilon(Q)(p_i) = Q(x_i, y_i),$$

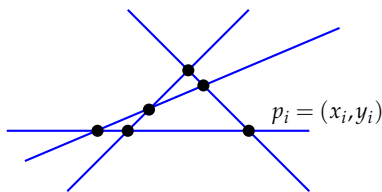


Fig. 2  $m = 4$  generic lines in the plane

is surjective if and only if  $d \geq m - 2$  and it is injective for  $d \leq m - 2$ . A similar claim of surjectivity holds when the lines are replaced by any nodal curve  $C$  of degree  $d$  and the intersection points by the set of nodes of  $C$ .

Note that the degree of  $P$  is much smaller than the number of interpolation points  $p_i$ , namely  $m - 2 < N = m(m - 1)/2$ . The injectivity claim is easy, using Bezout Theorem about the intersection of two plane curves. The surjectivity is subtle, the proof uses Hodge theory, see [7]. The case when  $C$  is a Chebyshev curve is particularly interesting, see [6].

## 2 Projective Duality and Interpolation

From now on we move from the real field  $\mathbb{R}$  to the complex field  $\mathbb{C}$ , and from the affine plane  $\mathbb{C}^2$  to the projective plane  $\mathbb{P}^2$ , with coordinates  $(x : y : z)$ . A point  $p$  in  $\mathbb{P}^2$  is given by 3 homogeneous coordinates

$$p = (a : b : c),$$

where  $a, b, c \in \mathbb{C}$  are not all zero. To such a point we can associate a line  $L_p$  in  $\mathbb{P}^2$ , given by the equation

$$L_p : ax + by + cz = 0.$$

Hence to a set of points  $S = \{p_i : i = 1, 2, \dots, n\}$  in  $\mathbb{P}^2$ , we can associate a line arrangement  $\mathcal{A}_S = \{L_{p_i} : i = 1, 2, \dots, n\}$  in  $\mathbb{P}^2$ . The multiplicity of a point  $p$  in a line arrangement  $\mathcal{A}$  is the number of lines of the arrangement  $\mathcal{A}$  passing through  $p$ . For more on line arrangements we refer to [4].

## 2.1 Splitting type of a line arrangement

Why to pass from points to lines ? Because line arrangements have a lot of geometry. In particular, for any line arrangement  $\mathcal{A}$  in  $\mathbb{P}^2$  one can define a rank two vector bundle  $E = E(\mathcal{A})$  on the projective plane  $\mathbb{P}^2$ , the bundle of logarithmic vector fields along  $\mathcal{A}$ . If  $L$  is a generic line in  $\mathbb{P}^2$ , then the restriction  $E|L$  splits as a direct sum of two line bundles on  $L = \mathbb{P}^1$ , with first Chern classes given by two negative integers, say  $(-a, -b)$ , with  $0 \leq a \leq b$ . The pair  $(a, b)$  is called the splitting type of  $E$  and satisfies  $a + b = |\mathcal{A}| - 1$ . For details, see [1,5].

## 2.2 A new look at the 1-dimensional case: a refinement

The fact that the evaluation map

$$\epsilon_d : \mathbb{R}[x]_{\leq d} \rightarrow \mathbb{R}^S = \mathbb{R}^n, \quad \epsilon(Q)(p_i) = Q(p_i),$$

is surjective for  $d \geq n - 1$  is equivalent to the claim that

$$\dim \ker \epsilon_d = \dim \{Q \in \mathbb{R}[x]_{\leq d} : Q(p_i) = 0 \text{ for any } i\} = d + 1 - n,$$

for  $d \geq n - 1$ . Now fix an integer  $k \geq 1$ , consider a new point  $q \in \mathbb{R}$ , but  $q \notin S$ , and define a new evaluation map

$$\epsilon_{d,q,k} : \mathbb{R}[x]_{\leq d} \rightarrow \mathbb{R}^{n+k} = \mathbb{R}^n \times \mathbb{R}[x]_{\leq k-1},$$

where  $\epsilon(Q)(p_i) = Q(p_i) \in \mathbb{R}$  and  $\epsilon(Q)(q) = T_{k-1}Q(q) \in \mathbb{R}[x]_{\leq k-1}$  is the  $(k - 1)$ -st Taylor expansion of the polynomial  $Q$  at the point  $q$ .

In particular,  $\epsilon(Q)(q) = T_{k-1}Q(q) = 0$  if and only if the first  $(k - 1)$  derivatives of  $Q$  vanish at  $q$ , namely  $Q^{(j)}(q) = 0$  for all  $0 \leq j \leq k - 1$ . It is easy to show that this new evaluation map is surjective for  $d \geq n + k - 1$ , and hence

$$\dim \ker \epsilon_{d,q,k} = d + 1 - n - k,$$

for  $d \geq n + k - 1$ . The practical interest of this refinement is that, for instance, a zero Taylor expansion of high order means very small values for the polynomial  $Q$  in the neighborhood of the given point  $q$ .

### 2.3 A new 2-dimensional interpolation problem

Starting with a given set of points  $S = \{p_i : i = 1, 2, \dots, n\}$  in  $\mathbb{P}^2$ , we fix an integer  $k \geq 1$ , and define  $I(S)_d$  to be the vector space of homogeneous polynomials  $Q \in \mathbb{C}[x, y, z]_d$  such that  $Q(p_i) = 0$  for any  $i = 1, 2, \dots, n$ . Choose then a generic point  $q \in \mathbb{P}^2$  and consider the vector space  $V(d, S, k, q)$  of homogeneous polynomials  $Q \in I(S)_d$  such that  $T_{k-1}Q(q) = 0$ . The expected dimension of this vector space is

$$\dim_e V(d, S, k, q) := \dim I(S)_d - \binom{k+1}{2},$$

when this number is positive. An important special case is when  $d = k$ , which is also the simplest case to consider. In this setting, we introduce the following notion, see [2].

**Definition 1.** We say that the set  $S$  admits an unexpected curve of degree  $k$  if

$$\dim V(k, S, k, q) > \dim_e V(k, S, k, q) \geq 0.$$

The main result in this direction is the following, see [2].

**Theorem 3.** Let  $S$  be a finite set of  $n$  points in  $\mathbb{P}^2$  and let  $(a_S, b_S)$  be the splitting type of the dual line arrangement  $\mathcal{A}_S$ . Then  $S$  admits an unexpected curve of degree  $k$  if and only if the following hold.

- $a_S + 1 \leq k \leq b_S - 1$ ;
- the multiplicity of any intersection point in  $\mathcal{A}_S$  is at most  $a_S + 1$ .

### 2.4 An example: the complete polygonal arrangements

Consider a regular polygon with  $N \geq 3$  edges, and the associated line arrangement  $\mathcal{A}$  consisting of the following  $2N + 1$  lines

- the  $N$  lines determined by the  $N$  edges of the polygon,
- the  $N$  symmetry axes of the polygon, and
- the line at infinity.

This type of line arrangement occurs in the following result, see [3].

**Theorem 4.** For  $N$  even, the complete  $N$ -polygonal arrangement has an unexpected curve of degree  $N$ .

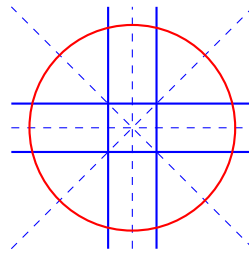


**Fig. 3** Complete 4-polygonal arrangement; the line at infinity is drawn as the red circle.

The proof uses the theory of supersolvable line arrangements to show that  $a = N - 1$  and  $b = N + 1$ . As an example, for  $N = 4$  we get  $a = 3$  and  $b = 5$ . Hence  $\mathcal{A}$  admits an unexpected curve of degree 4 by the result in see [2].

In the case  $N = 4$ , the complete  $N$ -polygonal arrangement is the dual arrangement  $\mathcal{A}_S$ , where the set of points  $S$  consists of the points  $(0 : 0 : 1)$ ,  $(0 : 1 : 0)$ ,  $(1 : 0 : 0)$ ,  $(1 : 1 : 1)$ ,  $(0 : 1 : 1)$ ,  $(1 : 0 : 1)$ ,  $(1 : 1 : 0)$ ,  $(-1 : 1 : 0)$ ,  $(1 : 1 : 2)$ . This situation was considered first by B. Harbourne in [8].

## References

1. Abe T. and Dimca, A.: On the splitting types of bundles of logarithmic vector fields along plane curves, *Internat. J. Math.* 29 (2018), no. 8, 1850055, 20 pp.
2. Cook, D., Harbourne, B., Migliore, J., Nagel, U.: Line arrangements and configurations of points with an unexpected geometric property. *Compositio Mathematica*, 154(2018), 2150-2194.
3. Di Marca, M., Malara, G., Oneto, A.: Unexpected curves arising from special line arrangements, arXiv:1804.02730.
4. Dimca, A.: *Hyperplane Arrangements: An Introduction*, Universitext, Springer-Verlag, 2017, 192+viii pages.
5. Dimca, A. and Sernesi, E.: Syzygies and logarithmic vector fields along plane curves, *Journal de l'École polytechnique-Mathématiques* 1, 247–267(2014)
6. Dimca, A. and Sticlaru, G.: Chebyshev curves, free resolutions and rational curve arrangements, *Math. Proc. Cambridge Phil. Soc.* 153, 385-397 (2012)
7. Dimca, A. and Sticlaru, G.: Koszul complexes and pole order filtrations, *Proc. Edinburgh Math. Soc.* 58, 333–354 (2015)
8. Harbourne, B.: Asymptotics of linear systems, with connections to line arrangements, arXiv:1705.09946.



# Compressions of a polycarbonate honeycomb

André Galligo, Jean Rajchenbach and  
Bernard Rousselet

**Abstract** The in-plane compressive response of a polycarbonate honeycomb with circular close-packed cells is considered first experimentally, then analytically. Under quasi-static uniaxial compression we observed behaviors that strongly depended on the orientation: for one of the two main orientations the compression is homogeneous, while for the other the deformation localizes in a very narrow band of cells. More surprisingly, for extreme but not crushing compression, when the load is released, the deformation is reversed, the localization disappears and the polycarbonate returns to its original shape. In order to explain these strange phenomena, we develop a geometric model of this honeycomb together with an expression of the bending energy. We focus on a basic mechanical element made of an elastica triangle. We also compare our description with previous experimental studies and simulations made with similar material. Finally, to illustrate this type of behavior mathematically, we present a simple model for buckling deformations with two degrees of freedom, which is also reversible.

---

André Galligo  
UCA, LJAD e-mail: [galligo@unice.fr](mailto:galligo@unice.fr)

Jean Rajchenbach  
UCA, Inphyni e-mail: [Jean.Rajchenbach@unice.fr](mailto:Jean.Rajchenbach@unice.fr)

Bernard Rousselet  
UCA, LJAD e-mail: [bernard.rousselet@unice.fr](mailto:bernard.rousselet@unice.fr)

## 1 Introduction

Honeycombs are a widely used material and it is important to understand the mechanism governing their responses to compressions. Here we consider a polycarbonate honeycomb with circular close-packed cells, as shown in the following pictures, which we submitted to an in-plane quasi-static uniaxial compression, with different orientations. Since the common tangents to the circles of the plane initial configuration form an hexagonal mesh, there are two different natural directions of compression, namely, when the vertical compression axis is either parallel or perpendicular to a tangent. In the first case, the circles are positioned in columns, and in the second case they are in a staggered arrangement. We observed that, as expected, in the first case the deformation was homogeneous, compressing all the rows. However, in the second case we observed localization along a few horizontal rows. More surprisingly the second kind of deformations were also reversible, contradicting usual expectations.

To understand these phenomena, we first compared our observations with other published experiments, mainly the excellent work of S. Papka et S. Kyriakides [3], which is accompanied by coherent simulations performed by a detailed computer model. While their aim was to describe the different steps of a complete crushing of a material, the first steps of their described experiments coincide with ours. So our first contribution is the observation of what happens when one releases the load after the localization is achieved, and the surprising fact is that the process is reversible.

Our second contribution is the description of a geometric model for the deformation of the circular close-packed cells and the corresponding hexagonal mesh, controlled by the evolution of the total bending energy of the mechanism. For that purpose, we propose an alternative decomposition of the material in an aggregate of curved triangles instead of the obvious aggregate of circles. We also develop spline approximate models of their geometry. All of this allows us to provide a rational explanation for the considered phenomena.

The last section will be dedicated to the presentation and the mathematical analysis of a simple mechanical model with two degrees of freedom. The target will be to somehow illustrate, with a much simpler model, the observed localization of the deformations that combines a kind of buckling with a rotation; in particular the process is reversible.

We thank the CNRS Fédération Doebelin, for its support during the preparation of this work.

## 1.1 Experiments

We submitted a circular polycarbonate honeycomb to a in-plane quasi-static uniaxial compression, along two compression directions, either parallel or perpendicular to a cell tangent. We observed two completely different behaviors: either a homogeneous deformation or a localization.

Figure 1 shows the first and last step of a compression (before a release of the load); we observe that the middle rows of the cells are strongly bent on the left or on the right and almost crushed. In other words the deformation localizes along the middle rows.

We also notice a quasi invariance by some horizontal translations.

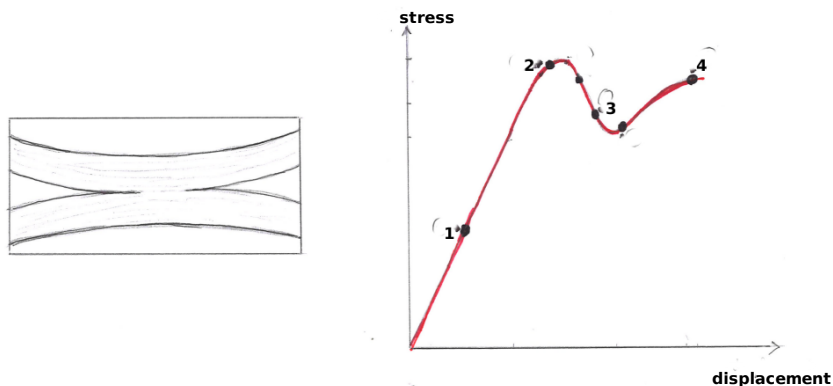


Fig. 1 Compression of a circular honeycomb in a staggered stack

The very surprising fact is that when we stop the compression at this point and leave the material free to relax, it returns to its initial configuration. In an important paper [3], S. Papka and S. Kyriakides studied the crushing of the same kind of polycarbonate honeycombs that we are considering. We refer to the figure 2 of page 243 of the article [3] of S. Papka and S. Kyriakides that describes the sequence they observed through 8 successive images of deformed configurations, corresponding to the response to a long compression. The images labeled (0) to (3) completely conform to our observations, with the same kind of localization phenomena (before we release the load).

S. Papka and S. Kyriakides also mentioned accurate measures of the geometric characteristics of the cells of the honeycomb, pointing out variations of wall thickness and “ovalisation”, illustrated by a schematic that we show in the left panel of Figure 2. These facts were also confirmed in an article [1] by L.L. Hu, T.X. Yu, Z.Y. Gao and X.Q. Huang, who also provided a convincing photo taken with a microscope.

We emphasize that, on the image, we can observe that near the stick points, the ovals coincide at a higher order than a usual tangent point. We based our model on this important observation.



**Fig. 2** Left panel: Sketches of the microscopic geometry near a stick point. Right panel: Non-linear behavior of the response.

S. Papka and S. Kyriakides recorded the compressive response in order to describe the different steps of the crushing, in the right panel of Figure 2 we sketched a graph summarizing the non-linear evolution of the stress against the displacement for our own experiment (before the final crushing). The numbers on this graph correspond to those of Figure 5.

Finally, we also report that S. Papka and S. Kyriakides provided a computer model of the compression process. Their problem was discretized using the software ABAQUS with quadratic beam elements; the simulation of the crushing of a honeycomb was consistent with the observations summarized in the figure cited above and allowed us to precisely describe the process.

## 2 Geometric Modelization

We consider that the basic polycarbonate material of the curved walls is isotropic and hyper elastic, which implies that it admits reversible elementary deformations.

We will assume that the length of each arc of the curve between two stick points does not vary during a deformation and that the deformations keep the sections in the same plane, so the entire study will be conducted in 2D. An invariance by horizontal translations is also assumed.

We consider that the glue between the “circular” packed cells plays a key role that we formalize through the two following geometric hypothesis: During all the compression and release processes we consider that the curvatures at the sticking points are zero. At the beginning of the compression the 3 semi-tangents at the stick points of a curved triangle meet at the same point. This property remains true for small deformations or when the triangle admits a symmetry axis.

Assuming this simplifying property, we can associate to the polycarbonate an abstract hexagonal mesh (made of small tangent segments), which resembles an hexagonal honeycomb and follows the deformation of the polycarbonate.

It makes sense to view the polycarbonate honeycomb not as an aggregate of packed circles, but as an aggregate of curved triangles (represented by Bezier splines) that can be deformed, provided that any two adjacent semi-tangents coincide.

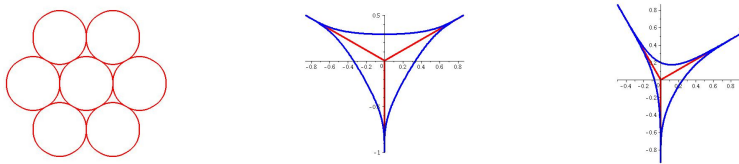


Fig. 3 Model of a curved triangle, undeformed and deformed.

We now present an explanation of the unexpected phenomena observed in our experiments. Let us emphasize, with the illustration of Figure 4, that the initial curved triangles are positioned differently relatively to the load, so that after the first step of the compression the remaining axial symmetries are different.



Fig. 4 Two distinct directions of conserved symmetry.

Let us consider, in both cases (stacks in columns or staggered), the effects of a compression.

## 2.1 *Stack “in columns”*

- The compression respects the horizontal symmetry of each curved triangle, of each oval, and of each hexagon formed by the tangents.
- The stack of hexagons made by the tangents deform (reversibly) to a flattened stack of hexagons.

## 2.2 *“Staggered” stack*

- After a certain load the “horizontal” side of the triangle reaches a maximum allowed length, then either it stops deforming or it buckles and a vertex bends (randomly on the left or on the right), then the triangle rotates in that direction.
- This behavior localizes along a few rows where imperfections provide the weakest resistance to buckling.
- In this process these curved triangles eventually rotate by an angle of  $\frac{\pi}{6}$ , and behave in a way similar to the one described for the curved triangles in a stack “in columns”.

The whole phenomenon is illustrated on the sequence of four images shown in Figure 5, their ordering 1 to 4 correspond to those of Figure 2. To emphasize the described process, we chose three different colors to single out the behavior of each of the curved triangles surrounding an oval in a localizing row. Note that a central symmetry is clearly conserved.

When the load is released, each flattened, curved triangle reacts elastically, in particular those in the upper and lower rows that did not buckle or rotate, and recover their original form. In the localized rows, the vertices that were forced to meet are separated, can relax, the process is then inverted and the curved triangles in the localization row rotate in the opposite direction.

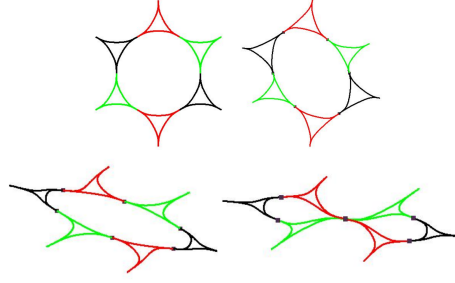


Fig. 5 Deformations and rotations around an oval.

### 3 A simple model for buckling deformations

In this section we present a model with 2 degrees of freedom made of 3 bars linked with 2 hinges; one bar is linked to a fixed hinge, whereas the third one is linked to a hinge that can move horizontally and on which a horizontal load is applied. The system may be described with 3 angles of the bars with respect to the unloaded configuration  $\phi_1, \phi_2, \phi_3$ ; see the figure below. The work of the applied load is  $Pw$ , where the horizontal displacements of the hinges are:

$$u_0 = 0, u_1 = l_1(1 - \cos(\phi_1)), u_2 = l_1(1 - \cos(\phi_1)) + l_2(1 - \cos(\phi_2)), \\ w = l_1(1 - \cos(\phi_1)) + l_2(1 - \cos(\phi_2)) + l_3(1 - \cos(\phi_3)).$$

The horizontal ones are:  $x_0 = 0, x_1 = l_1 \sin(\phi_1), x_2 = l_2 \sin(\phi_2), x_3 = 0$  and we have:  $x_2 - x_1 = l_3 \sin(\phi_3)$ ;  $\phi_1 = \arcsin(\frac{x_1}{l_1})$ ,  $\phi_2 = \arcsin(\frac{x_2}{l_2})$  and  $\phi_3 = \arcsin(\frac{x_2 - x_1}{l_3})$ .

We assume that torsion springs are active on hinges  $A_1$  and  $A_2$ ; we denote the relative angle of rotation of each bar with  $\theta_1, \theta_2$  with respect to its neighbor;  $\theta_1(x_1, x_2) = \phi_1(x_1, x_2) - \phi_3(x_1, x_2)$ ,  $\theta_2(x_1, x_2) = \phi_2(x_1, x_2) + \phi_3(x_1, x_2)$ .

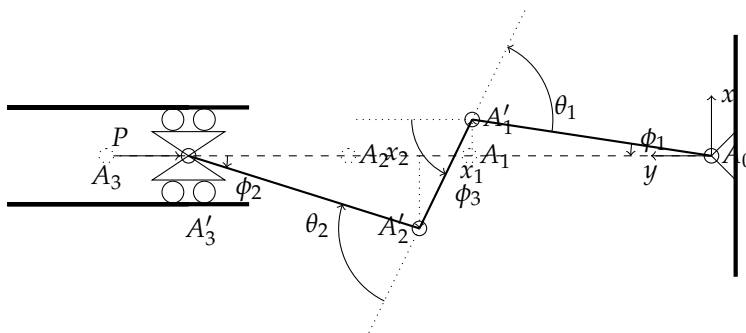
Assuming the torsion springs to be linear elastic, the strain energy is  $\frac{1}{2}(K_1\theta_1^2 + K_2\theta_2^2)$ . Then the total energy involving the work of the applied load is

$$V(x_1, x_2) = \frac{1}{2}[K_1(\theta_1(x_1, x_2))^2 + K_2(\theta_2(x_1, x_2))^2] - Pw(x_1, x_2). \quad (1)$$

With this energy, we get the equilibrium equation:  $\frac{\partial V}{\partial x_1} = 0, \frac{\partial V}{\partial x_2} = 0$ .

To simplify the computations, we assume here that  $l_1 = l_2 = l_3 = 1$  and that  $K_1 = K_2 = 1$ . Then by symmetry, the equilibrium can be reached only if  $x_2 = x_1$  or  $x_2 = -x_1$ .

For  $P < 1$ , then  $x = 0$  is the only stable equilibrium. For  $1 < P < 3$ , then  $x = 0$  is an unstable equilibrium and two stable equilibriums appears for  $x_2 = x_1$  and  $P = \frac{\arcsin(x_1)}{x_1}$ , i.e.,  $|x_1|$  almost equal to  $\sqrt{6(P - 1)}$ . For  $P > 3$ , two stable equilibriums appear for  $x_2 = -x_1$  and  $|x_1|$  almost equal to  $\sqrt{(2(P - 3))/3}$ . This corresponds to the configuration shown in the next figure.



## References

1. Hu, L.L. and Yu, T and Y. Gao, Z and Huang, X.Q.: The inhomogeneous deformation of polycarbonate circular honeycombs under in-plane compression. *International Journal of Mechanical Sciences* (2008), 50
2. López Jiménez, F. and Triantafyllidis, N.: Buckling of rectangular and hexagonal honeycomb under combined axial compression and transverse shear. *International Journal of Solids and Structures*, 50(24), pp.3934–3946, (2013).
3. S.D. Papka, S. Kyriakides: In-plane crushing of a polycarbonate honeycomb. *Int. J. Solids Struct.*, 35 (1998), pp. 239–267
4. Rousselet, B.: *A Finite Strain Rod Model and Its Design Sensitivity. Optimization of Large Structural Systems*, Springer Netherlands (1993).

# Measurement of temperature and thermal gradients using fibre optic long period gratings

Frédéric J Lesage

**Abstract** Ultraviolet-written Long Period Fibre Gratings are demonstrated to be affective tools when measuring thermal gradients of a thermally conductive material. More specifically, variations in the thermal system of a substrate are detected through transmission spectrum responses. While it is well known that uniform temperature leads to pure wavelength shifts of the transmission spectrum minimum, observed changes in transmission loss lead to predictions of thermal gradients. Since Fourier's law of heat conduction implies that heat flux measurements of known conductive materials can be predicted with knowledge of the temperature gradient, the present work demonstrates that optical fibres may be used to develop photonic heat flux sensors. Such an advancement would have a significant impact in industries, such as building materials, in which embedded sensors are used to predict surface thermal boundary layer conditions.

## 1 Introduction

In the physical sciences, our capacity to measure physical phenomena dictates our ability to make scientific observations and to formulate conclusions. For this reason, there is great interest in the scientific community to improve the precision in temperature and heat flux measurements. Indeed,

---

FJ Lesage

Université Côte d'Azur, Center of Modeling, Simulation and Interactions

e-mail: [frederic.lesage@unice.fr](mailto:frederic.lesage@unice.fr)

M Koffi, T Eftimov, WJ Bock, P Mikulic are coauthors from the

Université du Québec en Outaouais, Centre de recherche en photonique

accurate accounts of thermal profiles are key in design, safety, control, and maintenance of a large array of industrial processes [1, 2]. Rather than discuss all processes involving thermal measurements, this paper focuses on the need for improved temperature and heat flux sensors for building materials. More specifically, in the construction industry deteriorating building foundations are due to premature form-work removal (or stripping) when curing structural concrete resulting in a material resistance that is inferior to that which was intended [3]. Strategies to control concrete resistance aim to measure real time curing temperature evolution by inserting a temperature sensor in the form-work before curing begins [4]. The information provided allows for adjustments to be made to the water, limestone and aggregate quantities and to pinpoint the removal time of the concrete encasing [5].

Katipamula and Brambley [6] highlight the need for building material temperature measurements for improved habitat comfort, and for more efficient building energy systems. Other needs for temperature sensors in building materials gravitate towards the detection of faulty design, energy consumption, and structural damage [7,8]. Currently, conventional temperature sensors present certain limitations. As detailed in [1], they can be fragile, be unstable over long-period use, overheat, heat the substrate, and are subject to electromagnetic interference. Furthermore, they are inconvenient over large distances [2]. The present study explores the use of fibre optics as a temperature sensor and as a heat flux sensor. The main thesis of this work is that long-period fibre gratings can be calibrated to measure simultaneously temperature and heat flux. Furthermore, the precision of the measurements relative to conventional methods is promising. This is due to the fact that the measurements rely on the degree of accuracy of wavelength and transmission spectrum measurements.

## 2 Background

Fibre optics are generally made of glass and have the ability to channel light over large distances with minimal loss. They are widely used in telecommunications and have more recently been used as sensors for various applications [9]. The use of fibre optics as sensors was made possible by the development of Fibre Bragg Grating (FBG), characterised by their core's periodic variations in refractive index, and by Long-Period Fibre Grating (LPFG), which feature periodic perturbations in the cladding mode. These fibres have been shown to be sensitive to temperature and deformation [10–12].

In this study, Ultraviolet Long-Period Fibre Gratings (UV-LPFG) are used to detect variations in the transmission spectrum with respect to heat flux

and temperature. As illustrated in the UV-LPG section of Fig. 1, the permutations are written into the fibre cladding and the core (such as in [13]) periodically, thereby changing the propagation modes. The result is a graphical dip in transmission spectrum representing a power loss that is sensitive to the light’s energy levels ( $hc/\lambda$ ).

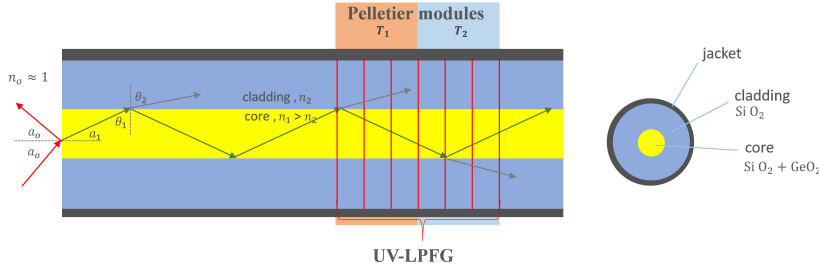


**Fig. 1** Incident light refracting through the core and cladding of an Ultraviolet Long-period Fibre Grating (UV-LPPG) with a thermal gradient maintained using Peltier modules.

Light propagates in the optical fibre according to Snell’s law (also known as Descartes’ law) which states that:

$$n_0 \sin a_0 = n_1 \sin a_1 \tag{1}$$

in which  $n_i$  represents the index of refraction of the medium  $i$ ,  $a_0$  is the incident angle from air and  $a_1$  is the refracted angle into the core of the fibre. Refraction propagates through the fibre in which the core-cladding refraction is also determined by Snell’s law such that  $n_1 \sin \theta_1 = n_2 \sin \theta_2$ . Total internal reflection is achieved when  $\theta_2 = \pi/2$  thereby identifying the critical incident angle  $a_c$  as that for which

$$\sin a_c = \frac{1}{n_0} \sqrt{n_1^2 - n_2^2} \tag{2}$$

In this study, a UV-LPPG is placed in a thermal system environment that measures it’s transmission spectrum with respect to temperature and to heat flux in an effort to provide the ground-work for photonic heat flux and temperature sensors.

### 3 Experimental Set-up

A CLS-561 light source providing 23 dBm ( $\approx 200$  mW) with a spectral power stability of  $\pm 0.2$  dB for wavelengths ranging from 600 nm to 1700 nm provides incident light to an optical fibre. A BK Precision 9201 electric current source is used to power two thermoelectric Peltier modules that are 30 mm  $\times$  30 mm  $\times$  3.8 mm. The modules are used to control the thermal system acting on the fibre. An Agilent 86142B is used to measure the transmission spectrum and an Agilent 34970A is used to measure the temperature data provided by thermocouples.

Experiments are performed in which the transmission spectrum is measured for varying temperatures, temperature gradients and distances between the Peltier modules. The tested LPFG of length 5 cm exhibits a sensitivity of  $d\lambda_c/dT = 0.1286$  nm/K for which  $\lambda_c$  is the centre wavelength corresponding to the wavelength generating the minimum in the transmission spectrum. The sensitivity is measured for a mean temperature varying over 35 °C. The experimental apparatus measures centre wavelength with an accuracy of 0.05 nm, which translates into a mean temperature accuracy of 0.4 °C. As losses and minimum power level measurements can be performed with an accuracy of 0.01 dB, UV-LPFG are used for the simultaneous measurement of temperature gradient and mean temperature by tracking the changes in transmission spectral minimum and centre wavelength.

## 4 Experimental results

### 4.1 Transmission response to temperature gradient

We consider the case in which a target mean temperature is applied to the fibre and the transmission spectrum is measured. The experiments are repeated for varying thermal gradient while maintaining the same target mean temperature. The experimental results illustrated in Fig. 2 demonstrate that an increase in temperature gradient dictates a decrease in the lower peak of the transmission spectrum and that the wavelength generating the peak is independent of temperature gradient. The temperature gradient is identified by the temperature differences ( $\Delta T$ ) generated by the Peltier modules since they are maintained at a fixed centre-to-centre distance of 30 mm.

Similar experimental observations were observed for mean temperatures of 10, 15, 20, 25, 30, 35 and 40 °C in which each set of experiments was conducted over the same range of temperature gradients as that of Fig. 2.

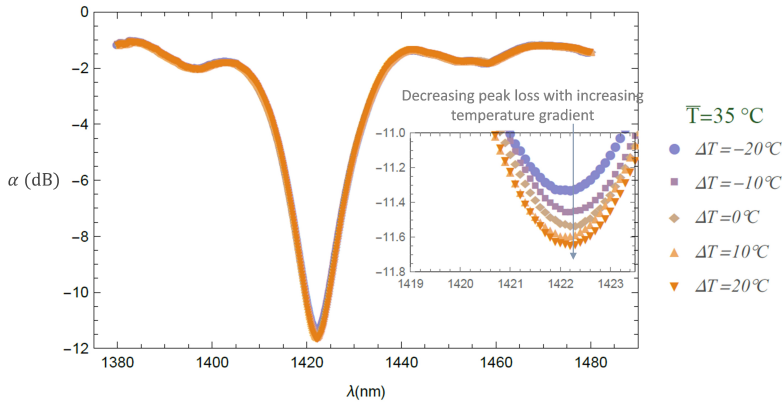


**Fig. 2** Transmission spectrum with respect to varying thermal gradients (denoted  $\Delta T$ ) with fixed distance between Peltier modules and fixed mean temperature  $\bar{T}$ .

Figure 3 presents the measured transmission spectrum minimums (denoted  $\alpha_{min}$ ) with respect to temperature gradient for varying mean temperatures. The results show a linear dependence between transmission spectrum minimums and temperature differences. Furthermore, a curve fitting to the measured data is used to provide a predictive tool. More specifically, the following linear equation predicts the thermal gradient from transmission spectrum results for the tested optical fibre.

$$\Delta T(\alpha_{min}) = -137.1\alpha_{min} - 1577.9 \tag{3}$$

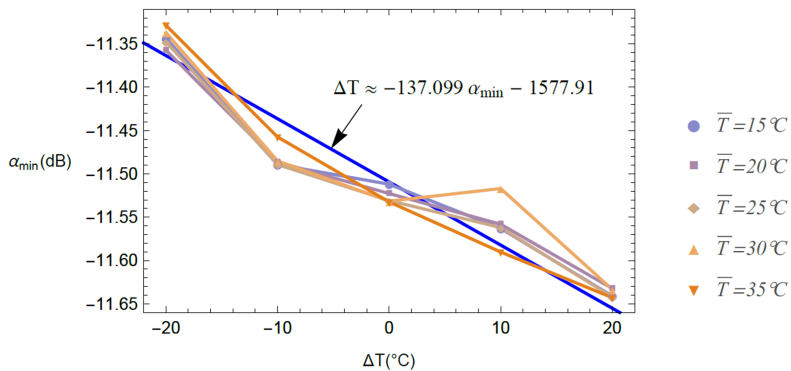


**Fig. 3** Minimum transmission spectrum with respect to varying thermal gradient.

## 4.2 Transmission response to mean temperature

We now consider the case in which a target temperature difference is maintained for a series of experiments with varying mean temperatures. The results illustrated in Fig. 4 show that as the mean temperature increases, the lower peak of the transmission spectrum remains constant. However, the results also show the centre wavelength increasing mean temperature.

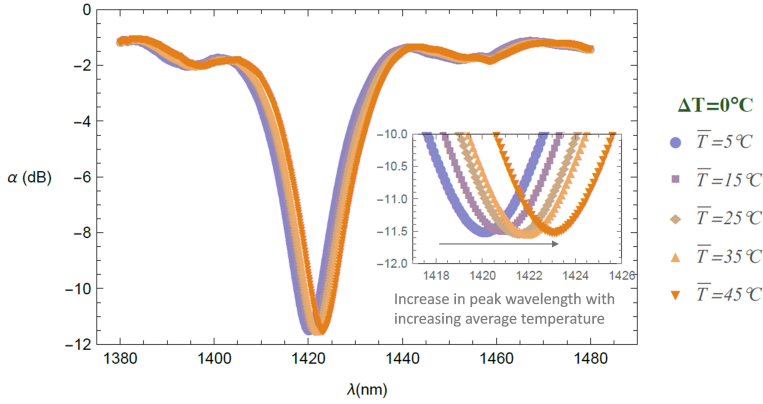


**Fig. 4** Transmission spectrum with respect to varying mean temperature ( $\bar{T}$ ) with fixed thermal gradient.

Similar experimental observations were observed for  $\Delta T$  values of  $-20$ ,  $-10$ ,  $0$ ,  $10$  and  $20$   $^{\circ}\text{C}$  in which each set of experiments was conducted over the same range of mean temperatures as that of Fig. 4.

The results illustrated in Fig. 5 show a linear relation between the centre wavelength and the mean temperature. The following linear curve fit can be used to predict the substrate's mean temperature from the transmission results for the tested optical fibre.

$$\bar{T}(\lambda_o) = 13.1\lambda_o - 18549.0 \quad (4)$$

Equations (3) and (4) imply that the transmission spectrum measurements, and more specifically, the coordinates of the peak dip in transmission, can be used to determine the mean temperature and the thermal gradient of a material over a length spanning  $30$   $\text{mm}$ . The accuracy of the  $\Delta T$  and  $\bar{T}$  measurements is evaluated as being within  $0.34^{\circ}\text{C}$  due to the peak transmission measurements being within  $0.0001$   $\text{dB}$ .

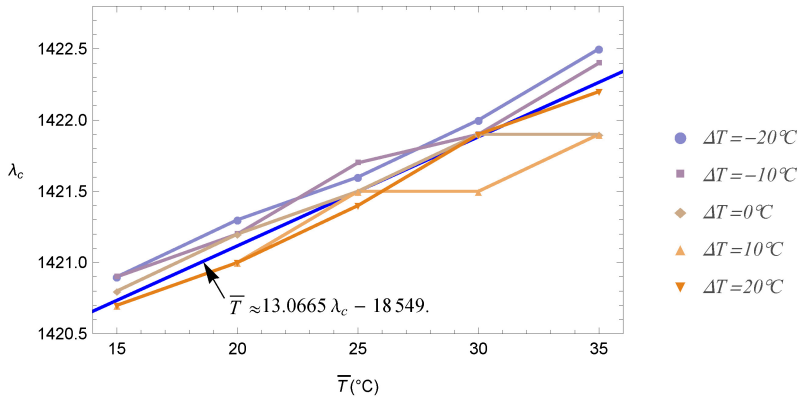


Fig. 5 Centre wavelength with respect to mean temperature

## 5 Conclusion

This work shows that optical fibres can be used to simultaneously measure the thermal behaviour of a substrate. It is demonstrated that the mean temperature is a linear function of the transmission spectrum's centre wavelength and that the temperature gradient is a linear function of the transmission spectrum's minimum value. Therefore, by applying Fourier's law of heat conduction, a single photonic sensor can be calibrated and used to measure the temperature and heat flux of a substrate with known proprieties. This technology has potential applications in many industries, such as combustion engines, integrated circuits and building materials since current heat flux sensors require two temperature readings resulting in a high uncertainty. Furthermore, optical fibres can be easily embedded into materials thereby providing surface boundary conditions by using the inverse heat conduction method.

## Acknowledgements

This work has been supported by the French government, through the UCA-JEDI Investments in the Future project managed by the National Research Agency (ANR) with the reference number ANR-15-IDEX-01, and by the Natural Sciences and Engineering Research Council of Canada under Grant RGPIN-2015-05242.

## References

1. Ping Lu, Liqiu Men, Kevin Sooley, and Qiying Chen. Tapered fiber mach–zehnder interferometer for simultaneous measurement of refractive index and temperature. *Applied Physics Letters*, 94(13):131110, 2009.
2. Mohtashim Mansoor, Ibraheem Haneef, Suhail Akhtar, Andrea De Luca, and Florin Udrea. Silicon diode temperature sensors—a review of applications. *Sensors and Actuators A: Physical*, 232:63–74, 2015.
3. SK Ghosh. Construction loading in high-rise buildings: Properties of concrete at early ages. *Edward G. Nawy (2nd ed.), Concrete construction engineering handbook*, page 307, 2008.
4. Jiukun Dai, Charles R Wood, and Michael King. The use of the concrete maturity method in the construction of industrial facilities: A case study. 2004.
5. AJ Robinson, FJ Lesage, A Reilly, G McGranaghan, G Byrne, R O’Hegarty, and O Kinane. A new transient method for determining thermal properties of wall sections. *Energy and Buildings*, 142:139–146, 2017.
6. Srinivas Katipamula and Michael R Brambley. Methods for fault detection, diagnostics, and prognostics for building systems—a review, part i. *Hvac&R Research*, 11(1):3–25, 2005.
7. F Ya. Situation and design for energy-efficiency building envelope in south of china. *Construction Conserves Energy*, 46:57–59, 2006.
8. Edgar H Callaway Jr. *Wireless sensor networks: architectures and protocols*. CRC press, 2003.
9. N Ayyanar, R Vasantha Jayakantha Raja, D Vigneswaran, B Lakshmi, M Sumathi, and K Porsezian. Highly efficient compact temperature sensor using liquid infiltrated asymmetric dual elliptical core photonic crystal fiber. *Optical Materials*, 64:574–582, 2017.
10. Bai-Ou Guan, Hwa-Yaw Tam, Xiao-Ming Tao, and Xiao-Yi Dong. Simultaneous strain and temperature measurement using a superstructure fiber bragg grating. *IEEE Photonics Technology Letters*, 12(6):675–677, 2000.
11. Ebrahim Oromiehie, B Gangadhara Prusty, Paul Compston, and Ginu Rajan. In-situ simultaneous measurement of strain and temperature in automated fiber placement (afp) using optical fiber bragg grating (fbg) sensors. *Advanced Manufacturing: Polymer & Composites Science*, 3(2):52–61, 2017.
12. Chao Li, Tigang Ning, Jing Li, Li Pei, Chan Zhang, Chuanbiao Zhang, Heng Lin, and Xiaodong Wen. Simultaneous measurement of refractive index, strain, and temperature based on a four-core fiber combined with a fiber bragg grating. *Optics & Laser Technology*, 90:179–184, 2017.
13. Ashish M Vengsarkar, Paul J Lemaire, Justin B Judkins, Vikram Bhatia, Turan Erdogan, and John E Sipe. Long-period fiber gratings as band-rejection filters. *Journal of lightwave technology*, 14(1):58–65, 1996.

# Nudging-based observers for geophysical data assimilation and joint state-parameters estimation

Samira Amraoui, Didier Auroux, Jacques Blum,  
Blaise Faugeras

**Abstract** Oceans and the atmosphere are governed by the general equations of fluid dynamics. Data assimilation consists of estimating the state of a system by combining, via numerical methods, two different sources of information: models and observations.

The Back and Forth Nudging (BFN) algorithm is a prototype of a new class of data assimilation methods. The nudging technique consists in adding a feedback term in the model equations, measuring the difference between the observations and the corresponding space states. The BFN algorithm is an iterative sequence of forward and backward resolutions, all of them being performed with an additional nudging feedback term in the model equations.

These nudging-based algorithms can be extended with the aim of correcting non-observed variables. This particularly concerns model parameter identification, with the potential of improving the quality and the confidence in the model state for future data assimilation processes.

## 1 Introduction

It is well established that the quality of weather and ocean circulation forecasts is highly dependent on the quality of the initial conditions. Geophysi-

---

Université Côte d'Azur, CNRS, LJAD, France, e-mail: [amraoui](mailto:amraoui); [auroux](mailto:auroux); [jblum](mailto:jblum); [faugeras@unice.fr](mailto:faugeras@unice.fr)

cal fluids (air, atmospheric, oceanic, surface or underground water) are governed by the general equations of fluid dynamics. Geophysical processes are hence nonlinear because of their fluid component. Such nonlinearities impose a huge sensitivity to the initial conditions, and then an ultimate limit to deterministic prediction (estimated to be about two weeks for weather prediction, for example). This limit is still far from being reached, and substantial gains can still be obtained in the quality of forecasts.

Data assimilation (DA) is precisely the domain at the interface between observations and models that makes it possible to identify the global structure of a system from a set of discrete space-time data. DA covers all the mathematical and numerical techniques in which the observed information is accumulated into the model state by taking advantage of consistency constraints with laws of time evolution and physical properties, and which allow us to blend, as optimally as possible, all the sources of information coming from theory, models and other types of data.

There are two main categories of DA techniques [1], variational methods based on the optimal control theory [2] and statistical methods based on the theory of optimal statistical estimation (for example, see [3–5] for an overview of inverse methods, both for oceanography and meteorology).

Here, we study the Back and Forth Nudging (BFN) algorithm, which is the prototype of a new class of data assimilation methods, although the standard nudging algorithm has been known for a couple of decades. The nudging technique consists in adding a feedback term in the model equations, measuring the difference between the observations and the corresponding space states. The idea is to apply the standard nudging algorithm to the backward (in time) nonlinear model in order to stabilize it. The BFN algorithm is an iterative sequence of forward and backward resolutions, all of them being performed with an additional nudging feedback term in the model equations. We also present the Diffusive Back and Forth Nudging (DBFN) algorithm, which is a natural extension of the BFN to some particular diffusive models, and the P-BFN for parameter estimation (possibly jointly with state estimation).

## 2 Back and Forth Nudging

### 2.1 *The nudging algorithm*

The standard nudging algorithm consists in adding, to the state equations, a feedback term, which is proportional to the difference between the observation and its equivalent quantity computed by the resolution of the state

equations. The model appears then as a weak constraint, and the nudging term forces the state variables to fit as well as possible to the observations.

Let us consider a very generic model

$$\begin{cases} \frac{dX}{dt} = F(X, U), & 0 < t < T, \\ X(0) = V. \end{cases} \quad (1)$$

We assume that we have an observation  $X_{obs}(t)$  of the state variable  $X(t)$ . The nudging algorithm simply gives

$$\begin{cases} \frac{dX}{dt} = F(X, U) + K(X_{obs} - HX), & 0 < t < T, \\ X(0) = V, \end{cases} \quad (2)$$

where  $H$  is the observation operator, allowing us to compare the observation  $X_{obs}$  with the corresponding quantity of the model solution  $X$ , and  $K$  is the nudging matrix. It is quite easy to understand that if  $K$  is large enough, then the state vector transposed into the observation space (through the observation operator)  $HX(t)$  will tend towards the observation vector  $X_{obs}(t)$ . In the linear case (where  $F$  and  $H$  are linear operators), the forward nudging method is nothing else than the Luenberger observer [6], a deterministic and time continuous alternative method to statistical Kalman filtering method first introduced in 1966. The operator  $K$  can be chosen so that the error goes to zero when time goes to infinity, hence its name of asymptotic observer.

This algorithm was first used in meteorology [7], and has since been used with success in oceanography [8] and applied to a mesoscale model of the atmosphere [9]. Many results have also been carried out on the optimal determination of the nudging coefficients  $K$  [10–12].

The backward nudging algorithm consists in solving the state equations of the model backwards in time, starting from the observation of the state of the system at the final instant. A nudging term, with the opposite sign compared to the standard nudging algorithm, is added to the state equations, and the final obtained state is in fact the initial state of the system [13, 14].

## 2.2 The BFN algorithm

The Back and Forth Nudging (BFN) algorithm consists in solving first the forward (standard) nudging equation, and then the backward nudging equation. After resolution of this backward equation, one obtains an estimate of

the initial state of the system. We repeat these forward and backward resolutions with the feedback terms until convergence of the algorithm [14].

The BFN algorithm is then the following:

$$\begin{cases} \frac{dX_k}{dt} = F(X_k, U) + K(X_{obs} - HX_k), & 0 < t < T, \\ X_k(0) = \tilde{X}_{k-1}(0), \end{cases} \quad (3)$$

$$\begin{cases} \frac{d\tilde{X}_k}{dt} = F(\tilde{X}_k, U) - K(X_{obs} - H\tilde{X}_k), & T < t < 0, \\ \tilde{X}_k(T) = X_k(T), \end{cases}$$

with  $X_0(0) = V$  as initial condition. Starting from  $V$ , a resolution of the direct model gives  $X_0(T)$  and hence  $\tilde{X}_0(T)$ . Then a resolution of the backward model provides  $\tilde{X}_0(0)$ , which is equal to  $X_1(0)$ , and so on.

This algorithm can be compared to the variational algorithm (4D-VAR, based on optimal control theory), which also consists in a sequence of forward and backward resolutions. In the BFN algorithm, even for nonlinear problems, it is useless to linearize the system and the computation of the backward system is as easy as the direct system, unlike an adjoint equation, the determination of which can be a playful task. In the case of ill-posed backward resolution, the extra feedback term in backward equation has the additional property to stabilize the numerical resolution.

The BFN algorithm has been tested successfully for the system of Lorenz equations, Burgers equation and a quasi-geostrophic ocean model in [15], for a shallow-water model in [16] and compared with a variational approach for all these models. It has been used to assimilate the wind data in a mesoscale model [17] and for the reconstruction of quantum states in [18].

### 2.3 DBFN: Diffusive Back and Forth Nudging algorithm

In the framework of oceanographic and meteorological problems, there is usually no diffusion in the model equations. However, the numerical equations that are solved contain some diffusion terms in order to both stabilize the numerical integration (or the numerical scheme is set to be slightly diffusive) and model some subscale turbulence processes. We can then separate the diffusion term from the rest of the model terms, and assume that the partial differential equations read:

$$\frac{dX}{dt} = F(X) + \nu \Delta X, \quad 0 < t < T, \quad (4)$$

where  $F$  has no diffusive terms,  $\nu$  is the diffusion coefficient, and we assume that the diffusion is a standard second-order Laplacian (note that it could be a fourth or sixth order derivative in some oceanographic models, but for clarity, we assume here that it is a Laplacian operator).

We introduce the D-BFN algorithm in this framework, for  $k \geq 1$ :

$$\begin{cases} \frac{dX_k}{dt} = F(X_k) + \nu\Delta X_k + K(X_{obs} - H(X_k)), & 0 < t < T, \\ X_k(0) = \tilde{X}_{k-1}(0), \end{cases} \quad (5)$$

$$\begin{cases} \frac{d\tilde{X}_k}{dt} = F(\tilde{X}_k) - \nu\Delta\tilde{X}_k - K'(X_{obs} - H(\tilde{X}_k)), & T > t > 0, \\ \tilde{X}_k(T) = X_k(T). \end{cases}$$

It is straightforward to see that the backward equation can be rewritten, using  $t' = T - t$ :

$$\begin{cases} \frac{d\tilde{X}_k}{dt'} = -F(\tilde{X}_k) + \nu\Delta\tilde{X}_k + K'(X_{obs} - H(\tilde{X}_k)), & 0 < t' < T, \\ \tilde{X}_k(t' = 0) = X_k(T). \end{cases} \quad (6)$$

where  $\tilde{X}_k$  is evaluated at time  $t'$ , the backward equation is well-posed, with an initial condition and the same diffusion operator as in the forward equation. The diffusion term both takes into account the subscale processes and stabilizes the numerical backward integrations, and the feedback term still controls the trajectory with the observations.

The main interest of this new algorithm is that for many geophysical problems, the non-diffusive part of the model is reversible, and the backward model is then stable. Moreover, the forward and backward equations are now consistent in the sense that they will be both diffusive in the same way (as if the numerical schemes were the same in forward and backward integrations), and only the non-diffusive part of the physical model is solved backwards. Note that in this case, it is reasonable to set  $K' = K$ .

The DBFN algorithm has been tested successfully for a linear transport equation in [19] and for the non-linear Burgers equation in [20].

## 2.4 Theoretical considerations

Data Assimilation is the ensemble of techniques combining the mathematical information provided by the equations of the model and the physical

information given by the observations in order to retrieve the state of a flow. In order to show that both BFN and DBFN algorithms achieve this double objective, let us give a formal explanation of the way these algorithms proceed.

If  $K' = K$  and the forward and backward limit trajectory are equal, i.e  $\tilde{X}_\infty = X_\infty$ , then taking the sum of the two equations in (3) shows that the limit trajectory  $X_\infty$  satisfies the model equation (1) (including possible model viscosity). Moreover, the difference between the two equations in (3) shows that the limit trajectory is the solution of the following equation:

$$K(X_{obs} - H(X_\infty)) = 0. \quad (7)$$

Equation (7) shows that the limit trajectory perfectly fits the observations (through the observation operator, and the gain matrix). In a similar way, for the DBFN algorithm, taking the sum of the two equations in (5) shows that the limit trajectory  $X_\infty$  satisfies the model equations without diffusion:

$$\frac{dX_\infty}{dt} = F(X_\infty) \quad (8)$$

while taking the difference between the two same equations shows that  $X_\infty$  satisfies the Poisson equation:

$$\Delta X_\infty = -\frac{K}{\nu}(X_{obs} - H(X_\infty)) \quad (9)$$

which represents a smoothing process on the observations for which the degree of smoothness is given by the ratio  $\frac{\nu}{K}$  [19]. Equation (9) corresponds, in the case where  $H$  is a matrix and  $K = kH^T R^{-1}$ , to the Euler equation of the minimization of the following cost function

$$J(X) = k\langle R^{-1}(X_{obs} - HX), (X_{obs} - HX) \rangle + \nu \int_{\Omega} \|\nabla X\|^2 \quad (10)$$

where the first term represents the quadratic difference to the observations and the second one is a first order Tikhonov regularisation term over the domain of resolution  $\Omega$ . The vector  $X_\infty$ , solution of (9), is the point where the minimum of this cost function is reached. This is a nice increment to the BFN algorithm, in which the limit trajectory fits the observations, while in the DBFN algorithm, the limit trajectory is the result of a smoothing process on the observations (which are often very noisy).

## 2.5 P-BFN for parameter estimation

In many physical or biological dynamical systems the state equations contain parameters that are not well known and need to be estimated. The usual approach to achieve this identification is to include the unknown parameters together with the initial conditions into the set of control variables and to minimize a cost function measuring the discrepancy between the model outputs and the observations. The drawback of this approach is that it necessitates the computation of derivatives with respect to the parameters.

On the other hand, the relative simplicity of the BFN framework is attractive to perform parameter identification. The state equations can be augmented with equations expressing the stationarity of the parameters, the initial conditions being the parameters values:

$$\begin{cases} \frac{dX}{dt} = F(X, P), & 0 < t < T, & X(0) = V, \\ \frac{dP}{dt} = 0, & 0 < t < T, & P(0) = U. \end{cases} \quad (11)$$

A Lyapunov functional is then formulated and enables one to obtain the expression of the nudging term to be added to these parameter equations [21]. Note that using observations on the state only, it is possible to add feedback terms (to the observations) on both parameter and state equations.

Finally BFN-like iterations provide, after convergence, an estimate of the the initial conditions for the state equations and the parameter's supplementary equations thus giving an estimate of the unknown parameters.

## 3 Numerical results

Let us now consider the simple example of a 1D transport equation and assume that the parameter  $a(x)$  of this transport equation is unknown. We want to estimate both the model state  $u$  and parameter  $a$ . We add an ad hoc equation for the time-independent parameter:

$$\begin{cases} \partial_t u(t, x) + a(x) \partial_x u(t, x) = 0, & u(0, x) = u_0(x), \\ \partial_t a(t, x) = 0, & a(0, x) = a(x). \end{cases}$$

Then we apply the BFN algorithm to this coupled system, and we add feedback terms to both equations, using only observations on the state  $u$ :

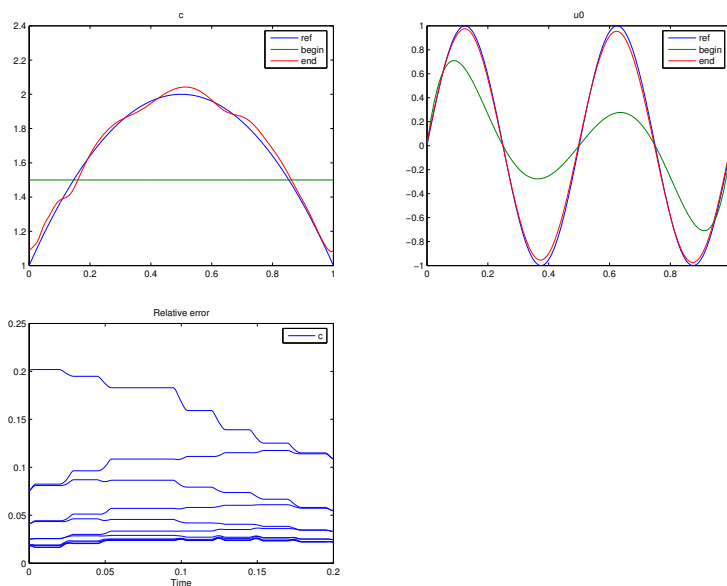


**Fig. 1** Comparisons between the true augmented state (state and parameter) and its estimation by P-BFN algorithm: reconstruction of parameter (left) and state (right). Relative error of parameter reconstruction (bottom) with regards to P-BFN iterations in a time window of  $[0, T]$  equal to  $[0, 0.2]$ .

$$\begin{cases} \partial_t \hat{u}(t, x) + \hat{a}(t, x) \partial_x \hat{u}(t, x) = K_u (u_{obs}(t, x) - \hat{u}(t, x)), \\ \partial_t \hat{a}(t, x) = K_a \mathcal{F}(u_{obs}(t, x) - \hat{u}(t, x)), \end{cases}$$

where  $\mathcal{F}$  is a feedback function involving spatial differential operators, such that there exists a Lyapunov function that decreases in time.

Then, we can prove that both  $u$  and  $a$  can be reconstructed, as it can be seen in Figure 1.

## 4 Conclusion

For state estimation, the BFN algorithm is a valuable technique for many reasons: its ease of implementation (simple combination of model and observation functions), its robustness and fast convergence, without requiring any linearization or optimization processes. When it comes to dealing with large-scale problems, as is already the case in meteorology and oceanography, the use of high computational cost methods is barely possible and BFN

can be a suitable solution. In terms of efficiency, the estimation provided by the BFN is comparable to other data assimilation methods in all tests conducted.

Its range of application can be extended to parameter estimation. By taking advantage of model parameter information contained in the state solution, the P-BFN identifies the model parameter exclusively from state observations. The numerical tests on the identification of the velocity parameter in a transport equation confirm that both state and parameter can be estimated without increasing the computational cost.

**Acknowledgment:** This work has been supported by the French government, through the UCAJEDI Investments in the Future project managed by the National Research Agency (ANR) with the reference number ANR-15-IDEX-01.

## References

1. O. Talagrand. Assimilation of observations, an introduction. *Journal of the Met. Soc. of Japan*, 75(1B):191–209, 1997.
2. J. L. Lions. *Contrôle optimal de systèmes gouvernés par des équations aux dérivées partielles*. Dunod, 1968.
3. A. F. Bennett. *Inverse Modeling of the Ocean and Atmosphere*. Cambridge University Press, Cambridge, 2002.
4. E. Kalnay. *Atmospheric modeling, data assimilation and predictability*. Cambridge Univ. Press, 2003.
5. J. Blum, F.-X. Le Dimet, and I. M. Navon. Data assimilation for geophysical fluids. In *Computational methods for the atmosphere and the oceans, Handbook of Numerical Analysis, Vol. XIV*, pages 385–441. Elsevier, 2009.
6. D. Luenberger. Observers for multivariable systems. *IEEE Trans. Autom. Contr.*, 11:190–197, 1966.
7. J. Hoke and R. A. Anthes. The initialization of numerical models by a dynamic initialization technique. *Month. Weaver Rev.*, 104:1551–1556, 1976.
8. J. Verron and W. R. Holland. Impact de données d’altimétrie satellitaire sur les simulations numériques des circulations générales océaniques aux latitudes moyennes. *Ann. Geophys.*, 7(1):31–46, 1989.
9. D. R. Stauffer and N. L. Seaman. Use of four dimensional data assimilation in a limited area mesoscale model - part 1: Experiments with synoptic-scale data. *Month. Weather Rev.*, 118:1250–1277, 1990.
10. X. Zou, I. M. Navon, and F.-X. Le Dimet. An optimal nudging data assimilation scheme using parameter estimation. *Quart. J. Roy. Meteorol. Soc.*, 118:1163–1186, 1992.
11. D. R. Stauffer and J. W. Bao. Optimal determination of nudging coefficients using the adjoint equations. *Tellus A*, 45:358–369, 1993.
12. P. A. Vidard, F.-X. Le Dimet, and A. Piacentini. Determination of optimal nudging coefficients. *Tellus A*, 55:1–15, 2003.
13. D. Auroux. *Étude de différentes méthodes d’assimilation de données pour l’environnement*. PhD thesis, University of Nice - Sophia Antipolis, France, 2003.

14. D. Auroux and J. Blum. Back and forth nudging algorithm for data assimilation problems. *C. R. Acad. Sci. Paris, Ser. I*, 340:873–878, 2005.
15. D. Auroux and J. Blum. A nudging-based data assimilation method for oceanographic problems: the Back and Forth Nudging (BFN) algorithm. *Nonlin. Proc. Geophys.*, 15:305–319, 2008.
16. D. Auroux. The Back and Forth Nudging algorithm applied to a shallow water model, comparison and hybridization with the 4D-VAR. *Int. J. Numer. Methods Fluids*, 61(8):911–929, 2009.
17. A. Boilley and J.-F. Mahfouf. Assimilation of low-level wind in a high resolution mesoscale model using the back and forth nudging algorithm. *Tellus A*, 64:18697, 2012.
18. Z. Leghtas, M. Mirrahimi, and P. Rouchon. Observer-based quantum state estimation by continuous weak measurement. In *American Control Conference (ACC)*, pages 4334–4339, 2011.
19. D. Auroux, J. Blum, and M. Nodet. Diffusive Back and Forth Nudging algorithm for data assimilation. *C. R. Acad. Sci. Paris, Ser. I*, 349(15-16):849–854, 2011.
20. D. Auroux, P. Bansart, and J. Blum. An evolution of the Back and Forth Nudging for geophysical data assimilation: application to burgers equation and comparisons. *Inv. Prob. Sci. Eng.*, 21(3):399–419, 2013.
21. A. Donovan, M. Mirrahimi, and P. Rouchon. Back and Forth Nudging for quantum state reconstruction. In *4th Int. Symp. Communications Control Signal Proc.*, pages 1–5, 2010.

# The retina: a fascinating object of study for a physicist

Bruno Cessac

**Abstract** I briefly present joint research where ideas and methods from theoretical physics can be applied to better understand the behaviour of the retina in normal, developmental and pharmacologically controlled conditions.

## 1 Introduction

Our visual system has astonishing capacities, from the rapid extraction of the main features of a visual scene, to higher level tasks like reading or face recognition. Our vision starts from the retina. This tiny membrane, only a few hundred microns thick, covering 75% of the internal ocular globe performs fundamental yet complex tasks. Although its primary function is to convert the photons from the outer world into sequences of action potentials (spike trains), encoding the visual scene, and conveying them to the visual cortex where they will be "decoded", the retina is not a mere camera. In recent years, researchers have indeed discovered that the retina "is smarter than scientists believed" [1].

In this paper, I would like to share with the reader the fascination of the retina for a physicist, working for years in the field of dynamical systems theory and statistical physics applied to "complex systems", especially neuronal models. Working with biologists and retinal specialists, I have discovered a beautiful object of studies both from the applied and theoretical

---

Bruno Cessac

Université Côte d'Azur, Biovision research project, Inria, 2004 route des Lucioles, 06902 Sophia-Antipolis e-mail: [bruno.cessac@inria.fr](mailto:bruno.cessac@inria.fr)

physics point of view. The retinal machinery (neurons, synapses, ion transport, light conversion from photoreceptors, etc.) is governed by physics. Yet the extrapolation of physical methods from theoretical physics (mean-field methods, transport equations, Gibbs distributions, etc.) raises several interesting questions that I have been confronted with during my research, and which I want to briefly present in this paper.

## 2 The retina structure

Throughout this paper, I will use "computer-oriented" language to deal with the retina: information, circuits, code, decode, computation, etc. This is a contemporary view, largely influenced by our computer-based society. Although this analogy is useful - it eases explanations and provides fruitful paradigms - it has its limitations, which are stressed throughout this paper.

The retina, much like the rest of our body, especially the brain, has an evident problem: it can't tolerate large variations in temperature. Especially, the Joule effect has to be strongly limited. As a consequence, neurons, which are cells producing electric currents, do not use electrons, instead they use ion transfer (sodium, potassium, calcium, chloride, etc.). The currents produced this way are small (of order 1 – 100 pA), as well as voltage variations ( $\sim 100$  mV), thus with an electric power of order pW. Even if there are many neurons of different types in the retina (of order  $10^8$ , including photoreceptors), the total heat production is quite small compared to a computer that would perform the same tasks. However, ions are quite slow, and the corollary is that the retina has to use massive parallel computations to perform complex tasks in a short time. This computation is achieved via neurons, but also by synapses: the synaptic organization of the retina plays a central role in its abilities (e.g., <http://webvision.med.utah.edu/book/part-i-foundations/simple-anatomy-of-the-retina/>).

The retina converts photons into variations of electric potential (phototransduction) via **photoreceptor** cells: rods (about 130 million) ensure eyesight in poor illumination; cones (about 7 million) ensure central vision and colour perception. Phototransduction is a very efficient mechanism as a single photon can produce a visual effect. This is due to a complex cascade of molecular mechanisms with a huge multiplicative effect. At the other side of the retina one finds **retinal ganglion cells** (RGCs), the final stage of retina encoding, as these are the cells that emit action potentials (spikes) via their axons (which constitute the optic nerve) to the visual cortex via the thalamus. There are about 1.2 to 1.5 million RGCs in the human retina. On average, each RGC receives inputs from about 100 rods and cones. These numbers

vary greatly among individuals and as a function of retinal location. In between, one finds 3 cells types: horizontal, bipolar and amacrine cells. Unlike most neurons, these cells communicate via graded potentials, rather than action potentials. **Horizontal cells** are laterally interconnecting neurons, helping integrate and regulate the input from multiple photoreceptors. **Bipolar cells** transmit the signals from the photoreceptors or the horizontal cells, and pass them on to the ganglion cells directly or indirectly (via **amacrine cells**).

The retina has therefore both a feed-forward structure (from photoreceptors to ganglion cells) and a lateral structure (due to horizontal and amacrine cells). This generates different types of neural circuits, which enable the RGCs to efficiently process local visual information such as dim light, small responses to single photon absorption, segregating moving objects, filtering the movement of body, head, or eye, motion extrapolation, detection of approaching motion, surprise at the missing element in the sequence. Many of these computations match the evident challenge of animals: to detect moving objects and locate them correctly; to struggle with a constantly moving image sensor; and to predict the future and adapt to changing conditions [1]. Thus, the thalamus and visual cortex receive not a computer-like pixel representation of the image, but a set of features processed via nonlinear mechanisms that researchers try to identify [1].

The optic nerve is therefore like an optical fiber with several millions of channels - the axon of each RGC - conveying a local spatio-temporal information encoded by sequences of spikes, decoded by the brain. However, in contrast to computers, the code has variability and, nevertheless, robustness. First, several presentations of the same visual stimulus do not trigger the same sequence of spikes although some statistical regularity is observed (typically, a given RGC type fires more intensively when a specific stimulus is presented). Second, there is not a unique coding strategy. RGCs convey part of the information independently from each other through their firing rates, or timing of spikes. But they share information because the spatial regions that they scan have overlaps (a photoreceptor contributes the activity of several RGCs) inducing stimuli-induced correlations in their response. In addition, the lateral connections from horizontal and amacrine cells induce indirect interactions between RGCs. Therefore, RGCs presumably also encode information at a population level. This "population coding" presents several advantages: redundancy, reduction of uncertainty, simultaneous coding of different stimulus attributes, fast response, etc. It is however a contemporary challenge to understand it.

### 3 Population coding and statistical physics

Current acquisition technologies (Multi-Electrodes Array, MEA) allow us to simultaneously record several thousands of RGCs in response to a visual scene, providing a contemporary challenge: to try and decipher the visual scene from the RGC spikes and thereby infer coding strategies of the visual system. Part of this information can be recovered by assuming that cells encode information independently. This allows one to design "decoders" based on firing rate, spike latency, rank order, etc. Yet, the decoders built this way have many fitting parameters and their efficiency may vary with the visual stimulus. In addition, it has been shown [2] that a part of the information is carried by the (weak) correlations between RGCs suggesting that population coding takes place.

For a modeller, it seems clear that a population of connected neurons submitted to an external stimulus will produce a correlated response at the population level. We have made a mathematical analysis of this aspect in [3,4], using Integrate and Fire models. We have shown that the population statistics are described by a variable length Markov chain where transition probabilities can be explicitly written: they depend on neuron connectivity, on the stimulus and on spike history in a similar fashion as the so-called Generalized Linear Models [5].

Such Markov chains are closely related to what physicists call "Gibbs distributions", initially introduced by Boltzmann and Gibbs to establish a link between microscopic dynamics of particles and thermodynamics. Gibbs distributions are probabilities of exponential form where the term in the exponential is, in physics, proportional to the energy; the form of the energy is constrained by the forces involved in the problem and defines a statistical model or an "ensemble". More generally, in the correspondence with Markov chain, the term in the exponential has not the interpretation of a physical energy, but we will call it "energy" as well, for simplicity. When dynamics are time-translation invariant ("stationarity"), Gibbs distributions are obtained by maximizing the statistical entropy under the constraint that the average of the observables defining the energy is fixed (Maximum Entropy Principle, MEP), but their definition via the equivalence with variable length Markov chains allows for non-stationary situations.

Using Gibbs distributions to analyze retina data and population coding has shown great success within the last decade. In particular, several important results have been obtained by using the MEP for an energy having the form of an Ising model, i.e., taking into account instantaneous pairwise interactions between neurons [2]. Extensions to more general energy forms have been considered too (triplet interactions [6], time delayed interactions [7]). In particular, we have developed efficient algorithms and soft-

ware, PRANAS, [8] allowing us to fit the parameters of a Gibbs distribution (whose energy form is given) from MEA data.

This "Gibbs" approach is appealing for a physicist. It would allow us to apply the powerful techniques and concepts from statistical physics to the analysis of the neural code. In addition, showing a canonical form of energy fitting well with retina data could be a step towards the "thermodynamics" of the retina: to explain the dynamics of a large population of RGCs by combining a few canonical observables. However, this approach raises several deep questions.

- **Which energy form?** In contrast to statistical physics/thermodynamics, the energy form for the retina cannot be inferred from first principles, so researchers are reduced to guess the form. Unfortunately, a mathematical analysis based on the mapping between Markov chains describing the neuronal dynamics and Gibbs distribution shows that the corresponding energy generically has a plethora of highly redundant observables [4]. We have proposed a method to eliminate these redundant terms from data analysis using information geometry, and we have shown experimentally that the degree of redundancy depends on the visual stimulus correlations [9].
- **Non stationarity.** Most Gibbs approaches, based on MEP, use the assumption of stationarity. To the contrary, the retina mainly responds to changes in a visual scene, i.e., transient, non-stationary stimuli. The MEP does not extend to this case. We have developed an approach, based on linear response theory, where a time-dependent stimulus is viewed as a perturbation of a stationary state (spontaneous activity) that can be characterized from data using MEP. In this case, the response to the stimulus can be written in terms of correlations of the stationary case (this an extension of the fluctuation-dissipation theorem of physics) [10].
- **Decoding.** Assume we are able to characterize the population statistics of RGC with a Gibbs distribution, how can we use it to decode the visual stimulus? Although some promising approaches have been proposed, this question seems far from being solved.

## 4 Retinal waves, retinal development and non linear dynamics

Immediately after birth the visual system of vertebrates is not yet effective. A complex, transient sequence of dynamical processes takes place starting a few days before birth, progressively enabling "the eyes to see" and stopping when vision is functional. A large part of this processing is due to waves of

electric activity ("retinal waves") spreading through the retina with a characteristic periodicity. This macroscopic phenomenon (i.e., occurring at the scale of the whole retina) originates from microscopic processes starting at the molecular level (ionic channels), inducing bursts of activity in specific cells, and spreading through the retina by virtue of cell connectivity. Retinal waves are classified into 3 consecutive stages, each having a specific role in visual system development. The transition between stages results from genetically programmed morphological changes. However, a part of this spatio-temporal activity and its transformation during development can be explained by generic mechanisms in nonlinear dynamics, as we describe here, focusing on stage II. This section is a summary of D. Karvouniari's thesis [11, 12], work conducted in collaboration with Institut de la Vision and InPhyNi (L. Gil).

Stage II retinal waves are due to spontaneous and periodic bursts of activity of specific retinal cells, the starburst amacrine cells (SACs), coupled by the excitatory neurotransmitter, acetylcholine (ACh). When a SAC is active (bursting) it releases acetylcholine; this can trigger the activation of post-synaptic cells. The membrane potential  $V$  of SAC  $i$  can be modeled as:

$$C \frac{dV_i}{dt} = I_{ion}(V_i, \bullet) + I_{sAHP}(V_i, R_i) + I_{ACh}(V_i, A_j), \quad (1)$$

where  $C$  is the membrane capacitance. The term  $I_{ion}(V, \bullet)$  represents the sum of ionic currents involved in SACs bursting (mainly calcium and potassium), and depending on additional dynamical variables represented, for simplicity by the symbol  $\bullet$  (see [11] for details);  $I_{sAHP}(V_i, R_i)$  is a slow hyperpolarization potassium current, depending on a refractory variable  $R_i$  controlled by a cascade of kinetic processes; finally,  $I_{ACh}(V, A_j)$  is the sum of excitatory acetylcholine currents due to active pre-synaptic cells  $j$  connected to  $i$ .

A bifurcation analysis of the model (1) shows that SACs can switch, by a saddle-node bifurcation, from a rest state to fast oscillations in the order of milliseconds (bursting). This arises when the current  $I_{tot} = I_{sAHP} + I_{ACh}$  crosses from below a threshold value  $I_{SN}$ , depending on biophysical parameters (conductances, reversal potentials, etc.). Reciprocally, when the cell is bursting, it can go back to a rest state, by a homoclinic bifurcation, if  $I_{tot}$  crosses from above a threshold value  $I_{Hc}$ . In general,  $I_{Hc} < I_{SN}$  but they differ by a few pA, so, for simplicity, we identify them from now. Thus, in short:

$$\text{if } I_{tot} = I_{sAHP} + I_{ACh}, \begin{cases} < \theta, \text{SAC is at rest,} \\ > \theta, \text{SAC is active.} \end{cases} \quad (2)$$

The transition from rest to active is due to excitation from pre-synaptic active cells, via the excitatory current  $I_{ACh}(V, A_j)$ . The transition from active to

rest is due to the slow hyperpolarization current  $I_{sAHP}(V_i, R_i)$  (having a negative sign). Indeed, when the cell is active, a complex mechanism involving calcium takes place,  $I_{sAHP}(V_i, R_i)$  becomes more and more negative, leading the cell, after a few seconds and via a bifurcation, to a hyperpolarized rest state where it can not be excited for a long period (in the order of one minute), independently of the excitatory current  $I_{Ach}$  provided by the other cells.

Thus, wave propagation is due to a transition from rest to active state of SACs transmitted via Ach interactions. Waves are stopped by hyperpolarized regions corresponding to cells that have burst in a former wave. Therefore, each wave has to propagate into a landscape, imprinted by previous waves, with refractory regions and excitable regions. This landscape evolves slowly in time, on time scales that are longer than the SAC refractory period. This generates a spatial anisotropy where some cells are more active ("leaders") and some others more refractory. In this way, the mere dynamics generate a huge spatio-temporal variability, even if the cells are initially identical. This (biologically observed) variability is purely dynamical and does need to add extra mechanisms to be explained.

A non-linear wave propagation equation can be obtained, upon several approximations, considering SACs are located on a  $d$ -dimensional regular lattice, with spacing  $a$ , and nearest-neighbours interactions. The Ach conductance,  $\Gamma$ , considered now as a field in a  $d$ -dimensional continuum, obeys:

$$\frac{\partial \Gamma}{\partial t} = -\mu \Gamma + 2d\Omega H[\Gamma - \Gamma_c(R)] + a^2 \Omega \Delta H[\Gamma - \Gamma_c(R)], \quad (3)$$

where  $\mu$  is the Ach degradation rate,  $\Omega$  the Ach production rate;  $\Delta$  is the Laplacian operator;  $H$  is the Heaviside function, mimicking the threshold effect (2), and  $\Gamma_c(R)$  is the critical threshold, derived from the bifurcation condition (2) in a refractory landscape characterized by the variable (field)  $R$  and depending upon the network history. This is a singular equation because one applies a Laplacian to a Heaviside function. It is however possible to smooth the Heaviside function to eliminate this singularity. This equation can be solved for simple refractory landscapes, but the general situation where  $R$  is a random landscape imprinted by waves history, is still under investigation.

The process of wave generation and propagation bares some similarity to forest fires introduced in the context of Self-Organized Criticality (SOC). SOC systems have the ability to self-organize into a state where characteristic events (avalanches) have power law distributions. This has lead some researchers to hypothesize that the retinal wave distribution (size or duration) could follow a power law [13]. Experimental evidence is not convincing though and would deserve a more elaborate analysis. Interestingly, eq.

(3) corresponds to a continuum limit of a SOC model (a sandpile) if the term  $-\mu\Gamma + 2d\Omega H[\Gamma - \Gamma_c(R)] = 0$ . This is very specific and non-generic situation. As a consequence, in our model, wave distributions are exponentials, except at a specific curve in the parameter space, given by this specific relation and related to the bifurcation condition (2); there the distribution is a power law. This suggests that SACs do not organize in a critical state unless some additional mechanism is added (like homeostasy), driving them towards the critical curve.

This model provides an example where one can construct the path from the molecular scale to the neuronal scale, to the macroscopic scale. The mathematical analysis allows us to explain bursting of SACs and wave propagation with simple mechanisms in nonlinear dynamics. In addition, it allows us to explicitly compute several important quantities, such as the wave speed.

But the main interest is the closeness to experiments. The model not only reproduces experimental facts, it also leads us to experimental predictions, some of which are on the way to be experimentally confirmed (see [11,12] on the role of kV3 channels on bursting of SACs during stage II). In particular, we are able to characterize how retinal wave structure is evolving during development when synaptic connections are modified. Likewise, the model is accurate enough to explain pharmacological manipulations (e.g., channels or synaptic terminal blocking).

## 5 Conclusion and perspectives

In this paper, I have given examples of research where concepts and methods from theoretical physics are used to understand retinal dynamics and how it encodes information. I would like now to briefly present further ongoing developments.

**Amacrine cells and motion processing.** When an object moves across the visual field our visual system is able to interpolate its trajectory and to filter much spurious information: eye-head-body movements, motion of the background. In particular, anticipation is absolutely essential to compensate the time lag of 30 – 100 ms between the reception of photons in the retina and the response of the visual cortex. Part of the anticipation process starts in the retina and is explained by the non-linear response (gain control mechanism) of bipolar and ganglion cells [14]. This does not take into account the lateral connectivity of amacrine cells, which play an important role in

motion processing (differential motion, approaching motion, etc.). We want to understand the possible role of amacrine cells lateral connectivity in the retina in processing complex motion. In particular, we are seeking a specific transient signature in RGC correlations, in response to a moving object. We believe that the correlated response could provide more efficient processing of the object motion, especially trajectory anticipation and interpolation. We want to validate this hypothesis at the modelling level (PhD thesis of Selma Souihel) and experimental level, in collaboration with the Institut de la Vision and Institut des Neurosciences de la Timone, in the context of the Trajectory ANR.

**Effect of pharmacologically switching a population of RGCs.** At present, over 30 RGC sub-types have been identified, typically on the basis of common anatomical features or basic functions (e.g., sensitivity to motion, orientation, motion direction etc.). In collaboration with the University of Newcastle, in the context of E. Kartsaki's thesis, we want to investigate how different groups of RGCs contribute to the encoding of visual scenes. The project uses a pharmacogenetics approach (combined with MEA physiology, anatomy, computational modelling and behaviour) to reversibly silence sub-groups of RGCs sharing gene expression through specific drugs (DREADD) activation. Removing an entire functional RGC group from the population response will shed light on the role these same cells play in population encoding of complex visual scenes and identify which information is lost, locally and globally.

## References

1. T. Gollisch and M. Meister. *Neuron*, 65(2):150–164, January 2010.
2. E. Schneidman, M.J. Berry, R. Segev, and W. Bialek. *Nature*, 440(7087):1007–1012, 2006.
3. R. Cofré and B. Cessac. *Chaos, Solitons & Fractals*, 50(13):3, 2013.
4. R. Cofré and B. Cessac. *Phys. Rev. E*, 89(052117), 2014.
5. J. W. Pillow, Y. Ahmadian, and L. Paninski. *Neural Comput*, 23(1):1–45, 2011.
6. E. Ganmor, R. Segev, and E. Schneidman. *The journal of neuroscience*, 31(8):3044–3054, 2011.
7. J.C. Vasquez, O. Marre, A. Palacios, M.J Berry, and B. Cessac. *J. Physiol. Paris*, 106(3-4):120–127, May 2012.
8. B. Cessac, P. Kornprobst, S. Kraria, H. Nasser, D. Pamplona, G. Portelli, and T. Viéville. *Frontiers in Neuroinformatics*, 11:49, 2017.
9. R. Herzog, M.J. Escobar, R. Cofré, B. Cessac, and A. Palacios. networks. *PNAS (submitted)*, 2018.
10. B. Cessac and R. Cofré. submitted to *Journal of Mathematical Biology*, 2018.
11. D. Karvouniari, L. Gil, E. Orendorff, O. Marre, S. Picaud, and B. Cessac. *Scientific Reports, submitted*, 2018.

12. D. Karvouniari. *Retinal waves: theory, numerics, experiments*. PhD thesis, EDSTIC, 2018.
13. M.H. Hennig, C. Adams, D. Willshaw, and E. Sernagor. *J Neurosci*, 2009.
14. M.J. Berry, I.H. Brivanlou, T.A. Jordan, and M. Meister. *Nature*, 398(6725):334—338, 1999.

# Modeling and computation of a liquid-vapor bubble formation

André Galligo, Frédéric Lesage, Sebastian Minjeaud

**Abstract** The Capillary Equation correctly predicts the curvature evolution and the length of a quasi-static vapour formation. It describes a two-phase interface as a smooth curve resulting from a balance of curvatures that are influenced by surface tension and hydrostatic pressures. The present work provides insight into the application of the Capillary Equation to the prediction of single nucleate site phase change phenomenon. In an effort to progress towards an application of the Capillary Equation to boiling events, a procedure for generating a numerical solution in which the computational expense is reduced, is reported.

## 1 Introduction

Boiling is a complex phase transitioning process in which a new liquid-vapor interface (bubbles) is created. It is an effective mechanism widely used in energy conversion industrial facilities. However, a precise descriptive/predictive model of bubble formations is needed to better understand

---

André Galligo  
Université Côte d'Azur, CNRS, Inria, LJAD, France.  
e-mail: [galligo@unice.fr](mailto:galligo@unice.fr)

Frederic Lesage  
Université Côte d'Azur, Center of Modeling, Simulation and Interactions.  
e-mail: [Frederic.Lesage@unice.fr](mailto:Frederic.Lesage@unice.fr)

Sebastian Minjeaud  
Université Côte d'Azur, CNRS, Inria, LJAD, France.  
e-mail: [Sebastian.Minjeaud@unice.fr](mailto:Sebastian.Minjeaud@unice.fr)

the heat transfer characteristics. As an important first step, the question can be addressed from a quasi-static viewpoint. Indeed, at the interface, a classical conservative law governs the surface curvature of the generated bubble. This non-linear law links the difference of pressure and the surface tension effect. After normalization, it can be expressed at each point of the surface by the following equation:  $\kappa_1 + \kappa_2 - Bz = \text{constant}$ ; where  $B$  is a Bond number, summarizing the context,  $z$  is the elevation and  $\kappa_1 + \kappa_2$  is twice the Gaussian mean curvature. Therefore, the study of a growing bubble is amenable to solving geometric computations and non-linear differentiable equation. The main difficulty is to design criteria to detect when the growing bubble will detach from the substrate's nucleation site. Inspired by experimental observations, the second author was able to develop a successful computational strategy [1,2]. The computational model implemented for the axisymmetric case (which relies on 2D geometric computations), provides useful information, fully confirmed by experimental observations. Moving forward, we were able to speed up the computations and introduce the use of splines for representing the plane section of the surfaces.

In future work, we will address with similar tools the case for which the nucleation site is on an inclined plane; this geometry better models the one effectively used in industrial plants. Our next target is to better formalize our detachment criteria, in collaboration with an experimental team in Dublin, Ireland; then develop and implement a 3D model for a more general situation. Future studies will also include external stress terms such as cross flows and electrical fields in an effort to move towards realistic and accurate boiling models.

## 2 Young-Laplace Equation and Capillary Equation

We consider an infinitesimal section of a vapour formation interface defined by two principal radii of curvature in perpendicular planes, as illustrated in Fig. 1. We suppose that the work done on the surface is considered to be equal to the work attributed to the pressure difference, as expressed by the Young-Laplace Equation:

$$\Delta p = \sigma(\kappa_1 + \kappa_2) \quad (1)$$

in which  $\kappa_1$  and  $\kappa_2$  are the curvatures corresponding to the principal radii of curvature in orthogonal planes, and  $\sigma$  is defined as the work per unit area required to produce an area variation of the interface.

Applying the Young-Laplace pressure balance to the context of a single vapour formation event, we consider a surface that is axisymmetric. The

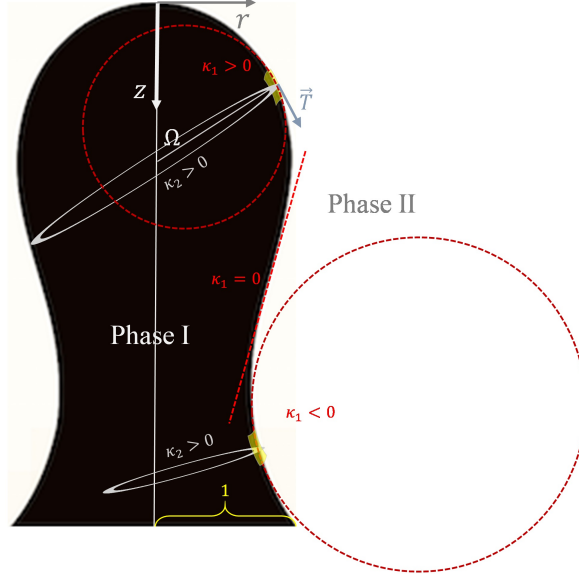


**Fig. 1** Axisymmetric surface with smooth contour.

surface can thus be described by a smooth curve  $\mathcal{C}$  that defines the two-phase interface, as illustrated in Fig. 1. The horizontal coordinate is denoted by  $r$  and the vertical one, oriented downward from the apex, by  $z$ . We normalize the problem by imposing a foot radius of unity, in other words the point  $(\eta, 1)$  belongs to the curve  $\mathcal{C}$ .

The curvature  $\kappa_1$  is in the  $z - r$  plane and the curvature  $\kappa_2$  is in the plane orthogonal to the tangent unit vector  $\mathbf{T}$ . Due to symmetry, the curvatures are equal at the apex origin, they are denoted by  $\kappa_0 = \kappa_1 = \kappa_2$ . Let  $g$  be the gravitational constant and  $\Delta\rho$  the difference in density between the two phases, (1) implies the capillary equation:

$$2\sigma\kappa_0 - \Delta\rho gz = \sigma(\kappa_1 + \kappa_2), \quad \text{on } \mathcal{C}. \quad (2)$$

Introducing a dimensionless Bond number,  $Bo = \Delta\rho r(\eta)^2 g / \sigma$ , we get the adimensionalized form of the capillary equation:

$$2\kappa_0 = \kappa_1 + \kappa_2 + Bo \cdot z, \quad \text{on } \mathcal{C}. \quad (3)$$

## 2.1 Strategy for Solving the problem

By choosing a parametrization of the curve  $\mathcal{C}$  and explicit expressions of the curvatures, the equation (3) can be expressed as a second order Ordinary Differential Equation (ODE) with a free parameter  $\kappa_0$  (the Bond number being determined by the physical properties of the two fluids). In order to simplify the bubble detachment problem, we decompose the difficulty by fixing a positive value for the parameter  $\eta$  and we consider the corresponding sub-problem with the following boundary conditions:

$$(0,0) \in \mathcal{C} \quad ; \quad (\eta,1) \in \mathcal{C} \quad \text{and} \quad \frac{dz}{dr} = 0 \text{ at the apex.} \quad (4)$$

Numerical procedures allow us to compute a candidate curve solution for each value of the fixed parameter  $\eta$ . Roughly speaking, two boundary conditions are needed to determine the curve from the second order ODE (3) while the third one determines a value for the free parameter  $\kappa_0$ . So, we obtain a family of curves depending on the parameter  $\eta$ . Then we need a criterion to select the curve that best models the (physical) bubble detachment phenomena. We claim that the detachment profile is identified by noting that at a given height  $\eta$ , below a threshold, one smooth curve satisfies the boundary conditions (4) with at most one inflexion point. This is illustrated in Fig. 2.

The detachment height is then deduced through incremental increases in the parameter to maximize the height  $\eta$  till this property can be satisfied.

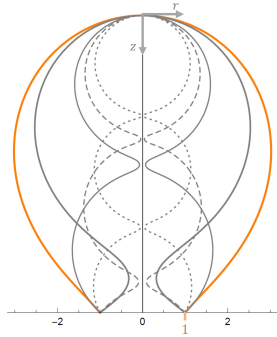


Fig. 2 Set of curves satisfying (3) with the boundary conditions (4) for fixed values of  $\eta$

## 2.2 First numerical procedure

This first method is an established approach [1, 3]. The half (smooth) curve  $\mathcal{C}$ , is divided in two parts: first a graph of a function  $r(z)$  near the apex, then a graph of a function  $z(r)$  till the foot. Expressing the curvatures  $\kappa_1$  and  $\kappa_2$  in each case, relying on differential geometry formulas, gives rise to a pair of ODEs:

$$2\kappa_0 = \frac{z''(r)}{(z'(r)^2 + 1)^{3/2}} + \frac{z'(r)}{r\sqrt{1 + z'(r)^2}} + Bo \cdot z(r) \quad (\text{ODE1})$$

and

$$2\kappa_0 = \frac{-r''(z)}{(r'(z)^2 + 1)^{3/2}} + \frac{1}{r(z)\sqrt{1 + r'(z)^2}} + Bo \cdot z \quad (\text{ODE2})$$

For each  $\eta$ , we first choose a value of  $\kappa_0$ . We integrate (ODE1) with the initial boundary conditions  $z(0) = 0$  and  $z'(0) = 0$ . This is done till some value  $r_1$  of  $r$  such that  $z'(r_1) = 1$ . We denote by  $z_1 = z(r_1)$ . Then we integrate (ODE2) with the initial boundary conditions  $r(z_1) = r_1$  and  $r'(z_1) = 1$ . This second integration is done until  $z = \eta$ . The  $r(\eta)$  is computed, it will serve for a shooting method. Indeed, performing this process for different values of  $\kappa_0$ , allows to find a minimum value of  $\kappa_0$  for which  $r(\eta) = 1$ .

This numerical approach was successfully implemented using the software Mathematica.

## 2.3 Second numerical procedure

The half (smooth) curve  $\mathcal{C}$  is represented by a kind of arc-length parameterization ( $0 \leq t \leq 1$ ):  $r(t), z(t)$  with  $|r'(t)|^2 + |z'(t)|^2 = \lambda^2$ , depending on a new parameter  $\lambda$ . Again, we can express  $\kappa_1$  and  $\kappa_2$ , by similar differential geometry formulas, which provide a system of ODE with respect to the variable  $t$ :

$$\begin{cases} 2z'(t)r(t)z''(0) = -\lambda r(t)r''(t) + \lambda z'(t)^2 + Bo\lambda^2 z(t)z'(t)r(t), \\ r'(t)^2 + z'(t)^2 = \lambda^2. \end{cases} \quad (5)$$

The boundary conditions can be expressed as

$$(r(0), z(0)) = (0, 0), \quad (r(1), z(1)) = (1, \eta), \quad z'(0) = 0.$$

Now, we can approximate the functions  $r(t)$  and  $z(t)$  by cubic spline functions on a subdivision of the interval  $(0, 1)$  and express the Boundary Value

Problem as a polynomial system of equations, which can be solved by standard techniques. The unknowns of the system are the coefficients of the two splines  $r$  and  $z$  and the parameter  $\lambda$ .

This second numerical approach was implemented using the software Scilab and is quite efficient since, for a given Bond number, it converges in few iterations of the nonlinear solver. Obviously, the curves obtained by the two numerical methods agree very well. Numerical results obtained with the second approach using a regular subdivision of 50 cells are presented in Fig. 3: at left, for a Bond number equal to 0.0052, the detachment height is estimated to 15.47 whereas at right, for a Bond number equal to 0.047, it is estimated to 7.90.

This second approach is still amenable when we replace the maximization parameter  $\eta$  by the volume of the bubble, an *a priori* more relevant physical quantity. The details will be given in a forthcoming article.

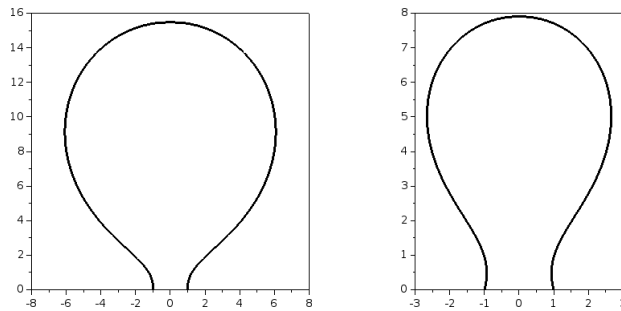


Fig. 3 Numerical solutions obtained for  $Bo = 0.0052$  (left) and  $Bo = 0.047$  (right)

### 3 Conclusion

Two numerical methods that solve the capillary equation are reported. The objective of the numerical treatments is to generate curves that model the interface of vapour formations growing from a nucleation site. The first method is an established approach and is used here to provide context and clarity to the solution procedure. The second method is a new refinement to the numerical solution of the Capillary equation. By implementing splines into the procedure, it reduces the computational expense and presents a stepping stone towards more accurate heat transfer predictions of single boiling events.

## Acknowledgments

This work has been supported by the French government, through the UCA-JEDI Investments in the Future project managed by the National Research Agency (ANR) with the reference number ANR-15-IDEX-01.

## References

1. F. J. Lesage and F. Marois. Experimental and numerical analysis of quasi-static bubble size and shape characteristics at detachment. *International Journal of Heat and Mass Transfer*, 64:53–69, 2013.
2. F. J. Lesage, J. S. Cotton, and A. J. Robinson. Analysis of quasi-static vapour bubble shape during growth and departure. *Physics of Fluids*, 25(6):067103, 2013.
3. D. Gerlach, G. Biswas, F. Durst, and V. Kolobaric. Quasi-static bubble formation on submerged orifices. *International Journal of Heat and Mass Transfer*, 48(2):425 – 438, 2005.



## New paradigms in nuclear human decorporation using macromolecular systems

Laurane Léost, Florian Lahrouch, Christophe Den Auwer, Christophe Di Giorgio and coworkers.

**Abstract** Actinides elements (that are all radioactive) are the subject of special attention considering the important amount that has been produced for military and civil applications. They often present a dual toxicity: chemical and radiotoxicological from  $\alpha$  and  $\beta$  decay. In case of dissemination during an accidental nuclear event, the consequences of contamination can initiate the vital process. Ingestion, inhalation and then retention in the target organs will occur. Currently, the golden standard of decorporation is DTPA (diethylenetriaminepentaacetic acid) injected intravenously. It presents a strong complexing constant for some actinides but poor chemical specificity and it is only valid for removing actinides from blood, immediately after contamination. Objectives are to explore the design of biocompatible nanoparticles or macromolecules able to release the decorporation agent directly into the target organ. This should constitute a new class of decorporation agents.

---

Laurane Léost, Florian Lahrouch, Christophe Den Auwer e-mail: [christophe.denauger@unice.fr](mailto:christophe.denauger@unice.fr), Christophe Di Giorgio  
Université Côte D'Azur, CNRS, Institut de Chimie de Nice, Parc Valrose 06108, Nice, France.

We would like to thank for their collaboration to this work Jean Aupiais, CEA, DAM, DIF, 91680 Bruyères le Châtel, France; Christoph Hennig, Helmholtz-Zentrum Dresden-Rossendorf, Institute of Resource Ecology, 01328 Dresden, Germany; and Anne Van Der Meeren CEA/DSV Laboratoire de RadioToxicologie, Bruyères le Châtel, 91297 Arpajon, France.

## 1 Context

Since the discovery of nuclear fission in the middle of the 20th century, actinide elements have been studied continuously. This family of unstable elements, of which uranium and plutonium are the two most famous representatives, has marked the history of science and humanity. Currently uranium and plutonium are strategic resources exploited at an industrial level. Schematically, these two radioactive elements are used for the production of electrical energy and for the manufacture of atomic weapons. The past use of nuclear weapons (atmospheric and submarine tests, Hiroshima and Nagasaki bombs) and industrial nuclear accidents (Chernobyl, and Fukushima mainly) have resulted in significant environmental pollution and human contamination. In the current context, the risk of actinide dispersion is still present, and possible cases of internal contamination may mainly affect nuclear workers or soldiers.

In case of internal contamination, plutonium and uranium can be distributed to organs via the bloodstream. Plutonium (Pu) in its oxidation state +IV under atmospheric conditions is retained mainly by the bones and liver. The soluble forms of Pu(IV) may be taken up by iron proteins while the insoluble forms are supported by the reticuloendothelial system. Uranium (U), on the other hand, is mostly found in its dioxo-cationic form, uranyl  $\{UO_2^{2+}\}$  at oxidation state +VI and preferably targets the mineral part of the bone matrix (hydroxyapatite). In summary, skeleton, liver and kidney that are the primary target organs for actinide retention can be damaged by radiotoxicity or chemical toxicity of these elements. The consequences of prolonged contamination are an increased risk of developing leukemia or (bone) cancer. In case of contamination with depleted uranium ( $^{238}U$ ) kidney dysfunctions may occur.

To promote actinide excretion and limit organ damage, chelating agents have been developed. They are called decorporation agents. At the present time, the calcium salt of diethylenetriamine pentaacetate (CaDTPA) is the standard chelating agent in France for Pu(IV) to promote blood elimination [1, 2]. Sodium bicarbonate, on the other hand, is the only countermeasure employed to favor U(VI) blood excretion and to limit kidney damage in case of acute uranium poisoning [3]. More recently, promising ligands for actinide(IV) and (III) decorporation have been developed based on catecholate (CAM) and hydroxypyridonate (HOPO) attached to spatially suitable molecular backbones [4]. The development strategy for such chelating molecules has long been based on optimizing affinity for actinides, which has allowed the development of chelating agents forming very stable complexes. But this strategy often lacks chemical selectivity with regards to biological cations that show similar chemical properties as actinides. This is the

case of Fe(III) for instance. Also, these molecular strategies for decorporation are of limited efficiency in removing actinides once incorporated in the target organs.

## 2 A new strategy

An alternative to the molecular strategy would be to enhance organ tropism and prevent accumulation. In that sense, polymeric chelates or nano-chelates may represent a real breakthrough in the actinides decorporation or protecting strategy because of their higher loading capacity (larger abundance of chelating sites per mg of polymer that could enhance uptake rates), but also their indirect vectorization properties correlated to a specific biodistribution into bone, kidney or liver [5]. We are currently exploring the use of phosphonate macromolecules in two systems: polyethyleneimine (PEI) as a polymeric chelator and chitosan (trimethyl chitosan, TMC) as a promising candidate for nanoparticle platforms. This strategy has already been applied to medical applications but never for actinide decorporation. For instance, the use, *in vivo*, of methylphosphonate functionalized polyethyleneimine (PEI-MP) for bone cancer imagery and scintigraphy has been reported [6]. We have proposed the use of PEI-MP for the chelation of Th(IV) and U(VI) in the specific case of bone contamination [7]. TMC on the other hand is biodegradable and therefore presents low toxicity for the human body [8]. We have proposed to develop a polyanionic chelating agent as a cross-linker for structuring the TMC into nanoparticles: the phosphonic analogue of DTPA, diethylenetriamine-pentamethylenephosphonic acid (DTPMP). The polycationic character of this polymer under physiological conditions improves tissue/cell adhesion and permeation, which leads to an increased residence time in biological systems. As a consequence, we have proposed TMC-DTPMP as a good candidate to be used as a drug delivery system for the specific case of lung epithelium [9]. Both systems are schematized in Figure 1.

Uranium in its natural isotopy (called  $^{Nat}U$ ) is a weakly radioactive nuclide that is easy to handle in our laboratory. Plutonium, however, is a strong chemical and radiological toxic whatever its isotopy. In this case thorium (Th) may be considered as a plutonium chemical analogue because it is stable at the unique oxidation state +IV and also because the specific activity of  $^{232}Th$  is comparable to that of natural uranium, which makes both of them easy to manipulate in the laboratory. Thorium has frequently been reported to mimic plutonium chemistry [10], although this must always be taken with caution. Thorium is also of interest by itself as the most concentrated natural

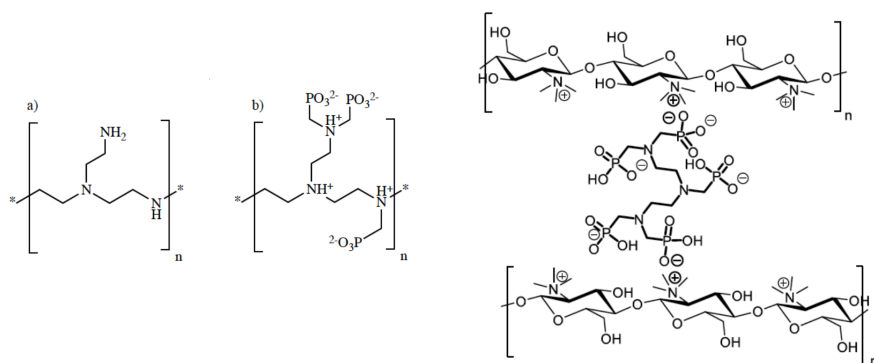


**Fig. 1** Left, representation of the monomeric unit of starting PEI (a) and PEI-MP (b) as if functionalization were equal to 100% and with an arbitrary protonation state; right, ionic cross-linking between TMC and DTPMP (with arbitrary protonated states).

actinide in the earth's crust and also because of its use a promising alternative fuel for the next reactor generation. In any case thorium is considered here as a preliminary step before investigating plutonium.

Uptake curves have been obtained with U, Th and each macromolecular system using a microfiltration technique followed by actinide quantification in the filtrate. The curve exhibits a linear increase up to a plateau, meaning that full complexation has occurred. For the U/PEI-MP system for instance, the plateau occurs for a monomer molar ratio of U: PEI-MP around 1.3 - 1.5 [7]. This corresponds to a maximum load comprised between 0.56 and 0.80 mg of uranium (elemental) per milligram of PEI-MP. For Th, the saturation regime that is not as clearly defined but would correspond to a maximum load comprised between 0.15 and 0.20 mg of thorium (elemental) per milligram of PEI-MP. For the Th/TMC-DTPMP system the resulting uptake curves for 10% DTPMP load corresponds to a maximum load of about 0.54 mg of Th(IV) (elemental) per mg of DTPMP [9]. Although different, these values are of the same order and exhibit the chelating capacity of the two platforms to chelate U(VI) and Th(IV) and more generally actinides at both oxidation states +IV and +VI.

In parallel, structural investigations have also been performed on both systems in order to decipher the coordination pattern of the actinide cation. X-ray Absorption Spectroscopy is a chemically selective spectroscopic technique that can probe local atomic arrangement, whatever the physical state of the sample. In order to better describe the actinide complexation site in both PEI-MC and TMC-DTPMP, Extended X-ray Absorption Fine Structure (EXAFS) spectra at the U, Th and Pu  $L_{III}$  edge were recorded (this corresponds formally to an electronic transition from 2p to nd states of the ac-

tinide). Measurements were conducted at the European Synchrotron Radiation Facility (ESRF) in Grenoble, at the ROBL beam line. As an example, one may describe the data obtained for uranyl complexed to PEI-MP. The first coordination sphere is composed of the short axial contribution of the two oxo bonds and of the longer equatorial contributions. The best fit metrical parameters for the equatorial uranyl plane are 4.7(2) equatorial oxygen atoms positioned at 2.35 Å (U-O<sub>eq</sub>). The second coordination sphere is composed by 3.3(5) phosphorous atoms at U...P = 3.77 Å. Both U-O<sub>eq</sub> and the U...P distances are typical distances for such phosphonate ligands as reported by Kubici *et al.* for a monodentate phosphate (U...O<sub>P</sub> = 2.28 Å and U...P = 3.64Å) [11].

Data obtained to date suggest that a macromolecular chelating approach to acting against actinide incorporation in target organs could be a valuable strategy. Studies aiming at determining the optimal molecular weight or size that directly impacts biodistribution and hence the toxicity and long-term kinetics experiments are also required to determine whether or not the actinide complexes could be naturally excreted with time. In a near future, the physical chemical approach presented above in model conditions will have to be complemented with biological assessments.

## References

1. WD Norwood. Therapeutic removal of plutonium in humans. *Health physics*, 8(6):747–750, 1962.
2. Guillaume Phan, Amaury Herbet, Sophie Cholet, Henri Benech, Jean-Robert Devierre, and Elias Fattal. Pharmacokinetics of dtpa entrapped in conventional and long-circulating liposomes of different size for plutonium decorporation. *Journal of controlled release*, 110(1):177–188, 2005.
3. Yasushi Ohmachi, Tomomi Imamura, Mizuyo Ikeda, Eriko Shishikura, Eunjo Kim, Osamu Kurihara, and Kazuo Sakai. Sodium bicarbonate protects uranium-induced acute nephrotoxicity through uranium-decorporation by urinary alkalinization in rats. *Journal of toxicologic pathology*, 28(2):65–71, 2015.
4. M Sturzbecher-Hoehne, GJ-P Deblonde, and RJ Abergel. Solution thermodynamic evaluation of hydroxypyridinonate chelators 3, 4, 3-li (1, 2-hopo) and 5-lio (me-3, 2-hopo) for uo<sub>2</sub> (vi) and th (iv) decorporation. *Radiochimica Acta International journal for chemical aspects of nuclear science and technology*, 101(6):359–366, 2013.
5. Jan R Zeevaart, Werner KA Louw, Zvonimir I Kolar, Elmaré Kilian, Frederika E Jansen van Rensburg, and Irene C Dormehl. Biodistribution and pharmacokinetics of variously molecular sized 117msn (ii)-polyethyleneiminomethyl phosphonate complexes in the normal primate model as potential selective therapeutic bone agents. *Arzneimittelforschung*, 54(06):340–347, 2004.
6. Neil V Jarvis, Jan Rijn Zeevaart, Judith M Wagener, Werner KA Louw, Irene C Dormehl, Rowan J Milner, and Elmaré Killian. Metal-ion speciation in blood plasma incorporating the water-soluble polymer, polyethyleneimine functionalised

- with methylenephosphonate groups, in therapeutic radiopharmaceuticals. *Radiochimica Acta*, 90(4):237–246, 2002.
7. Florian Lahrouch, Oleksandr Sofronov, Gaëlle Creff, André Rossberg, Christoph Hennig, Christophe Den Auwer, and Chirstophe Di Giorgio. Polyethyleneimine methylphosphonate: towards the design of a new class of macromolecular actinide chelating agents in the case of human exposition. *Dalton Transactions*, 46(40):13869–13877, 2017.
  8. Kuen Yong Lee, Wan Shik Ha, and Won Ho Park. Blood compatibility and biodegradability of partially n-acylated chitosan derivatives. *Biomaterials*, 16(16):1211–1216, 1995.
  9. L. Léost, L. Vincent, N. Sbirrazzuoli, J. Roques, A. Van De Meeren, C. Hennig, A. Rossberg, J. Aupiais, S. Pagnotta, C. Den Auwer, and C. Di Giorgio. *Submitted*.
  10. Konrad B Krauskopf. Thorium and rare-earth metals as analogs for actinide elements. *Chemical Geology*, 55(3-4):323–335, 1986.
  11. James D Kubicki, Gary P Halada, Prashant Jha, and Brian L Phillips. Quantum mechanical calculation of aqueous uranium complexes: carbonate, phosphate, organic and biomolecular species. *Chemistry Central Journal*, 3(1):10, 2009.

# Collective behaviours of light and matter

Thibaut Flottat, Frédéric Hébert and  
George Batrouni

**Abstract** Coupling of light and matter can lead to the emergence of new collective phenomena, which render a separate description in terms of light or matter impossible. To understand and describe such cases, new composite light matter objects need to be introduced. In this chapter, we present theoretical studies of two examples of such systems. The first is an assembly of coupled Rabi cavities that shows coherent behaviour similar to Dicke superradiance. The second is a Bose-Einstein condensate coupled to the optical modes of a cavity, that mediate an effective long range interaction between the atoms of the condensate and drive it into a supersolid phase.

## 1 Introduction

In quantum and condensed matter physics, light has always been used as a tool to manipulate and observe objects and phenomena. For example, in cold atoms experiments, electromagnetic (EM) fields are used to trap the atoms, to modify their mutual interaction through Feshbach resonances, and to impose all kinds of optical lattices upon them [1]. In solid state physics,

---

Thibaut Flottat, Frédéric Hébert, and George Batrouni  
Université Côte d'Azur, CNRS, INPHYNI, 1361 route des Lucioles, 06560, Valbonne,  
France, e-mail: [frederic.hebert@inphyni.cnrs.fr](mailto:frederic.hebert@inphyni.cnrs.fr).

We would like to thank, for their collaboration in this work, Laurent De Forges De Parny, Physikalisches Institut, Albert-Ludwigs Universität Freiburg, Hermann-Herder Straße 3, D-79104, Freiburg, Germany, and Valéry G. Rousseau, Physics Department, Loyola University New Orleans, 6363 Saint Charles Ave., LA 70118, USA.

photoemission spectroscopy [2] allows to determine the electron dispersion relations.

Beyond this, the coupling of light and matter can bring forth new collective behaviour where the observed phenomena, and the relevant degrees of freedom used to describe them, intricately mix both. When the light-matter coupling is strong, a separate description is not relevant, and new quantum objects emerge. For example, polaritons are quantum superpositions of a photon and a dipolar excitation of a solid medium. They behave as bosonic quasi-particles and can undergo Bose-Einstein condensation [3]. Similar collective light-matter phases can be observed in cold atoms experiments placed in optical cavities [4], for example Dicke superradiance [5] or crystallization [6]. In this chapter, we will exemplify such light-matter collective behavior by studying two cases.

First, we will consider the collective behaviour of coupled cavities. Each cavity is composed of an artificial atom coupled to the electromagnetic (EM) modes of the cavity. If the coupling is strong enough, the degrees of freedom of the atom and the EM field cannot be separated and these cavities, once connected to each others, are then new bricks to study collective behaviour. Quantum electrodynamic circuits are experimental realisation of such systems.

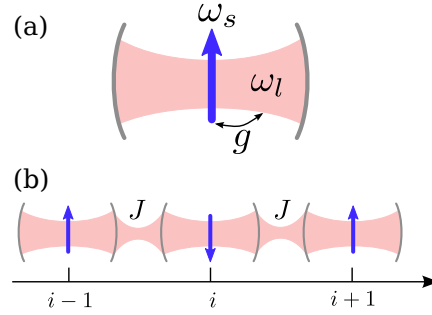
Secondly, we study an ensemble of atoms placed in a single cavity. The coupling with the field mediates an effective long range interaction between the atoms, that drives them into a supersolid phase, which exhibits simultaneous Bose condensed and charge density orders.

Both these studies present theoretical approaches to these problems. We use exact numerical techniques, quantum Monte Carlo (QMC) simulations with the SGF algorithm [7], supplemented by mean field techniques. The SGF method allows the calculation of many physical quantities, including complex correlation functions, at finite temperature on finite clusters.

## 2 Coupled cavities

Recently, it became possible to build elementary cavity quantum electrodynamics systems on solid state chips. For example a Josephson junction can play the role of an artificial atom and can be coupled to microwave photons localized in a small wave guide [8, 9]. A simple description of such cavities is based on the Rabi model. In this description, the material system is described as a two level quantum system, that is a spin 1/2, of excitation energy  $\omega_s$ . We neglect all of the EM modes but one, of energy  $\omega_l$ , and introduce a coupling strength between light and matter  $g$  (Fig. 1 (a)). Cavities

**Fig. 1** (a) The Rabi model, where a two level quantum system (spin) is coupled to a single EM mode, is the simplest model used to describe a cavity. (b) Coupling different cavities by tunnel effect, we obtain a QED circuit described by the so-called Rabi-Hubbard model.



are coupled to each other by tunnel effect of strength  $J$ , which gives a so-called circuit quantum electrodynamics (QED) system (**Fig. 1** (b)). Written in second quantized form, the Hamiltonian of the model reads

$$H = \sum_i \left( \omega_s \sigma_i^+ \sigma_i^- + \omega_l a_i^\dagger a_i + g (\sigma_i^+ + \sigma_i^-) (a_i + a_i^\dagger) \right) + J \sum_i (a_i a_{i+1}^\dagger + a_{i+1} a_i^\dagger) \quad (1)$$

$i$  is the index of the cavity, operators  $a_i^\dagger$  and  $a_i$  create and destroy a photon in cavity  $i$ ,  $\sigma_i^+$  and  $\sigma_i^-$  excite or de-excite the atom (spin) in cavity  $i$ . This model was dubbed Rabi-Hubbard model due to the presence of the tunnel effect term which is similar to those of Hubbard models in solid state physics. The tunnel effect term is diagonal in Fourier space. If the photons were decoupled from the atoms, the eigenstates would be plane waves and the eigenenergies would form a band, which is similar to what is observed for massive particles in lattices. The lowest energy state would be the state with wave vector  $k = 0$ . In the following we will concentrate on the resonant case where  $\omega_s = \omega_l = \omega$ .

This model has long been studied in the so-called rotating wave approximation (RW) (also known as the Jaynes-Cummings Hamiltonian). In this case, terms that do not conserve the total number of excitations  $N$  ( $N$  being the sum of the number of excited atoms and of the number of photons in the system) are neglected. Using this RW approximation, it was shown [10, 11] that a phenomenon similar to a photon blockade occurs, which was later observed experimentally [12]. In the photon blockade regime, the coupling between atoms and light is strong enough to stabilize a phase where, in each cavity, there is exactly one excitation, that is a quantum superposition of the excited atom and of a photon. The coupling  $g$  lowers the energy of such a state, which forbids other photons to come in the cavity. The different cavities are then decoupled, as photons are forbidden from tunneling from one

cavity to the next, which is similar to the Mott insulating phase observed in condensed matter physics. When the system is driven out of this phase by varying the parameters, the tunnel effect is once again allowed and light propagation throughout the system will yield long range phase coherence where photons and atoms will settle in the same state akin to a Bose-Einstein condensation.

While the RW approximation is valid for small  $g$ , it seems not to be when  $g$  becomes of the order of  $\omega$ , which is the regime that is now reached in circuit QED systems [9]. A mean-field study by Schiro *et al.* [13], taking into account the full Rabi-Hubbard Hamiltonian, showed that there would be no photon blockade. Taking into account the "counter rotating" (CR) terms (those which do not conserve the number of excitations) introduces fluctuations that destroy the blockade/Mott-like phase.

In our work [14], we studied the phase diagram of this system using exact SGF QMC simulations. It is challenging to treat exactly such systems as the number of particles changes and can become rather large. Other numerical techniques have difficulties tackling such problems. We confirmed the mean field predictions of [13] and derived the complete phase diagram of the Rabi-Hubbard model. The system adopts two phases (Fig. 2, left), depending on the Hamiltonian parameters: a phase where there is no coherence (but no blockade) dubbed a Rabi insulator and a phase where the systems becomes coherent, which is essentially the physics of the Dicke superradiant transition. In the incoherent phase, all correlation functions decay exponentially with distance between cavities, as in a photon blockade

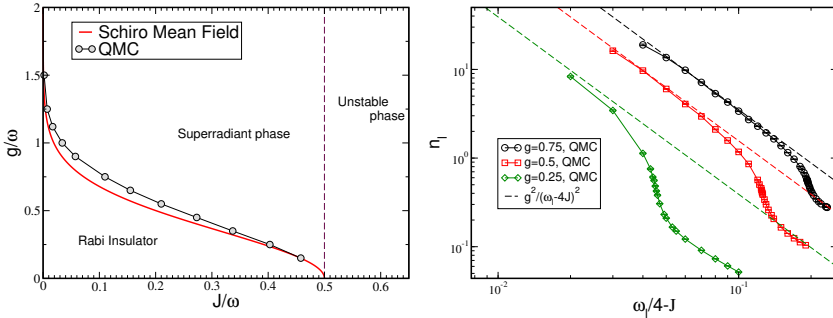


**Fig. 2** (left) The QMC phase diagram of the Rabi Hubbard model, compared with mean field results. We observe two phases: an incoherent Rabi insulator and a coherent superradiant phase. There is also a region where the system is unstable for  $J > \omega_1/2$ . (right) Density of photons in the system, as a function of  $-J$ . As  $J$  approaches the unstable region ( $J > \omega_1/4$  in this case), the density of photons diverges. As  $n_l$  becomes large, it reaches a mean field regime where  $n_l \simeq g^2 / (\omega_1 - 4J)^2$ . See [14] for details.

regime, but the density of excitations remains small and fluctuates, in other words the system is not gapped: It is compressible. As  $g$  and  $J$  are increased, one passes from the incoherent to the coherent phase. In the coherent phase, some correlation functions for both atoms and photons remain non zero at long distances, which means that this is collective phase where both matter and light become ordered at the same time. The density of photons becomes macroscopic in the  $k = 0$  Fourier mode, which means that they condense in one state, the atoms are then "synchronised" by the collective  $k = 0$  mode. Despite the fact that we have a band of photons mode, only the lowest energy one is relevant in that case, which is similar to the superradiant physics.

When the density of photons becomes large, the mean field predictions accurately describe the system (Fig. 2, right). For some parameters, the number of photons diverge and, beyond this limit, the Hamiltonian is not bounded (unstable region). We also studied variants of the Rabi Hubbard model to explore further the effect of the counter rotating terms on the physics of such systems [14].

In our equilibrium study, we did not find a blockade regime, except for some extreme parameters. With our Hamiltonian, the density of excitations grows with  $g$  but so do the fluctuations due to the counter rotating terms, which forbids the establishment of the blockade. On the contrary, in the RW approximation, the density of excitations is a conserved quantity, set independently of  $g$ , and we can have a large density with a value of  $g$  that is small to limit fluctuations. In experiments, that are made out of equilibrium, a similar effect happens as pumps set the density of excitations to the desired level, independently of  $g$ . However, when  $g$  is intrinsically large, we have shown that the RW description is not valid and that the full Rabi model must be used. This is the case for recent experiments that now reach the so-called ultrastrong coupling ( $g \simeq \omega$ ) or deep strong coupling ( $g > \omega$ ) regimes [9].

### 3 Bosons with cavity mediated interactions

The elusive supersolid phase has been proposed almost 60 years ago [15, 16] as a phase that shows both spatial ordering and superfluid (Bose condensed) properties. This is a priori contradictory as, in a Bose condensed phase, the particles are delocalized, which generates the long range phase coherence that is typical for this phase but smears any density pattern.

Recently, one of the first observation of such a phase has been achieved for condensed bosons in a cavity [17], as a collective light matter phase. The system is a two-dimensional condensed gas of cold atoms (Fig. 3, (left)) placed in an optical cavity. A cavity mode of wave length  $\lambda$  is pumped and a laser

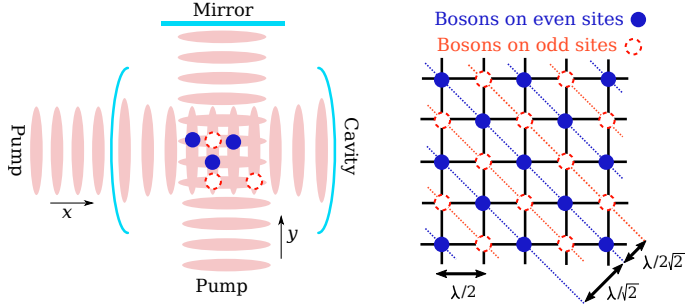


**Fig. 3** (left) In the experiment [17], a 2D gas of cold atoms is subjected to two perpendicular modes in a cavity. (right) The two optical modes are coupled if the atoms adopt a checkerboard pattern that provides the right wave planes to couple modes by scattering.

of the same wave length creates, by reflection on a mirror, a perpendicular standing wave mode. This creates a square optical lattice for the atoms to move into. But, if the atoms are placed with a checkerboard arrangement in this lattice, they scatter one mode into the other, which lowers the energy. There are two such checkerboard arrangements on odd or even sites of the square lattice (**Fig. 3**, (right)).

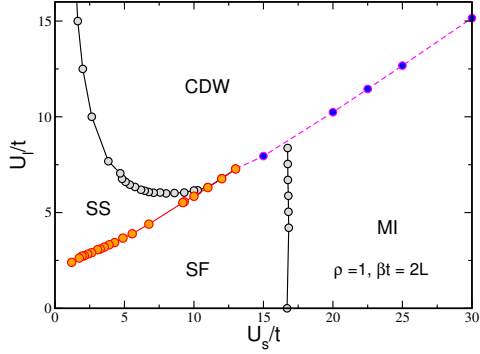
Integrating out the EM field yields an effective model for the atoms which reads

$$\hat{H} = -t \sum_{\langle i,j \rangle} (b_i^\dagger b_j + \text{H.c.}) + U_s \sum_i \frac{n_i(n_i - 1)}{2} - \frac{U_l}{L^2} \left( \sum_{i \in e} n_i - \sum_{i \in o} n_i \right)^2. \quad (2)$$

The  $b_i^\dagger$  and  $b_i$  operators create and destroy bosons on site  $i$  of a  $L \times L$  optical lattice while  $n_i$  is the boson number operator on site  $i$ . The  $t$  term propagates the particles in the lattice by tunnel effect between neighbouring sites  $\langle i, j \rangle$ .  $U_s$  is the strength of the on site repulsion between bosons. The  $U_l$  term is the interaction mediated by the coupling to the cavity modes that favours having particles either on the even ( $e$ ) sites or on the odd ( $o$ ) sites of the lattice. This is an infinite range interaction as all the particles are globally coupled. In this work, we concentrate on the physics of bosons, as the light degrees of freedom are integrated out in the description, but the observed phenomenon is in fact a collective phase of matter and light and a complete description requires to take both into account.

In our work [18], we derive the phase diagram of this model by QMC techniques, especially concentrating on the case where there is, on average, a density of one particle per site  $\rho = 1$ . This is the experimental case [17] although, in cold atom experiments, the density varies depending on the

**Fig. 4** The phase diagram for fixed density  $\rho = 1$  of one particle per site as a function of  $U_l$  and  $U_s$  is qualitatively similar to the experiments' findings [17].



position in the system, which yields some differences between experimental results and our theoretical study. This model was also studied using mean-field techniques [19,20].

The superfluid nature of the system is signalled by a finite density of condensed bosons  $n(\mathbf{k} = 0)$  in the  $\mathbf{k} = 0$  mode while the checkerboard patterns give a non zero structure factor (Fourier transform of the density correlations)  $S(\pi, \pi)$ . The phase diagram (**Fig. 4**), as a function of  $U_s$  and  $U_l$  ( $t$  sets the energy scale), includes four phases, that were observed experimentally:

- A superfluid (SF) Bose condensed phase at low interactions ( $n(\mathbf{k} = 0) \neq 0$ ,  $S(\pi, \pi) = 0$ )
- An incompressible homogeneous Mott insulator (MI) phase with one particle per site when  $U_s$  dominates ( $n(\mathbf{k} = 0) = 0$ ,  $S(\pi, \pi) = 0$ )
- a charge density wave phase with 2 particles on even sites and 0 on odd sites (or the reverse), which breaks the translation symmetry (dubbed CDW(2,0) phase) when  $U_l$  dominates ( $n(\mathbf{k} = 0) = 0$ ,  $S(\pi, \pi) \neq 0$ )
- a supersolid phase between the SF and CDW(2,0) phases with both an alternating density between even and odd sites and a phase coherence ( $n(\mathbf{k} = 0) \neq 0$ ,  $S(\pi, \pi) \neq 0$ ).

The same four phases were found in the experiment but the extent of the supersolid phase appears to be larger, compared to our data.

Numerically we explored other regimes, especially by varying the density. We found CDW phases with different patterns depending on the density : pattern (1,0) for  $\rho = 1/2$  and patterns (2,1) or (3,0) for  $\rho = 3/2$ . For moderate  $U_l$  (**Fig. 5** (a)), varying the density, we observe an alternation of superfluid regions, CDW phases for  $\rho = 1/2$  and  $\rho = 3/2$  that are surrounded by supersolid phases, as expected, and a Mott phase for  $\rho = 1$ . On the contrary, for large  $U_l$  (**Fig. 5** (b)) the cavity mediated interaction always impose the

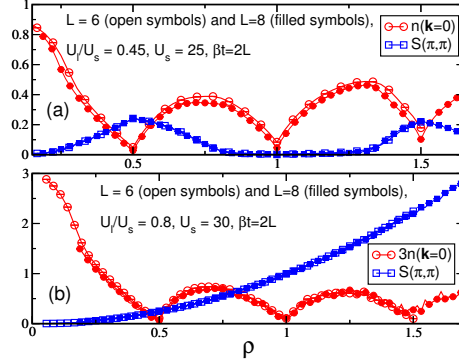


**Fig. 5** Varying density, we find different charge density wave, superfluid and supersolid phases. (a) For moderate  $U_l$  we find an alternation of phases with ( $S(\pi, \pi) \neq 0$ ) and without ( $S(\pi, \pi) = 0$ ) density modulation. (b) For large  $U_l$  there is always density modulation.

presence of a density modulation and we only observe CDW and supersolid behaviour ( $S(\pi, \pi)$  always  $\neq 0$ ).

We also analysed in detail the nature of the phase transitions between these different phases. In some cases, we observe first order phase transitions, which shows that the system is unstable towards phase separation, for example for  $\rho = 1/2$  (see [18] for details).

## 4 Acknowledgements

The authors thank B. Grémeaud, C. Miniatura, and T. Roscilde for useful discussions. This work was supported by the French government, through the UCAJEDI Investments in the Future project managed by the National Research Agency (ANR) with the reference number ANR-15-IDEX-01 and by Beijing Computational Science Research Center.

## References

1. *Many-body physics with ultracold gases*, by I. Bloch, J. Dalibard, and W. Zwerger, Rev. Mod. Phys. **80**, 885 (2008).
2. *Angle-resolved photoemission studies of the cuprate superconductors*, by A. Damascelli, Z. Hussain, and Zhi-Xun Shen Rev. Mod. Phys. **75**, 473 (2003).

3. *Exciton–polariton condensates*, by T. Byrnes, Na Young Kim, and Y. Yamamoto, *Nature Physics* **10**, 803 (2014).
4. *Cold atoms in cavity-generated dynamical optical potentials*, by H. Ritsch, P. Domokos, F. Brennecke, and T. Esslinger, *Rev. Mod. Phys.* **85**, 553 (2013).
5. *The Dicke Quantum Phase Transition with a Superfluid Gas in an Optical Cavity*, by K. Baumann, C. Guerlin, F. Brennecke, T. Esslinger, *Nature* **464**, 1301 (2010).
6. *Spontaneous Crystallization of Light and Ultracold Atoms*, by S. Ostermann, F. Piazza, and H. Ritsch, *Phys. Rev. X* **6**, 021026 (2016).
7. *Directed update for the Stochastic Green Function algorithm*, by V.G. Rousseau, *Phys. Rev. E* **78**, 056707 (2008).
8. *Strong coupling of a single photon to a superconducting qubit using circuit quantum electrodynamics*, by A. Wallraff, D.I. Schuster, A. Blais, L. Frunzio, R.-S. Huang, J. Majer, S. Kumar, S.M. Girvin, and R.J. Schoelkopf, *Nature* **431**, 162 (2004).
9. *Ultrastrong coupling regimes of light-matter interaction*, by P. Forn-Diaz, L. Lamata, E. Rico, J. Kono, and E. Solano, arXiv:1804.09275 (2018).
10. *Quantum phase transitions of light*, by A.D. Greentree, C. Tahan, J.H. Cole, and L.C.L. Hollenberg, *Nature Physics* **2**, 856 (2006).
11. *Mott-Insulating and Glassy Phases of Polaritons in 1D Arrays of Coupled Cavities*, by D. Rossini and R. Fazio, *Phys. Rev. Lett.* **99**, 186401 (2007).
12. *Observation of Resonant Photon Blockade at Microwave Frequencies Using Correlation Function Measurements*, by C. Lang, D. Bozyigit, C. Eichler, L. Steffen, J. M. Fink, A. A. Abdumalikov, M. Baur, S. Filipp, M. P. da Silva, A. Blais, and A. Wallraff, *Phys. Rev. Lett.* **106**, 243601 (2011).
13. *Phase Transition of Light in Cavity QED Lattices*, by M. Schiró, M. Bordyuh, B. Öztop, and H.E. Türeci, *Phys. Rev. Lett.* **109**, 053601 (2012).
14. *Quantum Monte Carlo study of the Rabi-Hubbard model*, by T. Flottat, F. Hébert, V. G. Rousseau, and G. G. Batrouni, *Eur. Phys. J. D* **70**, 213 (2016).
15. *Bose-Einstein Condensation and Liquid Helium*, by O. Penrose and L. Onsager, *Phys. Rev.* **104**, 576 (1956).
16. *Unified Theory of Interacting Bosons*, by E.P. Gross, *Phys. Rev. B* **106**, 161 (1957).
17. *Quantum phases from competing short- and long-range interactions in an optical lattice paper experimental*, by R. Landig, L. Hruby, N. Dogra, M. Landini, R. Mottl, T. Donner, and T. Esslinger, *Nature* **532**, 476 (2016).
18. *Phase diagram of bosons in a two-dimensional optical lattice with infinite-range cavity-mediated interactions*, by T. Flottat, L. de Forges de Parny, F. Hébert, V. G. Rousseau, and G. G. Batrouni, *Phys. Rev. B* **95**, 144501 (2017).
19. *Phase transitions in a Bose-Hubbard model with cavity-mediated global-range interactions*, by N. Dogra, F. Brennecke, S.D. Huber, and T. Donner, *Phys. Rev. A* **94**, 023632 (2016).
20. *Lattice bosons with infinite range checkerboard interactions*, by B. Sundar and E. J. Mueller, *Phys. Rev. A* **94**, 033631 (2016).



# Extreme and rare events in hydrodynamical and optical systems

Giovanna Tissoni and Eric Simonnet

**Abstract** Rare and extreme events are ubiquitous in nature and society, spanning from magnetic storms or particularly violent earthquakes, to market crashes or oceanic rogue waves. Different viewpoints are therefore possible: coming from two different communities, we will try here to bring together our ways to look at these events. After a very brief review of some recent results in our respective scientific domains, that is, non-equilibrium/statistical physics and nonlinear/dissipative optical systems, we draw some perspectives to develop a new approach using genetic algorithms to calculate extreme events in nonlinear dissipative optical systems.

## 1 Introduction

Nowadays, the modeling of complexity, in biology, geophysics or hydrodynamical turbulence for instance, involves systems with a huge number of degrees of freedom (d.o.f.) together with stochastic parametrisations. These parametrisations are needed, in general, to handle the physics at the microscopic/subgrid scale and to reduce the number of d.o.f. like in the Earth climate system, which involves multi-scale dynamics from a few meters to thousands of kilometers. Even more challenging, these systems are gener-

---

Giovanna Tissoni  
Université Côte d'Azur, Institut de Physique de Nice (INPHYNI), 1361, route des Lucioles  
06560 Valbonne, e-mail: [Giovanna.Tissoni@inphyni.cnrs.fr](mailto:Giovanna.Tissoni@inphyni.cnrs.fr)

Eric Simonnet  
INPHYNI, e-mail: [Eric.Simonnet@inphyni.cnrs.fr](mailto:Eric.Simonnet@inphyni.cnrs.fr)

ally far from equilibrium. Therefore, deterministic tools such as dynamical systems and bifurcation theory are not sufficient to handle these aspects. Nonequilibrium statistical physics appears to be the natural framework to study these phenomena.

It is often the case that physical systems exhibit phase transitions related to the existence of metastable states. The typical scenario is a system at equilibrium that exhibits (random) small-amplitude fluctuations. From time to time, some of these fluctuations might not be small and "push" the known (local) dynamics into another regime. These noise-induced transitions generally occur over a very short length of time. For many physical systems, it is particularly crucial to understand and predict these phase transitions, as they may have dramatic impacts to our societies.

The main aspect of this research is to use recent algorithmic tools for studying extreme and rare events in physics. These tools are not only able to compute the probability of these events but they also provide the physics associated to them. Even more importantly, they are able to overcome the so-called "curse of dimensionality" by handling systems with many d.o.f. These ideas were first proposed by J. Von Neumann (Manhattan project, unpublished) and developed in [1]. The first mathematical developments were obtained much later [2–5] and many others. The first successful applications in complex systems are very recent [6,7].

Roughly speaking, the idea is to mimic the evolution of species by performing Darwinian selections on the system dynamics, in a controlled (un-biased) way. These types of algorithms essentially perform a large number of mutations and selections (branching) by cloning the system dynamics. This is the reason they have sometimes been called *genetic algorithms* although they bear several different names (multilevel splitting, go-with-the-winner, rare event - large-deviation algorithms, etc.). In summary, these approaches are able to sample the system tail probability very efficiently. It thus allows us to compute rare or/and extreme events (see [7] for computing extremes), no matter the dimension of the system.

## 2 Phase transitions for atmospheric jets

In the recent years, it has been conjectured that a global climate change has occurred on Jupiter in the past century, which can be traced back to the 30's and the sudden disappearance of one of the atmospheric jets (similar to the North-Atlantic "jet stream" on Earth) [8]. In this work, we investigate phase transitions in a simple turbulent model of (barotropic) atmospheric jets. We are able to observe rare events corresponding to the absorption of a west-

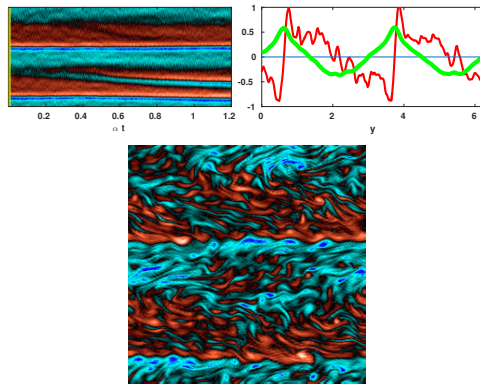


**Fig. 1** Phase transition for an atmospheric jet (nucleation): Hovmöller diagram (space vs. time) of the vorticity (left panel), zonal velocity and vorticity (right panel, green and red curves resp.). The lower panel is a snapshot of the vorticity 2-D field. The probability to observe this phenomenon is of the order  $10^{-7}$  in this case.

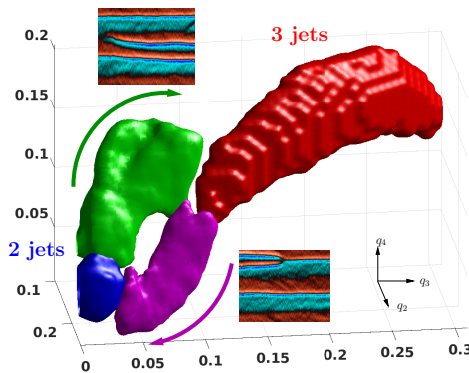


**Fig. 2** Finite-noise instanton concentrated along the most probable transition path between two-jet states and three-jet states.

ward jet into an eastward jet (coalescence) as well as the spontaneous creation of new eastward jets (nucleation). The statistics and the corresponding physics of these rare events are computed using a genetic algorithm called adaptive-multilevel splitting. This algorithm is exponentially faster than traditional tools (e.g., Monte-Carlo sampling) and allow for robust statistics of very low probability events. Figure 1 illustrates the creation of a new eastward jet. In addition, we can show that these transitions are controlled by an underlying instanton in the weak-noise limit (see Fig. 2). Therefore, it

suggests that only specific fluctuations along the instanton can yield such transitions and that predictors can be defined.

Although it is too early to relate this theoretical work with [8] we expect in the near future to consider more realistic models exhibiting the observed phenomenology. This is joint work with Freddy Bouchet at the Physics lab. ENS Lyon (in preparation).

### 3 Rogue waves in a laser with saturable absorber

In the recent years, extreme events in optics have been attracting a lot of interest, originating from the seminal paper by Solli *et al.* [9], due to the well-known analogy between optics and hydrodynamics, where rogue wave formation and prediction is a priority field of investigations. A huge body of literature has been blooming on this subject, studying rogue waves for many different optical systems (for a review, see [10–12] and references therein).

Optical fibers and fiber lasers are systems of choice for the analysis of optical rogue waves due to their natural longitudinal extension both for the conservative and the dissipative case. Dissipative rogue waves in laser devices have been also studied, and semiconductor systems have emerged as experimentally convenient test beds for the analysis of extreme phenomena. For instance, low dimensional semiconductor systems in which the wave envelope is severely constrained by boundary conditions served to demonstrate that the emergence of rogue events can be associated to an external crisis in a chaotic regime [13], thus showing the deterministic character of these extreme events.

Very recently, extreme events were studied both experimentally and numerically [14] in the intensity emitted by a monolithic broad-area vertical cavity surface emitting laser (VCSEL) with a saturable absorber with a linear pump (which reduces to one the transverse dimensions), and spatio-temporal chaos is claimed to be at the dynamical origin of extreme events.

Here we show numerical results about extreme events occurring in the field intensity emitted by a monolithic broad-area VCSEL with an intra-cavity saturable absorber [15], as the one used in the experiments on cavity solitons [14]. The system is displayed in the left panel of Fig. 3. The model we use is a set of 4 PDEs for the (complex) slowly varying envelope of the intra-cavity electric field, and the carrier populations in the active and in the passive material. The control parameters are the pump parameter  $\mu$  in the active medium, and the ratio  $r$  between the nonradiative lifetimes in the active and passive materials (for the model and the parameters we refer the reader to [15]).

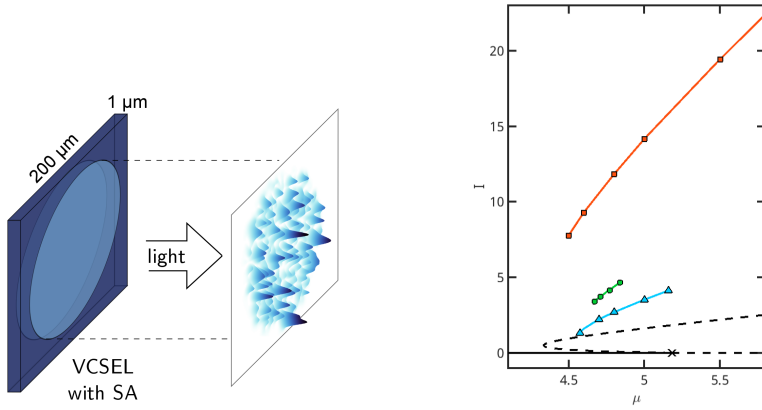


**Fig. 3** Left panel: scheme of the the system in study. Right panel: branches of solutions displayed for  $r = 1$  as a function of the control parameter  $\mu$  (injected current in the active medium, see text): homogenous stationary solution (dashed black line), stationary cavity solitons (blue line and triangles), time averaged maximum intensity of the turbulent state (orange line and squares) and of chaotic solitons (green line and circles). Note that the laser threshold is at  $\mu_{th} = 5.18$  (subcritical bifurcation).

In the right panel of Fig. 3 we show that below the lasing threshold the system may present multiple solutions, such as stationary cavity solitons (also called localised structures), oscillating or chaotic solitons and a global "turbulent" solution where the light intensity oscillates aperiodically in space and time, together with the trivial non-lasing solution. The turbulent solution survives above threshold, where it is the only attractor of the system. This solution has been associated (for the 1D case and for a slightly different set of parameters) to spatio-temporal chaos [14].

When the system is emitting on the "turbulent" solution, we perform a statistical treatment on the full set of 3D data of field intensity as a function of space and time. In contrast with previous literature about optical rogue waves in spatially extended systems [14, 16], we developed a numerical method for the individuation of the spatio-temporal maxima of the transverse field intensity in which each maximum appearing in the space profile is counted as an "event" only when its peak intensity reaches the maximum value also in time. This method allows a comparison, for example, with the hydrodynamical definition of "significant wave height", corresponding to the mean value of the wave height (from trough to crest) of the highest third of the waves.

The results of the statistical analysis are shown in Fig. 4, where the thresholds for RW are defined as follows:

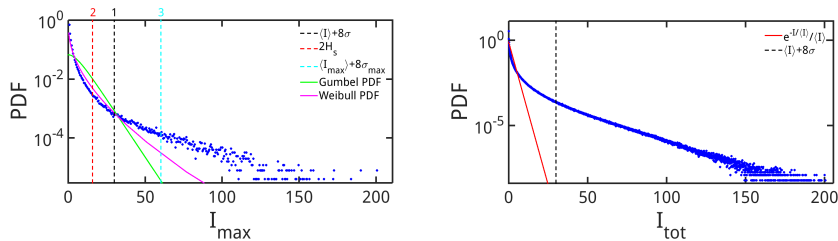


**Fig. 4** (a) PDF of the spatio-temporal maxima for a numerical simulation lasting 25 ns, for  $\mu = 7$  and  $r = 2.5$ . The green and magenta lines are respectively the Gumbel and Weibull distributions computed from the mean and standard deviation of the data. The three vertical dashed lines indicate three different definitions of rogue wave thresholds, defined in the text as thresholds 1,2 and 3 (see the legend, and the text). (b) PDF of all the values explored by the intensity during the simulation in each point of the transverse plane. Black dashed vertical line: threshold for rogue waves (same as threshold 1 in (a)). Here  $\mu = 5$  and  $r = 2.4$ . The presence of very heavy tails is clearly visible, and RW exist according to all the threshold definitions.

Threshold 1: the mean intensity, averaged on every point of the transverse plane and every instant in time, plus 8 times the standard deviation. This is the definition most commonly used for studying optical rogue waves in spatially extended systems [16, 17].

Threshold 2: two times the significant wave height  $H_s$ , defined as the average of the highest third of the spatio-temporal maxima values. This is the typical hydrodynamic definition, and permits one to get rid of a possible global increase of the average value, that would not correspond to a freak wave. The typical number of “events” detected during a simulation lasting 25ns is around  $6 \times 10^5$ .

Threshold 3: average of spatio-temporal maxima values plus 8 times the standard deviation.

We performed a statistical analysis of all the data (spatio-temporal maxima or total intensity) varying systematically the pump parameter  $\mu$  and the carrier lifetimes ratio  $r$ , and we could conclude that rogue waves are most probable below the lasing threshold (in the multistability region, see Fig.3) towards the lowest values of  $\mu$  (leftmost part of the turbulent branch) and for high values of  $r$ , meaning fast saturable absorbers.

Finally, in Fig. 5 we show an example of how a rogue wave looks like in the transverse plane, together with its temporal profile.

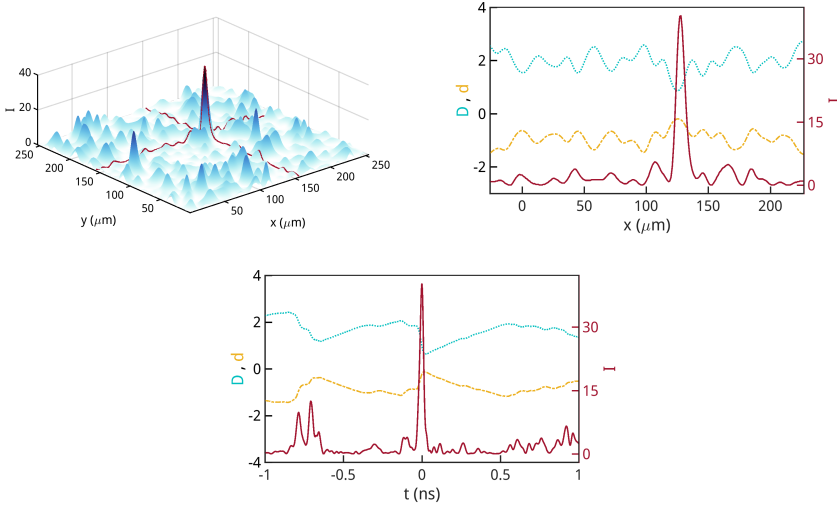


**Fig. 5** Example of a rogue wave in the transverse plane (upper left panel) and its spatial (upper right panel) and temporal (lower panel) profiles, shown for the variables  $I$  (solid red line),  $D$  (dotted blue line) and  $d$  (dash dotted yellow line). Parameters are  $\mu = 4.8, r = 2.2$ .

## 4 Conclusion

Based on our expertise, both in optical systems and the computation of rare and extreme events, we would like to analyze spatially extended optical cavities in various regimes. In particular, genetic algorithms similar to the one used for studying atmospheric jet phase transitions, could potentially give very large-ensemble statistics of optical rogue waves. One of the key points is to compare these results with known experiments taking place in our laboratory and in various places over the world (New Zealand, Scotland, and France). This study will provide a rigorous formalism for optical rogue waves and will also give tools for predicting their appearance and in particular to detect instanton-driven regimes. This approach based on non-equilibrium statistical physics is completely new and could be extended to many area of physics due to its predictive character.

## References

1. H.Kahn and T.Harris, Estimation of particle transmission by random sampling, *Natl. Bur. Stand., Appl. Math. Ser.*,12,27–30 (1951).
2. Pierre Del Moral, Feynman-Kac formulae, Genealogical and interacting particle systems with applications, *Probability and Applications*, New York, Springer-Verlag, (2004).
3. F.Cérou and A.Guyader, Adaptive Multilevel Splitting for Rare Events Analysis,*Stoch. Anal. and Appl.*,25,417–443 (2007).
4. E.Simonnet, Combinatorial analysis of the adaptive last particle method, *Stat.Comput.*, in press 2014, DOI 10.1007/s11222-014-9489-6 (access online).
5. J.Rolland and E.Simonnet, 2015. Statistical behavior of adaptive multilevel algorithm in simple models, *J.Comp.Phys.*, **283**, 541–558.
6. J.Rolland, F.Bouchet, E.Simonnet, Computing transition rates for the 1-D stochastic Ginzburg–Landau–Allen–Cahn equation for finite-amplitude noise with a rare event algorithm, *J.Stat.Phys.*, (2016), **162**, 277–311.
7. F.Ragone, J.Wouters, and F.Bouchet, Computation of extreme heat waves in climate models using a large deviation algorithm , *PNAS*, 2017.
8. PS.Markus, Prediction of a global climate change on Jupiter. *Nature*, 22:428,828–831 (2004).
9. D.R. Solli, C. Ropers, P. Koonath, and B. Jalali, Optical rogue waves, *Nature* **450**, pp 1054-1057, 2007.
10. M. Onorato, S. Residori, U. Bortolozzo, A. Montina, and F.T. Arecchi, Rogue waves and their generating mechanisms in different physical contexts, *Physics Reports* **528**, pp 47–89 (2013).
11. J. M. Dudley, F. Dias, P. Koonath, M. Erkintalo, and G. Genty, Instabilities, breathers and rogue waves in optics, *Nat. Photon.* **8**, pp 755–764, 2014.
12. N. Akhmediev, B. Kibler, F. Baronio, M. Belić, W.P. Zhong, Y. Zhang, W. Chang, J.M. Soto-Crespo, P. Vouzas, P. Grelu, etc., Roadmap on optical rogue waves and extreme events, *Journal of Optics* **18**, 063001, 2016.
13. C. Bonatto, M. Feyereisen, S. Barland, M. Giudici, C. Masoller, J. R. Rios Leite, and J. R. Tredicce, Deterministic Optical Rogue Waves, *Phys. Rev. Lett.* **107**, 053901, 2011.
14. F. Selmi, S. Coulibaly, Z. Lohmari, I. Sagnes, G. Beaudoin, M.G. Clerc, and S. Barbay, Spatiotemporal chaos induces extreme events in an extended microcavity laser, *Phys. Rev. Lett.* **116**, 013901–5, 2016.
15. C. Rimoldi, S. Barland, F. Prati, and G. Tissoni, Spatiotemporal extreme events in a laser with a saturable absorber, *Phys. Rev. A* **95**, 023841–8, 2017.
16. C. Gibson, A. M. Yao, and G. L. Oppo, Optical Rogue Waves in Vortex Turbulence, *Phys. Rev. Lett.* **116**, 043903–5, 2016
17. F.T. Arecchi, U. Bortolozzo, A. Montina, and S. Residori, Granularity and Inhomogeneity Are the Joint Generators of Optical Rogue Waves, *Phys. Rev. Lett.* **106**, 153901-4, 2011.

# Complex molecule synthesis made easy

Nelli Elizarov, Pascal D. Giorgi,  
Alexandra Yeromina, Sylvain Antoniotti

**Abstract** By the combination of suitable catalytic methodologies, the synthesis of complex molecules could be performed with limited footprints and energy consumption either in orthogonal mult catalysis, sequential one-pot reactions or sequential reactions in continuous flow. In this account, we present a selection of our recent results in this area of research where several catalysts such as supported metal nanoparticles, supported metal salts, or mineral and organic bases were combined. New and step-economical synthetic methods were thus developed either in standard batch reactors or in continuous flow using millifluidic technology.

## 1 Introduction

For most epistemologists and historians of science, organic synthesis was born serendipitously in 1828 when Friedrich Wöhler obtained urea from ammonium cyanide [1]. Since then, the art of synthesis has improved both in terms of the complexity of molecules synthesized and the efficiency of the synthetic methods used. In most instances, the chemical synthesis of a given molecule starts with commercially available building blocks, mostly from the petrochemical industry, but increasingly from bio-based resources [2]. The core structure of the building block is then modified following a series of sequential operations to increase the number of atoms, the number of covalent bonds and the degree of oxidation, like Nature does for example

---

Sylvain Antoniotti  
Université Côte d'Azur, CNRS, Institut de Chimie de Nice. e-mail: [sylvain.  
antoniotti@unice.fr](mailto:sylvain.antoniotti@unice.fr)

in the biosynthesis of complex terpenoids [3]. For larger molecules, two or more syntheses can be performed in parallel and their products merged at some point to converge towards the final structure [4]. In the light of the recent shift towards more sustainable processes in chemical synthesis, it has become desirable to discover and apply novel methodologies to fulfill the need for complex molecules to be used in health or well-being applications without compromising the quality of the environment and the level of resources left to future generations [5].

To contribute to this effort, we have recently developed complex catalytic systems simply hyphenated in the same reactor or synergistically assembled to perform multiple elementary steps of synthesis in one operation, thereby delivering complex molecules more easily. Catalysis is in itself a premium approach to discover chemical transformations with low impact in terms of waste generation and energy consumption by its intrinsic assets [6–8]. Specifically, our strategy is based on the design of complex reactions schemes triggered by a clean oxidation reaction of activated alcohols by gold nanoparticles (Au NPs) solely requiring O<sub>2</sub> as the terminal oxidant [9]. To achieve these one-pot/multi-step transformations, we needed an oxidizing system both specific of the allylic alcohol motif, and selective for the formation of aldehydes. In addition, this ideal oxidative catalytic system had to be compatible with the multicatalytic setting. These prerequisites were found with Au NPs operating under O<sub>2</sub> [10–14].

In this account, we present our recent results in this area of research where the Au NPs-catalyzed allylic alcohol oxidation has been combined with C-C bond forming tandem reactions such as Friedel-Crafts-type aldolisation/cyclisation and oxa-Michael addition/aldolisation to yield valuable bioactive molecules in one operation, making complex molecules synthesis easy.

## 2 Oxidation by supported gold nanoparticles

Gold nanoparticles (Au NPs) have been successfully used in various catalytic carbon-carbon and carbon-heteroatom bond-forming reactions and, thanks to their ability to activate molecular oxygen, in oxidation reactions of organic substrates [15–20].

Preliminary screening of catalysts and reaction conditions taught us that small supported Au NPs (2–3 nm of diameter) were suitable as a catalyst in toluene and THF for the oxidation of activated alcohols. Optimization studies and control experiments were thus performed with these catalysts in batch reactors on benzyl alcohol **1a**, a benchmark substrate for this type of

oxidation reaction [21]. To avoid both energy consumption and safety issues, a fixed pressure of O<sub>2</sub> of 1 atm was used.

These conditions were successfully applied to allylic alcohols such as cinnamyl alcohol **2a**, nerol **3a**, geraniol **4a**, and farnesol **5a** delivering the corresponding aldehydes in 66-99% yields and 66-99% conversion (Figure 1). With these results in hand, we started to study the reaction in continuous flow. Heterogeneous catalysis is well suited for being used in flow since catalytic reactors as simple as a column filled with the solid catalytic material could be used. In the case of reactions occurring in gas-liquid biphasic medium, the flow chemistry set up often outperforms batch reactors [22,23]. We therefore transposed our batch conditions with fixed-bed catalytic reactors containing Au NPs supported on Al<sub>2</sub>O<sub>3</sub> and a tube-in-tube gas/liquid device for the O<sub>2</sub> supply. The optimized protocol in continuous flow was found to be more efficient for aliphatic substrates, the corresponding aldehydes **1-5b** being obtained in 84-87% yield (vs 66-68% in batch) at a flow rate of 0.444 mL.min<sup>-1</sup> for a residence time of 3.7 minutes. A better relative O<sub>2</sub> concentration could probably account for this improvement, as well as the limited residence time of the product in the reactor, thereby limiting the risk of degradation at 80°C [21].



**Fig. 1** Au NPs-catalyzed oxidation of activated alcohols.

### 3 Oxidation / Friedel-Crafts Aldolisation / Cyclisation

With this oxidation protocol tailored for our applications in hand, we next turned our attention to its combination with an aldol Friedel-Crafts-type reaction, requiring an aldehyde as the electrophilic partner and aryl nucleophiles.

Our study was initiated with benzyl alcohol derivatives and an electron-rich aryl nucleophile, such as veratrol **6**, in order to obtain unsymmetri-

cal benzophenones upon oxidation/aldol Friedel-Crafts-type/oxidation. To achieve this goal, we combined the Au NPs-catalyzed oxidation with a Bronsted acid-catalyzed reaction with the use of Amberlyst 15, a sulfonic organic resin. In spite of several attempts, we found that if the first and second steps occurred as expected with the oxidation of **1a** to **1b** and subsequent addition of **6**, the second oxidation to the corresponding benzophenone did not occur and the addition of a second veratrol unit yielded triarylmethanes such as **1a6** together with oxidation products benzoic acid **1c** and benzyl benzoate **1d** and other secondary products (Figure 2).

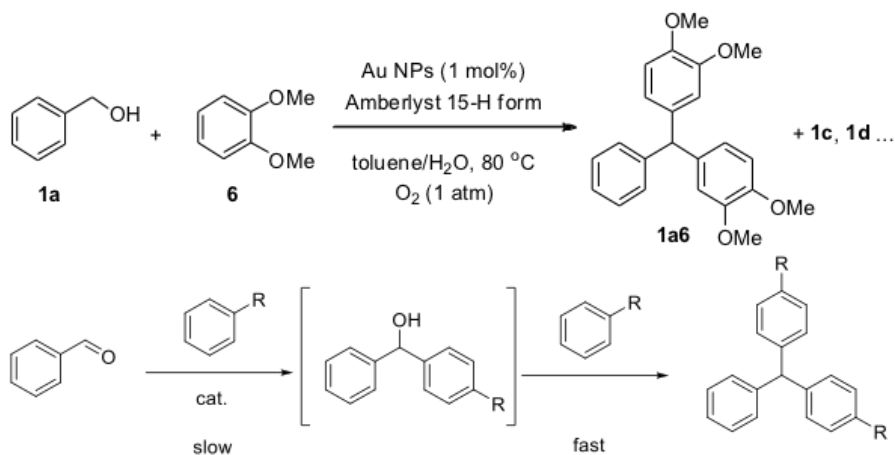


Fig. 2 Combined oxidation/aldol Friedel-Crafts type reaction.

Considering the reactivity of aldol Friedel-Crafts products, we decided to turn this reactivity to our favor using bifunctional substrates and aryl nucleophiles likely to react intramolecularly in a second time to yield complex cyclic structures. The aldehydic substrate would be generated in situ upon Au NPs-catalyzed oxidation of allylic alcohols under O<sub>2</sub>.

We thus screened a series of Lewis and Bronsted acids in a test reaction with citral (mixture of **3b** and **4b**) and 5-methylresorcinol (orcinol) **7**, thereby focusing on the second step. If conventional Lewis acids delivered mixtures containing  $\Delta$ 9- and  $\Delta$ 8-tetrahydrocannabinol (THCC) **3aa**, the use of montmorillonite doped with metal cations (M-MMT) enabled the selective formation of *ortho*-THCC **3aa'**. Under optimized conditions using Ti-MMT as catalyst (10 mol%), a yield of up to 98% **3aa'** was obtained as a 83:17 mixture of  $\Delta$ 9 and  $\Delta$ 8 isomers (entry 13). The *cis/trans* ratio was found to be 8:2 in most cases. This result was rather unexpected since these compounds were

typically observed as side products in various syntheses of natural cannabinoids. In the same reaction conditions, but using olivetol **8** instead of **7**, *ortho*- $\Delta^9$ -THC **3ab'** was obtained in 77% isolated yield (Figure 3) [24].

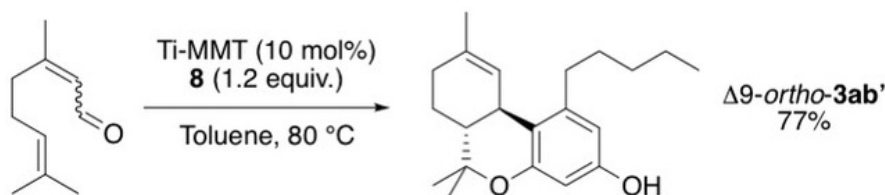
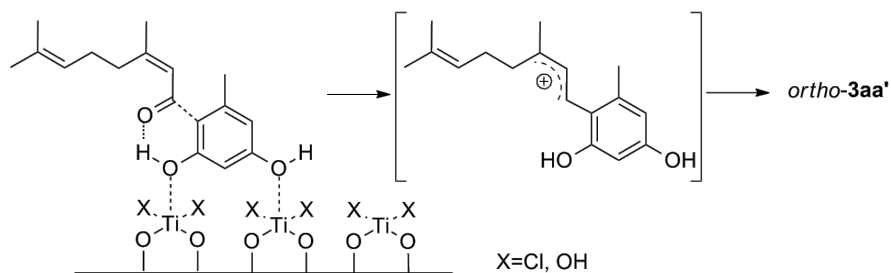


Fig. 3 Formation of the *ortho*- $\Delta^9$ -THC **3ab'**.

A series of experiments was then undertaken to gain a better understanding of the regioselectivity of the reaction. First, the role of hydroxyl groups of **7** was evaluated. Citral was thus treated with modified alkyl resorcinols, in the presence of Ti-MMT (10 mol%) under our optimized conditions. Interestingly, the blockage of both hydroxyl groups by methylation or acetylation resulted in complete inhibition of the arylation reaction and the recovery of unchanged citral. Surprisingly, the blockage of a single hydroxyl group also completely inhibited the reaction. Based on these observations, and taking the regioselectivity in favor of *ortho*-isomers into consideration, we reasoned that Ti-MMT could influence the selectivity through a template effect where both hydroxyl groups would coordinate the interlamellar surface, combined with a Lewis-acid assisted Bronsted acid process (LBA process) allowed by Ti(IV) species. The nucleophilic attack of the arene would thus proceed via the most accessible position, in *ortho* relative to the alkyl substituent (Figure 4).

Considering our interest in the design of multicatalytic chemical processes, we performed a preliminary series of tests to combine an Au NP-catalyzed oxidation of allylic alcohols with the Ti-MMT-catalyzed cyclisation. Unfortunately, catalysts were not compatible in our conditions and the oxidation step was quenched in the presence of Ti-MMT. We thus moved towards continuous flow chemistry reactors.

The first stage of the batch/flow transposition was the optimization of the Ti-MMT-catalyzed step. At a 0.05 M concentration, a conversion of 100% of citral and 98% yield of cyclized products could be obtained with a column charged with 400 mg of Ti-MMT within 5 min residence time. With the implementation of a second catalytic column filled with Au NPs/ $\text{Al}_2\text{O}_3$  (1 g) and using the tube-in-tube technology for an efficient  $\text{O}_2$  supply, the flow synthesis of *ortho*-THC and analogs was possible from **3a** (2.5 mmol scale) and enabled total conversion, and the formation of *ortho*-THCC **3aa'** ( $\Delta^8/\Delta^9$



**Fig. 4** LBA mode of activation at the Ti-MMT surface and subsequent regioselectivity of the reaction.

1:3.5) and *ortho*-THC **3ab'** ( $\Delta 8/\Delta 9$  1:6) with a 81 and 72% yield, respectively, from **7** and **8** (Figure 5). The first stage of the batch/flow transposition was the optimization of the Ti-MMT-catalyzed step. At a 0.05 M concentration, a conversion of 100% of citral and 98% yield of cyclized products could be obtained with a column charged with 400 mg of Ti-MMT within 5 min residence time. With the implementation of a second catalytic column filled with Au NPs/ $\text{Al}_2\text{O}_3$  (1 g) and using the tube-in-tube technology for an efficient  $\text{O}_2$  supply, the flow synthesis of *ortho*-THC and analogs was possible from **3a** (2.5 mmol scale) and enabled total conversion, and the formation of *ortho*-THCC **3aa'** ( $\Delta 8/\Delta 9$  1:3.5) and *ortho*-THC **3ab'** ( $\Delta 8/\Delta 9$  1:6) with a 81 and 72% yield, respectively, from **7** and **8** (Figure 5).

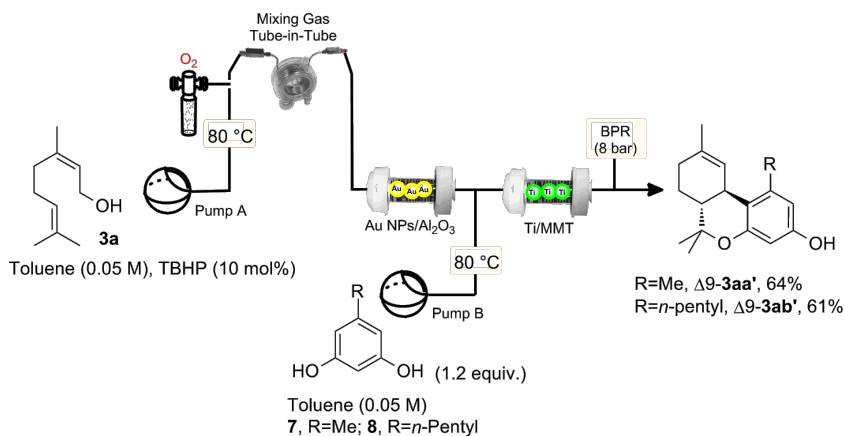


**Fig. 5** Continuous flow set up for the synthesis of *ortho*-THCs **3aa'**-**3ab'**.

## 4 Oxidation / Hetero-Michael Addition / Addition / Crotonisation

Chromenes are motifs occurring in a large number of natural products exhibiting bioactivity and several synthetic methods to access these structures have been reported [25–33]. Our plan was to use the Au NPs/O<sub>2</sub> catalytic system to generate in situ  $\alpha,\beta$ -unsaturated aldehydes further undergoing a base-catalyzed oxa-Michael addition of salicylaldehydes to yield chromenes substituted on positions 2, 3 and 5 in a bicatalytic one-pot/4-steps procedure thereby shortening the access to these chromene structures. Initial testing taught us that the two catalytic systems were not compatible, and a sequential one-pot process was thus developed.

Upon substrate-specific optimisation, we found that for aliphatic allylic alcohols, a mineral base such as K<sub>2</sub>CO<sub>3</sub> (1.1 equiv., added as a methanolic solution) was efficient enough and chromenes were obtained in 59–67% yields. With cinnamyl alcohol derivatives, the use of an organic base such as pyrrolidine (30 mol%) in THF in the presence of molecular sieves (3 Å) was necessary for the reaction to proceed efficiently, and the expected chromenes were obtained in 86–93% yields. By replacing salicylaldehyde **9** (R<sub>3</sub>=H, X=O) by *ortho*-aminobenzaldehyde **10** (R<sub>3</sub>=H, X=NH), dihydroquinolines could be obtained similarly in 79–93% yields. Variation on the salicylaldehyde partner was also possible (Figure 6) [34].

In summary, we have developed a step- and atom-economical bicatalytic tandem process allowing a simplified access to biologically relevant chromene and 1,2-dihydroquinoline scaffolds with a large space of substitution possibilities. We have shown that up to five reactions could proceed in the same pot to convert simple starting materials into complex molecules by combining nanocatalysis and base-catalysis.

## 5 Conclusion

It is possible to perform intensive synthesis by adapting existing protocols or discovering new ones. To achieve these goals, the use of catalysis is the key to success for both basic and practical reasons. Combined with flow chemistry technology, complex molecule synthesis could be achieved easily and efficiently. These approaches could be further developed in the future toward an ideal goal of one-pot total synthesis.

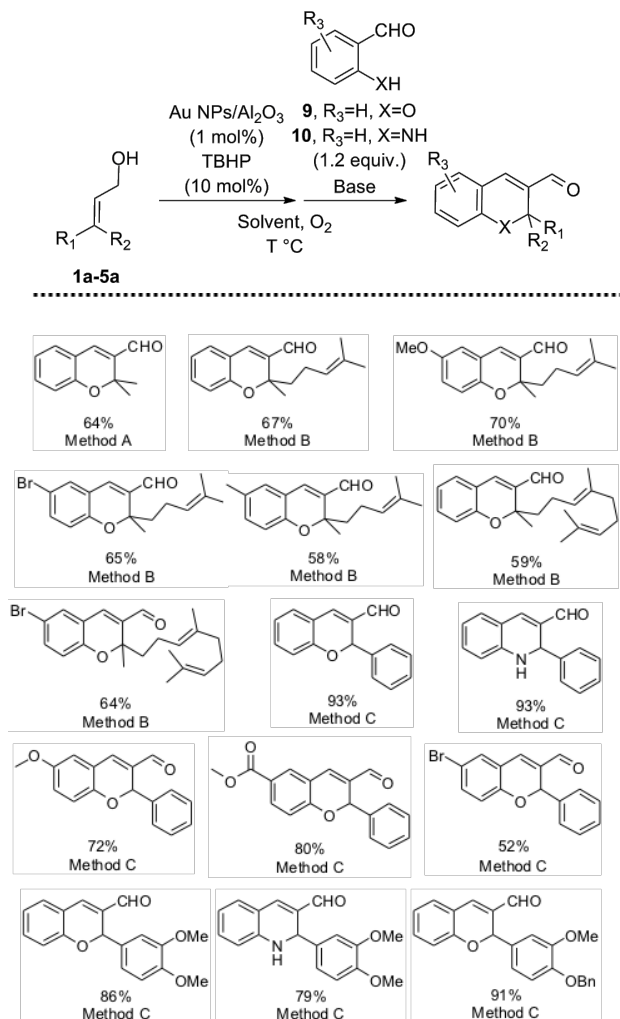


**Fig. 6** Bicatalytic one-pot/4-steps synthesis of substituted chromenes/dihydroquinolines (Method A: triazabicyclodecene (TBD), Method B: K<sub>2</sub>CO<sub>3</sub> Method C: pyrrolidine).

## References

1. Friedrich Wöhler. Ueber künstliche bildung des harnstoffs. *Annalen der Physik*, 88(2):253–256, 1828.
2. Sylvain Antoniotti. *Chimie verte - Chimie durable*, page 192. Ellipses, Paris, 2013.
3. Thomas J Maimone and Phil S Baran. Modern synthetic efforts toward biologically active terpenes. *Nature chemical biology*, 3(7):396–407, 2007.

4. Kyriacos Costa Nicolaou and Tamsyn Montagnon. *Molecules that changed the world.*, page 385. Wiley-VCH Verlag GmbH, Weinheim, 2008.
5. Chao-Jun Li and Paul T Anastas. Green chemistry: present and future. *Chemical Society Reviews*, 41(4):1413–1414, 2012.
6. Avelino Corma and Hermenegildo Garcia. Lewis acids: from conventional homogeneous to green homogeneous and heterogeneous catalysis. *Chemical Reviews*, 103(11):4307–4366, 2003.
7. Roger A Sheldon. E factors, green chemistry and catalysis: an odyssey. *Chemical Communications*, (29):3352–3365, 2008.
8. Meenakshisundaram Sankar, Nikolaos Dimitratos, Peter J Miedziak, Peter P Wells, Christopher J Kiely, and Graham J Hutchings. Designing bimetallic catalysts for a green and sustainable future. *Chemical Society Reviews*, 41(24):8099–8139, 2012.
9. Pascal Giorgi and Sylvain Antoniotti. Catalytic tandem reactions triggered by the introduction of a carbonyl function. In Atta ur Rahman, editor, *Advances in Organic Synthesis*, pages 1–31. Bentham Science Publishers, 2017.
10. Sudhir E Dapurkar, Zameer Shervani, Toshiro Yokoyama, Yutaka Ikushima, and Hajime Kawanami. Supported gold nanoparticles catalysts for solvent-free selective oxidation of benzylic compounds into ketones at 1 atm o<sub>2</sub>. *Catalysis letters*, 130(1-2):42–47, 2009.
11. Antonio Buonerba, Cinzia Cuomo, Sheila Ortega Sánchez, Patrizia Canton, and Alfonso Grassi. Gold nanoparticles incarcerated in nanoporous syndiotactic polystyrene matrices as new and efficient catalysts for alcohol oxidations. *Chemistry-A European Journal*, 18(2):709–715, 2012.
12. Takashi Takei, Tomoki Akita, Isao Nakamura, Tadahiro Fujitani, Mitsutaka Okumura, Kazuyuki Okazaki, Jiahui Huang, Tamao Ishida, and Masatake Haruta. *Advances in Catalysis*, pages 1–126. Elsevier Academic Press Inc, San Diego, 2012.
13. Emmanuel Skupien, Rob J Berger, Vera P Santos, Jorge Gascon, Michiel Makkee, Michiel T Kreutzer, Patricia J Kooyman, Jacob A Moulijn, and Freek Kapteijn. Inhibition of a gold-based catalyst in benzyl alcohol oxidation: Understanding and remediation. *Catalysts*, 4(2):89–115, 2014.
14. Hiroyuki Miyamura, Ryosuke Matsubara, Yoji Miyazaki, and Shū Kobayashi. Aerobic oxidation of alcohols at room temperature and atmospheric conditions catalyzed by reusable gold nanoclusters stabilized by the benzene rings of polystyrene derivatives. *Angewandte Chemie*, 119(22):4229–4232, 2007.
15. Didier Astruc. *Nanoparticles and catalysis*. John Wiley & Sons, 2008.
16. Younan Xia, Hong Yang, and Charles T. Campbell. Nanoparticles for catalysis. *Accounts of Chemical Research*, 46(8):1671–1672, 2013.
17. Manolis Stratakis and Hermenegildo Garcia. Catalysis by supported gold nanoparticles: beyond aerobic oxidative processes. *Chemical Reviews*, 112(8):4469–4506, 2012.
18. Philippe Serp and Karine Philippot, editors. *Nanomaterials in Catalysis*. Wiley-VCH: Weinheim, Germany, 2013.
19. Serena Biella and Michele Rossi. Gas phase oxidation of alcohols to aldehydes or ketones catalysed by supported gold. *Chemical communications*, (3):378–379, 2003.
20. Cristina Della Pina, Ermelinda Falletta, Laura Prati, and Michele Rossi. Selective oxidation using gold. *Chemical Society Reviews*, 37(9):2077–2095, 2008.
21. Pascal D Giorgi, Nelli Elizarov, and Sylvain Antoniotti. Selective oxidation of activated alcohols by supported gold nanoparticles under an atmospheric pressure of o<sub>2</sub>: Batch and continuous-flow studies. *ChemCatChem*, 9(10):1830–1836, 2017.
22. Naiwei Wang, Tsutomu Matsumoto, Masaharu Ueno, Hiroyuki Miyamura, and Shū Kobayashi. A gold-immobilized microchannel flow reactor for oxidation of alcohols with molecular oxygen. *Angewandte Chemie*, 121(26):4838–4840, 2009.

23. Sangeeta Roy Chaudhuri, Jan Hartwig, Lukas Kupracz, Torben Kodanek, Jens Wegner, and Andreas Kirschning. Oxidations of allylic and benzylic alcohols under inductively-heated flow conditions with gold-doped superparamagnetic nanostructured particles as catalyst and oxygen as oxidant. *Advanced Synthesis & Catalysis*, 356(17):3530–3538, 2014.
24. Pascal Giorgi, Virginie Liautard, Mathieu Pucheault, and Sylvain Antoniotti. *Eur. J. Org. Chem.*, 11:1307–1311, 2018.
25. Naoki Iwata, Naili Wang, Xinsheng Yao, and Susumu Kitanaka. Structures and histamine release inhibitory effects of prenylated orcinol derivatives from rhododendron dauricum. *Journal of natural products*, 67(7):1106–1109, 2004.
26. Marialuisa Menna, Anna Aiello, Filomena D’Aniello, Concetta Imperatore, Paolo Luciano, Rocco Vitalone, Carlo Irace, and Rita Santamaria. Conithiaquinones a and b, tetracyclic cytotoxic meroterpenes from the mediterranean ascidian aplidium conicum. *European Journal of Organic Chemistry*, 2013(16):3241–3246, 2013.
27. Yoshihiro Noda and Misato Yasuda. Enantioselective synthesis of (-)-(r)-cordiachromene and (-)-(r)-dictyochromenol utilizing intramolecular snar reaction. *Helvetica Chimica Acta*, 95(10):1946–1952, 2012.
28. Dipak Harel, Sami A Khalid, Marcel Kaiser, Reto Brun, Bernhard Wünsch, and Thomas J Schmidt. Enecalol angelate, an unstable chromene from *ageratum conyzoides* L.: total synthesis and investigation of its antiprotozoal activity. *Journal of ethnopharmacology*, 137(1):620–625, 2011.
29. Maryla Szczepanik, Robert Obara, Antoni Szumny, Beata Gabryś, Aleksandra Halarewicz-Pacan, Jan Nawrot, and Czesław Wawrzęczyk. Synthesis and insect antifeedant activity of precocene derivatives with lactone moiety. *Journal of agricultural and food chemistry*, 53(15):5905–5910, 2005.
30. Manuel C Broehmer, Nicole Volz, and Stefan Braese. Thieme chemistry journal awardees—where are they now? microwave-assisted rhodium-catalyzed decarbonylation of functionalized 3-formyl-2h-chromenes: A sequence for functionalized chromenes like deoxycordiachromene. *Synlett*, 2009(09):1383–1386, 2009.
31. Kegang Liu and Xiaohua Jiang. Regioselective and enantioselective domino aldol-oxa-michael reactions to construct quaternary (chroman) stereocenters. *European Journal of Organic Chemistry*, 2015(29):6423–6428, 2015.
32. Henrik Sunden, Ismail Ibrahim, Gui-Ling Zhao, Lars Eriksson, and Armando Cordova. Catalytic enantioselective domino oxa-michael/aldol condensations: Asymmetric synthesis of benzopyran derivatives. *Chemistry—A European Journal*, 13(2):574–581, 2007.
33. Xiang-Wei Du and Levi M Stanley. Tandem alkyne hydroacylation and oxo-michael addition: Diastereoselective synthesis of 2, 3-disubstituted chroman-4-ones and fluorinated derivatives. *Organic letters*, 17(13):3276–3279, 2015.
34. Pascal D Giorgi, Peter J Miedziak, Jennifer K Edwards, Graham J Hutchings, and Sylvain Antoniotti. Bicataltic multistep reactions en route to the one-pot total synthesis of complex molecules: Easy access to chromene and 1, 2-dihydroquinoline derivatives from simple substrates. *ChemCatChem*, 9(1):70–75, 2017.

# Chaotic reverberation chambers for electromagnetic compatibility

Olivier Legrand, Ulrich Kuhl, Fabrice Mortessagne,  
Khalid Oubaha and Martin Richter

**Abstract** Electromagnetic reverberation chambers are now commonly used in the domain of ElectroMagnetic Compatibility (EMC) where electronic devices or wirelessly connected objects are, for instance, submitted to immunity tests. By modifying the standard geometry of current reverberation chambers – which are metallic Faraday cavities – to make them chaotic, we have shown that the statistical requirements of a well-operating reverberation chamber are better satisfied in the more complex geometry due to its spatial and spectral statistical behaviors being very close to those predicted by random matrix theory. More specifically, we have shown that in the range of frequency corresponding to the first few hundred modes, the suppression of non-generic modes could be achieved by drastically reducing the amount of parallel walls. Among other results we could demonstrate that, in a chaotic cavity, the low frequency limit of a well operating reverberation chamber can be significantly reduced under the usual values met in conventional mode-stirred reverberation chambers.

## 1 Introduction

Mode-stirred reverberation chambers (MSRC) play an important role in Electromagnetic Compatibility (EMC). They have been designed initially to cope with the measurements of the electromagnetic (EM) emission of ra-

---

Olivier Legrand  
Institute of Physics of Nice, Université Côte d'Azur, Nice, France, e-mail: [olivier.legrand@unice.fr](mailto:olivier.legrand@unice.fr)

diofrequency sources. By extending the concerned frequencies from hundreds of MHz to tens of GHz, the reduction of the wavelength came with a decrease of the antenna size, so that the production of intense fields obtained through the confinement in the reverberant environment had to be favored. By producing oversized cavities compared to the wavelength, generation of fields of random amplitudes is currently achieved by mode-stirring [1] with the help of complex-shaped metallic mechanical rotating stirrers. With their help it is possible to obtain statistically valuable results for the EM radiation emitted from or impinging upon an object under test. In particular, thanks to the presence of a mechanical stirrer, devices under test are expected to be submitted to an isotropic, statistically uniform and depolarized electromagnetic field. Those properties are believed to be satisfied under the condition that the frequency is above the so-called *lowest useable frequency* (LUF). There are many definitions of the LUF [2,3] but they all suffer from an important drawback since they don't explicitly take the overlap of resonances, induced by the losses, into account [4]. Indeed, the LUF being the frequency above which the condition of a statistical uniformity of the field is achieved, the use of a stirrer is supposed to ensure the validity of the so-called *continuous plane wave-spectrum* hypothesis. This statistical hypothesis about the EM field inside reverberation chambers is commonly used by the EMC community and was originally proposed by D. A. Hill [5,6], who assumed that the field is statistically equivalent to a random superposition of traveling plane waves. This hypothesis is generally well verified if the excitation frequency is much larger than the LUF, a result that has long been acknowledged in room acoustics literature [7,8] due to large modal overlap. However, in a frequency regime close to the LUF, the EM field might be neither uniform nor isotropic and this is in spite of any stirring. In this regime, conventional reverberation chambers, which are not chaotic cavities, display a highly non-universal behavior, which may depend on their geometries, the types of antennas used or the object under test.

Moreover, in order to get reliable statements about the fluctuations of the EM field, it is necessary to use statistically independent experimental realizations. Therefore, the statistical ensemble usually achieved by a mode-stirrer has to be mixing enough to make the intensity patterns of the MSRC statistically independent from each other.

All the previously mentioned statistical requirements of a well-stirred MSRC above the LUF closely correspond to the natural behavior of a chaotic cavity [9–11]. For more than five years now, our group has been investigating the spectral and spatial statistical properties of three-dimensional (3D) chaotic cavities, in collaboration with Elodie Richalot and colleagues from ESYCOM at UPEMLV, and has proposed to use chaotic reverberation chambers (CRC) as a new paradigm for applications in EMC [12–14].

Beyond EMC concerns, MSRCs also allow one to simulate complex propagation environments related to multiple reflections, a particularly interesting feature for applications towards modern telecommunication techniques. In particular, CRCs have been recently shown to provide well-adapted benchmarks to test the quality of communication between antennas when the influence of reverberation cannot be neglected [15].

In the following section, we will briefly review the main statistical features of the electromagnetic response of a CRC that can be deduced from a Random Matrix model introduced in [14, 16]

## 2 Statistics of the response in a chaotic reverberation chamber

When Hill’s hypothesis is not valid, below or in the vicinity of the LUF, the real and imaginary parts of each component of the EM field are not identically distributed [17]. For a given configuration of an ideally chaotic cavity, they are still independently Gaussian distributed, but with different variances. The ensuing distribution of the modulus of each component  $|E_a|$  is then no longer a Rayleigh distribution but depends on a single parameter  $\varrho$ , called the *phase rigidity*, defined by:

$$\varrho = \frac{\int_V \mathbf{E} \cdot \mathbf{E} d\mathbf{r}}{\int_V \|\mathbf{E}\|^2 d\mathbf{r}}. \tag{1}$$

Note that for  $|\varrho| \rightarrow 1$  the system tends to be lossless, a situation corresponding to non-overlapping resonances at low frequency well under the LUF, whereas  $|\varrho| \rightarrow 0$  corresponds to a completely open system, which recovers the limit of validity of Hill’s assumptions for frequencies much larger than the LUF. More specifically, due to the *ergodicity* of the modes that contribute to the response, for a given excitation frequency and a given configuration, the probability distribution  $P(\mathcal{E}_a; \varrho)$  of the normalized field amplitude of the Cartesian component  $\mathcal{E}_a = |E_a| / \langle |E_a|^2 \rangle_r^{1/2}$  depends solely on the modulus of  $\varrho$ . Since the *phase rigidity* is itself a distributed quantity, the distribution of the normalized field amplitude for an ensemble of responses resulting from stirring thus reads

$$P_a(\mathcal{E}_a) = \int_0^1 P_\varrho(\varrho) P(\mathcal{E}_a; \varrho) d\varrho \tag{2}$$

where  $P_\varrho$  is the distribution of the *phase rigidity* of the responses. Our investigations, based on numerical simulations of the Random Matrix model described in [14, 17], have shown that  $P_\varrho$  depends solely on the mean modal

overlap  $d$ . This overlap  $d$  is defined as the ratio of the average modal bandwidth to the average difference between neighboring modal frequencies. We assume that within the investigated frequency range, the latter quantities vary only slightly. Similar results have also been obtained for the phase of the response in a CRC [18].

These theoretical results as well as spectral statistical features like the so-called *level repulsion* between frequencies of the modes, the distribution of the widths of the resonances [19], or the distribution of the width shifts obtained through parametrical variation of the CRC [20] have been tested experimentally and confronted with measurements that are meaningful for the statistical requirements (for instance the *uniformity criterion*) [16], which should be met in well-operating MSRCs according to the IEC standard [3].



**Fig. 1** 180-degree photograph of the chaotic RC at ESYCOM. The commercial RC consists in a rectangular metallic cavity of dimensions  $W = 2.95$  m,  $L = 2.75$  m and  $H = 2.35$  m and was modified by placing 3 hemispheres with radii of 40 cm (one at the ceiling and two on adjacent walls). The mechanical stirrer in the far corner can be seen.

One of the RCs we investigated is shown in Fig. 1 and is located in our partners' lab at ESYCOM. It has a volume  $V \simeq 19$  m<sup>3</sup> and was made chaotic by the addition of three or six metallic half-spheres with a radius of 40 cm located on different walls [13, 16]. The commercial RC we have modified consists of a rectangular metallic cavity of dimensions  $W = 2.95$  m,  $L = 2.75$  m and  $H = 2.35$  m equipped by a mode-stirrer in rotation around the vertical axis and located in a corner. To illustrate the validity of our theoretical approach in an actual CRC, Fig. 2 shows a comparison of the histogram of the normalized field amplitude deduced from experimental data measured in the CRC of Fig. 1, with the prediction (2), where the value  $d = 0.89$  was used. A best fit with a Weibull distribution used in [21] is also shown, demonstrating that the latter cannot account for the experimental data neither in the bulk nor for the small amplitude part of the histogram.

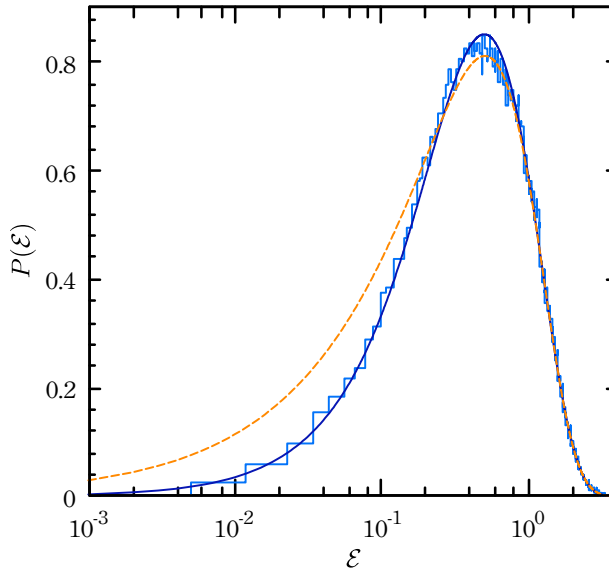


**Fig. 2** Histogram of the normalized field component amplitude from experimental data, compared with the prediction (2) (continuous line) and the corresponding probability distribution of  $P_\varrho(\varrho)$  where the value  $d = 0.89$  was used. Weibull best fit (dashed curve).

Another CRC was specifically designed by our group in INPHYNI for testing communication between monopole antennas in a complex reverberating environment (see Fig. 3) in the framework of experimental investigations concerning the statistics of reflection and transmission in the moderate and strong modal overlap regimes of fully chaotic reverberation chambers [22].

### 3 Conclusion

Here, we have briefly reviewed our theoretical and experimental investigations concerning chaotic electromagnetic cavities leading to the proposal of chaotic reverberation chambers as a new paradigm for applications in EMC, in collaboration with Elodie Richalot from ESYCOM. The results from our group have confirmed the key role of the ergodic character of the response of a chaotic RC to improve the statistical behavior of an RC for frequencies below or in the neighborhood of the LUF. In particular, the statistical criterion proposed in [3] to evaluate the uniformity of the spatial field distri-

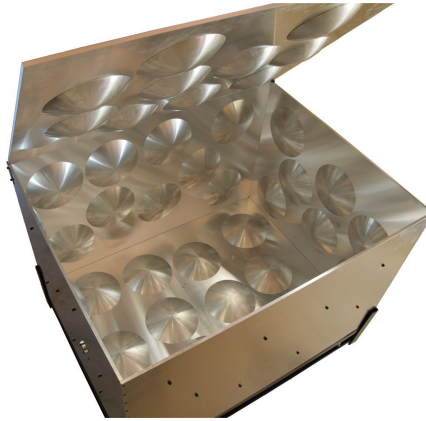


**Fig. 3** Photograph of the chaotic RC at INPHYNI with length  $L=100$  cm, width  $W=77$  cm and height  $H=62$  cm. At the walls 54 spherical caps of radius  $r_c=10$  cm and cap height  $h_c=3$  cm are used. The total internal volume is  $V=0.451$  m<sup>3</sup>.

bution, when used near the LUF or at lower frequencies, is only valid if the RC is chaotic since the universality of the statistics of the response cannot be ensured in the case of a conventional non-chaotic RC.

## Acknowledgment

We thank the European Commission for financial support through the H2020 program by the Open Future Emerging Technology "NEMF21" Project 664828.

## References

1. Corona P., Ladbury J., Latmiral G., "Reverberation chamber research then and now: a review of early work and comparison with current understanding", *IEEE Transactions on Electromagnetic Compatibility*, **44**, no. 1, pp. 87-94, February 2002.
2. Bruns Ch., PhD thesis, "Three-dimensional simulation and experimental verification of a reverberation chamber", University at Fridericiana Karlsruhe (TH), 16041, <http://e-collection.library.ethz.ch/eserv/eth:28055/eth-28055-02.pdf>, 2005.
3. *Electromagnetic Compatibility (EMC) - Part 4-21: Testing and Measurement Techniques - Reverberation Chamber Test Methods*, ser. Blue Book, No. 4, International Electrotechnical Commission (IEC) International Standard IEC 61000-4-21:2011, 2011. [Online]. Available: <https://webstore.iec.ch/publication/4191>

4. A. Cozza, The Role of Losses in the Definition of the Overmoded Condition for Reverberation Chambers and Their Statistics, *IEEE Transactions on Electromagnetic Compatibility* **53** (2), pp. 296–307 (2011).
5. D. Hill, Plane wave integral representation for fields in reverberation chambers, *IEEE Transactions on Electromagnetic Compatibility* **40** (3), pp. 209–217, 1998.
6. D. Hill, *Electromagnetic fields in cavities: deterministic and statistical theories*, IEEE Press Series on Electromagnetic Wave Theory, IEEE ; Wiley, 2009.
7. M. R. Schroeder and K. H. Kuttruff, "On frequency response curves in rooms. Comparison of experimental, theoretical, and monte carlo results for the average frequency spacing between maxima," *J. Acoust. Soc. Am.*, **34**, p. 76 (1962).
8. H. Kuttruff, *Room acoustics*, 5th ed. Spon Press/Taylor & Francis, 2009.
9. M. V. Berry, "Regular and irregular semiclassical wavefunctions," *J. Phys. A*, **10**, p. 2083 (1977).
10. O. Legrand, F. Mortessagne, *Wave Chaos for the Helmholtz Equation, New Directions in Linear Acoustics and Vibration: Quantum Chaos, Random Matrix Theory, and Complexity*, Cambridge University Press, 2010.
11. M. Dennis, *Gaussian Random Wavefields and the Ergodic Mode Hypothesis, New Directions in Linear Acoustics and Vibration: Quantum Chaos, Random Matrix Theory, and Complexity*, Cambridge University Press, 2010.
12. J.-B. Gros, O. Legrand, F. Mortessagne, E. Richalot, and K. Selezmani, "Universal behaviour of a wave chaos based electromagnetic reverberation chamber," *Wave Motion*, **51**, p. 664 (2014).
13. J.-B. Gros, U. Kuhl, O. Legrand, F. Mortessagne, O. Picon, and E. Richalot, "Statistics of the electromagnetic response of a chaotic reverberation chamber," *Adv. Electromagn.*, **4**, p. 38 (2015).
14. J.-B. Gros, U. Kuhl, O. Legrand, and F. Mortessagne, "Lossy chaotic electromagnetic reverberation chambers: Universal statistical behavior of the vectorial field", *Physical Review E*, **93**, 032108 (2016).
15. U. Kuhl, O. Legrand, F. Mortessagne, K. Oubaha, and M. Richter, "Statistics of reflection and transmission in the strong overlap regime of fully chaotic reverberation chambers," in *2017 47th European Microwave Conference (EuMC, Nuremberg)*, 2017, pp. 359–362, see also arXiv:1706.04873, arXiv:1706.04873, accepted paper for the European Microwave Week in Nuremberg 2017. [Online]. Available: <https://arxiv.org/abs/1706.04873>
16. J.-B. Gros, U. Kuhl, O. Legrand, F. Mortessagne, and E. Richalot, "Universal intensity statistics in a chaotic reverberation chamber to refine the criterion of statistical field uniformity", *Metrology for Aerospace (MetroAeroSpace)*, 2015 IEEE, Jun 2015, Benevento, Italy. *IEEE Xplore Metrology for Aerospace*, pp.225-229 (2015).
17. J.-B. Gros, "Statistiques spatiales des cavités chaotiques ouvertes: Applications aux cavités chaotiques électromagnétiques", PhD thesis, 2014, <https://tel.archives-ouvertes.fr/tel-01159009>.
18. J.-B. Gros, U. Kuhl, O. Legrand, F. Mortessagne, and E. Richalot, "Phase distribution of the response in chaotic reverberation chambers", in *Union Radio-Scientifique Internationale (32nd URSI GASS)*, Montreal, 19-26 August 2017.
19. E. Richalot, U. Kuhl, O. Legrand, F. Mortessagne, J. B. Gros, and S. Grivet-Talocia, Experimental characterization of the distribution of resonance widths in chaotic reverberation chambers, in *2016 IEEE Metrology for Aerospace (MetroAeroSpace)* pp. 177-181 (2016).
20. J.-B. Gros, U. Kuhl, O. Legrand, F. Mortessagne, E. Richalot, and D. V. Savin, "Experimental width shift distribution: A test of nonorthogonality for local and global perturbations", *Phys. Rev. Lett.* **113**, 224101 (2014).

21. C. Lemoine, P. Besnier, and M. Drissi, "Proposition of tolerance requirements adapted for the calibration of a reverberation chamber", 20th International Zurich Symposium on EMC, Zurich, pp. 41-44 (2009).
22. D. V. Savin, M. Richter, U. Kuhl, O. Legrand, and F. Mortessagne, "Fluctuations in an established transmission in the presence of a complex environment", *Phys. Rev. E*, **96**, 032221 (2017).

# Collisional relaxation of long range interacting systems of particles

Fernanda P. C. Benetti and Bruno Marcos

**Abstract** Systems of particles with long range interactions present two phases in their evolution: first, the formation of Quasi-Stationary states (such as galaxies) in a process called *violent relaxation* and, second, the much slower relaxation towards thermal equilibrium, in a process called *collisional relaxation*. In this contribution we focus on the last process and we present the first exact calculations of diffusion coefficients performed for non-homogeneous configurations.

## 1 Introduction

In Statistical Physics, we call systems with long range interactions those in which all the particles interact significantly. If they interact through a pair potential, this potential decreases with distance slower than  $u(r \rightarrow \infty) \sim 1/r^d$ , where  $d$  is the dimension of space. There are many such systems in nature: self-gravitating systems such as galaxies, globular clusters or the large scale structure of the Universe, cold trapped atoms, colloids at surface interfaces, active particles, etc. The long range nature of these systems results in the apparition of "exotic" collective effects compared with short range systems. They have different manifestations: formation of Quasi-Stationary

---

Fernanda Benetti

Dipartimento di Fisica, Sapienza Università di Roma Piazzale Aldo Moro, 2 00185 Roma - RM Italy, e-mail: [fernanda.benetti@roma1.infn.it](mailto:fernanda.benetti@roma1.infn.it)

Bruno Marcos

Université Côte d'Azur, CNRS UMR 7351, LJAD, France, e-mail: [marcos@unice.fr](mailto:marcos@unice.fr)

states via the mechanism of “violent relaxation” (such as a galaxy, which is a quasi-stable structure but completely out of thermodynamic equilibrium), “collisional” slow relaxation towards thermodynamic equilibrium in a time scaling with the number of particles, the possibility of negative specific heat at thermodynamic equilibrium, etc. In this contribution we will focus on the process of “collisional” slow relaxation of a long range system towards thermodynamic equilibrium. An example of such a process is the evaporation of stars in a galaxy or a globular cluster. This process is driven by the finiteness of the number of particles, which causes fluctuations (“noise”) in the (mean-field) potential generated by the system. The effect of these fluctuations can be modeled, as it is usually done in Statistical Physics, through a Fokker-Planck or Langevin equation. There are, however, two important difficulties: (i) the noise has to be modeled very precisely taking into account, accurately, the orbit of each particle and (ii) the motion of the particles perturbs, in turn, the mean-field potential giving rise to collective effects. In general this results in very difficult perturbative calculations. We will present the first (to our knowledge) exact calculations of diffusion coefficients for spatially inhomogeneous systems, performed for a simplified one-dimensional long range model, the Hamiltonian Mean Field model (HMF). The material presented in this contribution can be found, in an extended format, in [1].

## 2 Kinetic theory

The natural framework to describe these kinds of out-of-equilibrium systems, composed by a large number of particles  $N$ , is kinetic theory. We start from the discrete distribution function  $f_d(\mathbf{r}, \mathbf{v}, t)$ , which contains all the information of the state of the system at a given time  $t$ ,

$$f_d(\mathbf{r}, \mathbf{v}, t) = m \sum_{i=1}^N \delta[\mathbf{r} - \mathbf{r}_i(t)] \delta[\mathbf{v} - \mathbf{v}_i(t)]. \quad (1)$$

This function has too much information to study the system. Averaging over initial conditions (denoted by the operator  $\langle \dots \rangle$ ) we define the smoothed distribution function  $f(\mathbf{r}, \mathbf{v}, t) = \langle f_d(\mathbf{r}, \mathbf{v}, t) \rangle$ , which is the equivalent of taking the limit  $N \rightarrow \infty$  for a single realization. The fluctuations are defined with  $f_d(\mathbf{r}, \mathbf{v}, t) = f(\mathbf{r}, \mathbf{v}, t) + \delta f(\mathbf{r}, \mathbf{v}, t)$ . It is possible to show that the smoothed distribution function obeys the Vlasov-Boltzmann equation [1]:

$$\frac{\partial f}{\partial t} + \mathbf{v} \cdot \frac{\partial f}{\partial \mathbf{r}} - \frac{\partial \phi}{\partial \mathbf{r}} \cdot \frac{\partial f}{\partial \mathbf{v}} = \frac{\partial}{\partial \mathbf{v}} \cdot \langle \delta f \frac{\partial \delta \phi}{\partial \mathbf{r}} \rangle, \quad (2)$$

The above equation gives the evolution of the smooth distribution due to correlation between its own fluctuations and the fluctuation of the smooth potential  $\phi(\mathbf{r}, t)$ , determined by  $\phi_d(\mathbf{r}, t) = \phi(\mathbf{r}, t) + \delta\phi(\mathbf{r}, t)$ , where

$$\phi(\mathbf{r}, t) = \int u(|\mathbf{r} - \mathbf{r}'|) f(\mathbf{r}', \mathbf{v}', t) d\mathbf{r}' d\mathbf{v}' \quad (3)$$

$$\delta\phi(\mathbf{r}, t) = \int u(|\mathbf{r} - \mathbf{r}'|) \delta f(\mathbf{r}', \mathbf{v}', t) d\mathbf{r}' d\mathbf{v}', \quad (4)$$

where  $u(r)$  is the inter-particle potential.

The strategy to solve Eq. (2) at first order in  $\delta f$  (which is an excellent approximation) consists in linearizing equation (2), to obtain,

$$\frac{\partial \delta f}{\partial t} + \mathbf{v} \cdot \frac{\partial \delta f}{\partial \mathbf{r}} - \frac{\partial \delta \phi}{\partial \mathbf{r}} \cdot \frac{\partial f}{\partial \mathbf{v}} - \frac{\partial \phi}{\partial \mathbf{r}} \cdot \frac{\partial \delta f}{\partial \mathbf{v}} = 0. \quad (5)$$

The evolution of the system can be computed by solving the system of equations (2) and (5).

## 2.1 Homogeneous systems

We will first give a brief derivation of the kinetic equations for the spatially homogeneous case. It is technically simpler than the inhomogeneous one while sharing the same ideas. In this case  $f = f(\mathbf{v}, t)$ , so equations (2) and (5) become

$$\frac{\partial f}{\partial t} = \frac{\partial}{\partial \mathbf{v}} \cdot \langle \delta f \frac{\partial \delta \phi}{\partial \mathbf{r}} \rangle, \quad (6a)$$

$$\frac{\partial \delta f}{\partial t} + \mathbf{v} \cdot \frac{\partial \delta f}{\partial \mathbf{r}} - \frac{\partial \delta \phi}{\partial \mathbf{r}} \cdot \frac{\partial f}{\partial \mathbf{v}} = 0. \quad (6b)$$

In this case it is (relatively) simple to solve Eq. (6b) because  $f$  does not depend on the space variable  $\mathbf{r}$ . Therefore the unperturbed orbits are straight lines with constant velocity. Moreover, applying a Fourier-Laplace transform to the variables  $t$  and  $\mathbf{r}$  does not introduce a convolution in the last term of Eq. (6b).

Defining  $\tilde{\delta f}(\mathbf{k}, \mathbf{v}, \omega) = \frac{1}{(2\pi)^d} \int d\mathbf{r} \int_0^\infty dt e^{-i(\mathbf{k} \cdot \mathbf{r} - \omega t)} \delta f(\mathbf{r}, \mathbf{v}, t)$  and  $\tilde{\delta \phi}(\mathbf{k}, \omega) = \frac{1}{(2\pi)^d} \int d\mathbf{r} \int_0^\infty dt e^{-i(\mathbf{k} \cdot \mathbf{r} - \omega t)} \delta \phi(\mathbf{r}, t)$  and taking the Fourier-Laplace transform of Eq. (6b), we obtain

$$\tilde{\delta f} = \underbrace{\frac{\mathbf{k} \cdot \frac{\partial f}{\partial \mathbf{v}} \tilde{\delta \phi}(\mathbf{k})}{\mathbf{k} \cdot \mathbf{v} - \omega}}_{\text{collective effects}} + \underbrace{\frac{\widehat{\delta f}(\mathbf{k}, \mathbf{v}, 0)}{i(\mathbf{k} \cdot \mathbf{v} - \omega)}}_{\text{initial conditions}}, \quad (7)$$

where  $\widehat{\delta f}(\mathbf{k}, \mathbf{v}, 0) = \int \frac{d\mathbf{r}}{(2\pi)^d} e^{-i\mathbf{k} \cdot \mathbf{r}} \delta f(\mathbf{r}, \mathbf{v}, 0)$  is a Fourier transform. The first term of the r.h.s. of Eq. (7) corresponds to collective effects, which are a generic feature of long range systems. The second term corresponds to the initial fluctuations because of the finiteness of the number of particles  $N$ .

The next step in the derivation consists in expressing the Fourier transform of the fluctuation of the potential  $\widehat{\delta \phi}(\mathbf{k}, \omega)$  as a function of the fluctuation  $\tilde{\delta f}(\mathbf{k}, \omega)$ . To do so, we integrate equation (7) over  $\mathbf{v}$ , and using the Fourier transform of equation (4), we get

$$\int_{-\infty}^{\infty} d\mathbf{v} \tilde{\delta f}(\mathbf{k}, \mathbf{v}, \omega) = \frac{1}{\epsilon(\mathbf{k}, \omega)} \int_{-\infty}^{\infty} d\mathbf{v} \frac{\widehat{\delta f}(\mathbf{k}, \mathbf{v}, 0)}{i(\mathbf{v} \cdot \mathbf{k} - \omega)}, \quad (8)$$

where we have defined the plasma response dielectric function  $\epsilon(\mathbf{k}, \omega) = 1 - \hat{u}(\mathbf{k}) \int d\mathbf{v} \frac{\mathbf{k} \cdot \partial f(\mathbf{v}) / \partial \mathbf{v}}{\mathbf{v} \cdot \mathbf{k} - \omega}$ . Using again equations (4) and (8), we get  $\widehat{\delta \phi}(\mathbf{k}, \omega)$ . After some algebra, we obtain the Lenard-Balescu equation [2]:

$$\begin{aligned} \frac{\partial f}{\partial t} = \pi(2\pi)^d m \sum_{i,j=1}^d \frac{\partial}{\partial v_i} \int d\mathbf{k} d\mathbf{v}' k_i k_j \frac{\hat{u}(\mathbf{k})^2 \delta[\mathbf{k} \cdot (\mathbf{v} - \mathbf{v}')] }{|\epsilon(\mathbf{k}, \mathbf{k} \cdot \mathbf{v})|^2} \\ \times \left( \frac{\partial}{\partial v_j} - \frac{\partial}{\partial v'_j} \right) f(\mathbf{v}, t) f(\mathbf{v}', t). \end{aligned} \quad (9)$$

When collective effects are not taken into account, the first term of the r.h.s. of equation (7) is neglected, which is equivalent to set  $\epsilon(\mathbf{k}, \omega) = 1$ . The Lenard-Balescu equation is called in this case the Landau equation.

## 2.2 Inhomogeneous systems

In inhomogeneous systems, new difficulties appear: (i) the unperturbed orbits are much more complicated than in the homogeneous case and (ii) in the last term of (6b)  $f$  depends also in the position  $\mathbf{r}$ , and taking the Laplace-Fourier transform would give a convolution term. The strategy to solve the difficulty (ii) consists in “homogenizing” the equations, using an appropriate change of variables. These new variables are the angle-action  $(\mathbf{w}, \mathbf{J})$  cor-

responding to the Hamiltonian  $\mathcal{H}$  of smooth dynamics (i.e., the one corresponding to the limit  $N \rightarrow \infty$ ) [3]). Using these variables, particles described by the Hamiltonian  $\mathcal{H}$  keep their action  $\mathbf{J}$  constant during the dynamic and their angle evolves with time as  $\mathbf{w} = \Omega(\mathbf{J})t + \mathbf{w}_0$  where  $\mathbf{w}_0$  is the angle at  $t = 0$  and  $\Omega(\mathbf{J}) = \partial\mathcal{H}/\partial\mathbf{J}$  is the angular frequency [4].

The equations for the evolution of the smooth distribution function  $f$  and its fluctuation  $\delta f$  are [5,6]

$$\frac{\partial f}{\partial t} = \frac{\partial}{\partial \mathbf{J}} \cdot \left\langle \delta f \frac{\partial \delta \phi}{\partial \mathbf{w}} \right\rangle, \quad (10a)$$

$$\frac{\partial \delta f}{\partial t} + \Omega(\mathbf{J}) \cdot \frac{\partial \delta f}{\partial \mathbf{w}} - \frac{\partial \delta \phi}{\partial \mathbf{w}} \cdot \frac{\partial f}{\partial \mathbf{J}} = 0. \quad (10b)$$

Despite these equations seeming as simple as Eqs. (7), the difficulty (i) described in the first paragraph of this section is not solved; the complexity of the unperturbed orbits is hidden in the change of variables, which makes the expression of the potential very complicated.

Following the same procedure as the one described in the homogeneous case, we get the Lenard-Balescu-type kinetic equation in action-angle variables [6,7],

$$\begin{aligned} \frac{\partial f}{\partial t} = & \pi(2\pi)^d m \frac{\partial}{\partial \mathbf{J}} \cdot \sum_{\mathbf{k}, \mathbf{k}'} \int d\mathbf{J}' \mathbf{k} \frac{\delta[\mathbf{k} \cdot \Omega(\mathbf{J}) - \mathbf{k}' \cdot \Omega(\mathbf{J}')] }{|D_{\mathbf{k}, \mathbf{k}'}(\mathbf{J}, \mathbf{J}', \mathbf{k} \cdot \Omega(\mathbf{J}))|^2} \\ & \times \left( \mathbf{k} \cdot \frac{\partial}{\partial \mathbf{J}} - \mathbf{k}' \cdot \frac{\partial}{\partial \mathbf{J}'} \right) f(\mathbf{J}, t) f(\mathbf{J}', t) \end{aligned} \quad (11)$$

where

$$\frac{1}{D_{\mathbf{k}, \mathbf{k}'}(\mathbf{J}, \mathbf{J}', \omega)} = \sum_{\alpha, \alpha'} \hat{\Phi}_\alpha(\mathbf{k}, \mathbf{J}) (\epsilon^{-1})_{\alpha, \alpha'}(\omega) \hat{\Phi}_{\alpha'}^*(\mathbf{k}', \mathbf{J}'), \quad (12)$$

and  $\epsilon_{\alpha\alpha'}(\omega)$  is the dielectric tensor

$$\epsilon_{\alpha\alpha'}(\omega) = \delta_{\alpha\alpha'} + (2\pi)^d \sum_{\mathbf{k}} \int d\mathbf{J} \frac{\mathbf{k} \cdot \partial f / \partial \mathbf{J}}{\mathbf{k} \cdot \Omega(\mathbf{J}) - \omega} \times \hat{\Phi}_\alpha^*(\mathbf{k}, \mathbf{J}) \hat{\Phi}_{\alpha'}(\mathbf{k}, \mathbf{J}). \quad (13)$$

The indices  $(\alpha, \alpha')$  are labels for a bi-orthogonal basis  $\{\rho_\alpha, \Phi_\alpha\}$  for the density and the potential [8], where  $\rho(\mathbf{r}) = \int f(\mathbf{r}, \mathbf{v}, t) d\mathbf{v}$ , which satisfies [8]

$$\int u(|\mathbf{r} - \mathbf{r}'|) \rho_\alpha(\mathbf{r}') d\mathbf{r}' = \Phi_\alpha \quad (14)$$

$$\int \rho_\alpha(\mathbf{r}) \Phi_{\alpha'}^*(\mathbf{r}) d\mathbf{r} = -\delta_{\alpha, \alpha'}. \quad (15)$$

The terms  $\hat{\Phi}_\alpha$  are the Fourier transforms of the potential in the bi-orthogonal representation with respect to the angles  $\hat{\Phi}_\alpha(\mathbf{k}, \mathbf{J}) = \frac{1}{(2\pi)^d} \int d\mathbf{w} e^{-i\mathbf{k}\cdot\mathbf{w}} \Phi_\alpha(\mathbf{w}, \mathbf{J})$ . The Lenard-Balescu equation (11) gives the evolution of  $f$  due to the inclusion of a finite- $N$  correction to the collision-less (Vlasov) kinetic equation. From equation (11), we see that the evolution, which slowly deforms the orbits of constant  $\mathbf{J}$ , is driven by resonances between orbital frequencies,  $\mathbf{k}\cdot\Omega(\mathbf{J}) = \mathbf{k}'\cdot\Omega(\mathbf{J}')$ . This differs from the homogeneous case, equation (9), where  $f$  evolves due to the resonances  $\mathbf{v} = \mathbf{v}'$ .

From the Lenard-Balescu-type equation (11) it is possible to compute diffusion coefficients, defined as  $D_{dif}^{ij}(\mathbf{J}, t) = \lim_{\Delta t \rightarrow 0} \langle \Delta J_i(t) \Delta J_j(t) \rangle / \Delta t$ :

$$D_{dif}^{ij}(\mathbf{J}, t) = \pi(2\pi)^d m \sum_{\mathbf{k}, \mathbf{k}'} \int d\mathbf{J}' k_i k_j \frac{\delta[\mathbf{k}\cdot\Omega(\mathbf{J}) - \mathbf{k}'\cdot\Omega(\mathbf{J}')] }{|D_{\mathbf{k}, \mathbf{k}'}(\mathbf{J}, \mathbf{J}', \mathbf{k}'\cdot\Omega(\mathbf{J}'))|^2} f(\mathbf{J}', t). \quad (16)$$

When collective effects are not considered, we have  $\epsilon_{\alpha\alpha'} = \delta_{\alpha\alpha'}$ .

### 3 Kinetic equations for the Hamiltonian Mean-Field model

We will compute explicitly the diffusion coefficients for the HMF model [9]. It is given by the Hamiltonian

$$H = \sum_{i=1}^N \frac{p^2}{2} - \frac{1}{2N} \sum_{i,j=1}^N \cos(\theta_i - \theta_j). \quad (17)$$

This model corresponds to a simplified model of one-dimensional gravity, in which only the first harmonic of a Fourier expansion on the potential is considered. This model is widely studied because many calculations can be performed analytically. The energy of one particle can be written as

$$h(\theta, p) = \frac{p^2}{2} + \phi(\theta) = \frac{p^2}{2} - \frac{1}{N} \sum_{i=1}^N \cos(\theta_i - \theta). \quad (18)$$

The potential  $\phi(\theta) = -1/N \sum_i \cos(\theta_i - \theta)$  can be rewritten as

$$\phi(\theta) = -\frac{\sum_{i=1}^N \cos \theta_i}{N} \cos \theta - \frac{\sum_{i=1}^N \sin \theta_i}{N} \sin \theta = -M_x \cos \theta - M_y \sin \theta \quad (19)$$

where  $\mathbf{M} = (M_x, M_y)$  is the magnetization vector. Its modulus  $M$  quantifies how bunched, or clustered, the particles are. From Eq. (19) we can see that,

when  $M_x$  and  $M_y$  are approximately constant, the particles motion corresponds to a real pendulum. The action variables can be computed analytically:

$$J(\kappa) = \frac{4\sqrt{M_0}}{\pi} \begin{cases} 2 [E(\kappa) - (1 - \kappa^2)K(\kappa)], & \kappa < 1 \\ \kappa E\left(\frac{1}{\kappa}\right), & \kappa > 1 \end{cases} \quad (20)$$

where  $M_0$  is the magnetization of the Quasi-Stationary state,  $E(x)$  is the complete Legendre elliptic integral of the second kind and  $\kappa = \sqrt{(1 + h/M_0)/2}$ . The angular frequency can be computed analytically,

$$\Omega(\kappa) = \pi\sqrt{M_0} \begin{cases} \frac{1}{2K(\kappa)}, & \kappa < 1 \\ \frac{\kappa}{K\left(\frac{1}{\kappa}\right)}, & \kappa > 1, \end{cases} \quad (21)$$

where  $K(x)$  is the complete elliptic integral of the first kind. It is also possible to compute analytically the bi-orthogonal basis, which is composed by only two family of functions in this case. We will call them  $c_l(\kappa)$  and  $s_l(\kappa)$  (see [1] for detailed expressions). This permits us to express all the quantities of interest analytically, except the dielectric tensor, for which numerical integrals have to be performed:

$$\epsilon_{cc/ss}(\omega) = 1 + 2\pi \sum_{\ell=-\infty}^{\infty} \int_0^{\infty} d\kappa \frac{g_{\ell}^{cc/ss}(\kappa)}{\Omega(\kappa) - \omega/\ell'} \quad (22)$$

where

$$g_{\ell}^{cc}(\kappa) = |c_{\ell}(\kappa)|^2 \partial f / \partial \kappa \quad (23a)$$

$$g_{\ell}^{ss}(\kappa) = |s_{\ell}(\kappa)|^2 \partial f / \partial \kappa. \quad (23b)$$

The final expression for the diffusion coefficient is

$$D_{dif}(\kappa) = \frac{2\pi^2}{N} \sum_{n,n'=-\infty}^{\infty} \sum_{\kappa^*} \frac{n^2 |\partial J / \partial \kappa|_{\kappa^*}}{|D_{nn'}(\kappa, \kappa^*, n\Omega(\kappa))|^2} \frac{f(\kappa^*, t)}{\left| n' \frac{\partial \Omega}{\partial \kappa'} \right|_{\kappa^*}} \quad (24)$$

where  $\kappa^*$  are the roots of the equation  $m\Omega(\kappa) - m'\Omega(\kappa') = 0$  and

$$\frac{1}{D_{nn'}(\kappa, \kappa', \omega)} = \frac{c_n(\kappa)c_{n'}(\kappa')}{\epsilon_{cc}(\omega)} - \frac{s_n(\kappa)s_{n'}(\kappa')}{\epsilon_{ss}(\omega)}. \quad (25)$$

It is usually necessary to take a only few terms of the sum over  $n$  and  $n'$  in Eq. (24) to obtain accurate results (see [1]).

## 4 Numerical checking

In this section we check the diffusion coefficients (24) with molecular dynamics (MD) simulations. The details can be found in [1]. In Figure 1 we show an excellent agreement between theory and simulations for Quasi-Stationary states with different values of the magnetization  $M_0$  (which measures the clusterization of the system). We performed simulations suppressing the collective effects (top panels) and with collective effects (bottom panels). Row (a) corresponds to high magnetization (very clustered states), row (b) to intermediate magnetization and row (c) low magnetization (quasi-homogeneous configuration). A very good agreement between theory and simulations is observed in all cases.

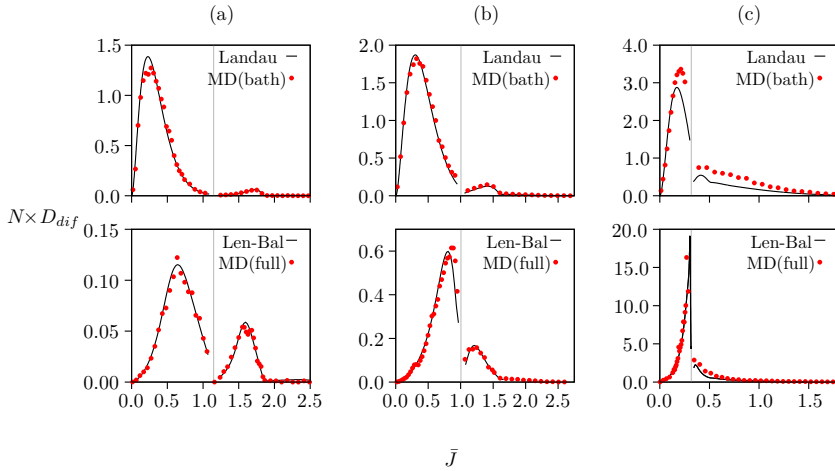


**Fig. 1** Diffusion coefficients calculated by molecular dynamics, compared to the theoretical results, for an equilibrium distribution with magnetization (a)  $M_0 = 0.816$ , (b)  $M_0 = 0.622$  and (c)  $M_0 = 0.06$ . On the bottom, MD simulations without collective effects, with the prediction of the Landau equation ( $\epsilon_{ss} = \epsilon_{cc} = 1$ ). On the top, MD simulations with collective effects with the theoretical curve predicted by the Lenard-Balescu (Len-Bal) equation, and the molecular dynamics given by the regular HMF model – MD(full).

## References

1. F. P. C. Benetti and B. Marcos. Collisional relaxation in the inhomogeneous Hamiltonian mean-field model: Diffusion coefficients. *Phys. Rev. E*, **95**:022111, 2017.

2. P. H. Chavanis. Kinetic theory of spatially homogeneous systems with long-range interactions: I. General results. *The European Physical Journal Plus*, **127**:19, 2012.
3. J. Binney and S. Tremaine. *Galactic Dynamics*. Princeton University Press, 2008.
4. H. Goldstein. *Classical Mechanics*. Pearson Education, 2002.
5. J. F. Luciani and R. Pellat. Kinetic equation of finite Hamiltonian systems with integrable mean field. *Journal de Physique*, **48**:591–599, 1987.
6. P.-H. Chavanis. Kinetic theory of long-range interacting systems with angle-action variables and collective effects. *Physica A*, **391**:3680, 2012.
7. J. Heyvaerts. A Balescu-Lenard-type kinetic equation for the collisional evolution of stable self-gravitating systems. *MNRAS*, **407**, 2010.
8. A. J. Kalnajs. Dynamics of Flat Galaxies. II. Biorthonormal Surface Density-Potential Pairs for Finite Disks. *Astrophysical Journal*, **205**:745, 1976.
9. Mickael Antoni and Stefano Ruffo. Clustering and relaxation in hamiltonian long-range dynamics. *Phys. Rev. E*, **52**:2361–2374, Sep 1995.



# Optimal control of slow-fast mechanical systems

Jean-Baptiste Caillau, Lamberto Dell'Elce,  
Jean-Baptiste Pomet and Jérémy Rouot

**Abstract** We consider the minimum time control of dynamical systems with slow and fast state variables. With applications to perturbations of integrable systems in mind, we focus on the case of problems with one or more fast angles, together with a small drift on the slow part modelling a so-called secular evolution of the slow variables. According to Pontrjagin maximum principle, minimizing trajectories are projections on the state space of Hamiltonian curves. In the case of a single fast angle, it turns out that, provided the drift on the slow part of the original system is small enough, time minimizing trajectories can be approximated by geodesics of a suitable metric. As an application to space mechanics, the effect of the  $J_2$  term in the Earth potential on the control of a spacecraft is considered. In ongoing work, we also address the more involved question of systems having two fast angles.

---

J.-B. Caillau

LJAD, Univ. Côte d'Azur & CNRS/Inria, Parc Valrose, F-06108 Nice e-mail: [jean-baptiste.caillau@univ-cotedazur.fr](mailto:jean-baptiste.caillau@univ-cotedazur.fr)

L. Dell'Elce

Inria Sophia Antipolis Méditerranée, Univ. Côte d'Azur, 2004 route des lucioles, F-06902 Valbonne e-mail: [lamberto.dell-elce@inria.fr](mailto:lamberto.dell-elce@inria.fr)

J.-B. Pomet

Inria Sophia Antipolis Méditerranée, Univ. Côte d'Azur, 2004 route des lucioles, F-06902 Valbonne e-mail: [jean-baptiste.pomet@inria.fr](mailto:jean-baptiste.pomet@inria.fr)

J. Rouot

École Polytechnique Féminine, 2 rue Sastre, F-10430 Rosières-près-Troyes e-mail: [jeremy.rouot@epf.fr](mailto:jeremy.rouot@epf.fr)

## Introduction

We consider the following slow-fast control system on an  $n$ -dimensional manifold  $M$ :

$$\frac{dI}{dt} = \varepsilon F_0(I, \varphi, \varepsilon) + \varepsilon \sum_{i=1}^m u_i F_i(I, \varphi, \varepsilon), \quad |u| = \sqrt{u_1^2 + \cdots + u_m^2} \leq 1, \quad (1)$$

$$\frac{d\varphi}{dt} = \omega(I) + \varepsilon G_0(I, \varphi, \varepsilon) + \varepsilon \sum_{i=1}^m u_i G_i(I, \varphi, \varepsilon), \quad \omega(I) > 0, \quad (2)$$

with  $I \in M$ ,  $\varphi \in \mathbf{S}^1$ ,  $u \in \mathbf{R}^m$ , and fixed extremities  $I_0, I_f$ , and free phases  $\varphi_0, \varphi_f$ . All the data is periodic with respect to the single fast angle  $\varphi$ , and  $\omega$  is assumed to be positive on  $M$ . Extensions are possible to the case of several phases but resonances must then be taken into account.

In the first section, we focus on systems with a single fast angle. The Hamiltonian system provided by applying Pontrjagin maximum principle is averaged after properly identifying the slow variables. The averaged system turns out to be associated with a metric approximation of the original problem. We apply the method to space mechanics, and show how the  $J_2$  term in the Earth potential is responsible for the asymmetry of the metric. In the second section, we give a preliminary analysis of multiphase averaging for minimum time control problems. The case of two fast angles is considered on a simple example. A crucial step is to define a suitable near-identity transformation of the initial state and costate. This work is related with other methods applicable to slow-fast control systems. (See, e.g., the recent papers [1–3, 6].)

## 1 Metric approximation in the case of a single fast phase

### 1.1 Averaging the extremal flow

According to Pontrjagin maximum principle, time minimizing curves are projections onto the base space  $M \times \mathbf{S}^1$  of integral curves (*extremals*) of the maximized Hamiltonian below:

$$H(I, \varphi, p_I, p_\varphi, \varepsilon) := p_\varphi \omega(I) + \varepsilon K(I, \varphi, p_I, p_\varphi, \varepsilon),$$

$$K := H_0 + \sqrt{\sum_{i=1}^m H_i^2},$$

$$H_i(I, \varphi, p_I, p_\varphi, \varepsilon) := p_I F_i(I, \varphi, \varepsilon) + p_\varphi G_i(I, \varphi, \varepsilon), \quad i = 0, \dots, m.$$

There are two types of extremals: abnormal ones that live on the level set  $\{H = 0\}$ , and normal ones that evolve on nonzero levels of the Hamiltonian. One defines the averaged Hamiltonian  $\bar{K}$  as

$$\begin{aligned} \bar{K} &:= \bar{H}_0 + \bar{K}_0, \quad \bar{H}_0 := \langle p_I, \bar{F}_0 \rangle, \\ \bar{K}_0(I, p_I) &:= \frac{1}{2\pi} \int_0^{2\pi} \sqrt{\sum_{i=1}^m H_i^2(I, \varphi, p_I, p_\varphi = 0, \varepsilon = 0)} d\varphi. \end{aligned} \quad (3)$$

It is smooth on the open set  $\Omega$  equal to the complement of  $\bar{\Sigma}^c$  where

$$\Sigma := \{(I, p_I, \varphi) \in T^*M \times \mathbf{S}^1 \mid (\forall i = 1, m) : \langle p_I, F_i(I, \varphi, \varepsilon = 0) \rangle = 0\},$$

$$\bar{\Sigma} := \omega(\Sigma) \quad \omega : T^*M \times \mathbf{S}^1 \rightarrow T^*M.$$

One also defines the open submanifold  $M_0 := \Pi(\Omega)$  of  $M$ . We assume that  $M_0$  is connex. Under the assumption

$$(A1) \text{ rank}\{\partial^j F_i(I, \varphi, \varepsilon = 0) / \partial \varphi^j, i = 1, \dots, m, j \geq 0\} = n, (I, \varphi) \in M \times \mathbf{S}^1,$$

one is able to express some properties of the averaged Hamiltonian in terms of Finsler metric. (We refer the reader, *e.g.*, to [5] for an introduction to Finsler geometry.)

**Proposition 1.** *The symmetric part  $\bar{K}_0 : (\Omega \subset) T^*M \rightarrow \mathbf{R}$  of the tensor  $\bar{K}$  is positive definite and 1-homogenous. It so defines a symmetric Finsler co-norm.*

We assume moreover that

$$(A2) \bar{K}_0(I, \bar{F}_0^*(I)) < 1, I \in M,$$

where  $\bar{F}_0^*$  is the inverse Legendre transform of  $\bar{F}_0$ . Under this new assumption, one has

**Proposition 2.** *The tensor  $\bar{K} = \bar{H}_0 + \bar{K}_0$  is positive definite and defines an asymmetric Finsler co-norm.*

The geodesics are the integral curves of the Hamiltonian  $\bar{K}$  restricted to the level set  $\{\bar{K} = 1\}$ ,

$$\frac{dI}{d\tau} = \frac{\partial \bar{K}}{\partial p_I}, \quad \frac{dp_I}{d\tau} = -\frac{\partial \bar{K}}{\partial I},$$

$$I(0) = I_0, \quad I(\tau_f) = I_f, \quad \bar{K}(I_0, p_I(0)) = 1,$$

and  $\tau_f = d(I_0, I_f)$  for minimizing ones. The convergence properties of the original system towards this metric when  $\varepsilon \rightarrow 0$  are studied in [4].

## 1.2 Application to space mechanics

We consider the two-body potential case,

$$\dot{q} = -\mu \frac{q}{|q|^3} + \frac{u}{M}, \quad |u| \leq T_{\max}.$$

Thanks to the super-integrability of the  $-1/|q|$  potential, the minimum time control system is slow-fast with only angle (the longitude of the evolving body) if one restricts to the case of transfers between elliptic orbits ( $\mu$  is the gravitational constant). In the non-coplanar situation, we have to analyze a dimension five symmetric Finsler metric. In order to account for the Earth non-oblateness, we add to the dynamics a small drift  $F_0$  on the slow variables. In the standard equinoctial orbit elements,  $I = (a, e, \omega, \Omega, i)$ , the  $J_2$  term of order  $1/|q|^3$  of the Earth potential derives from the additional potential ( $r_e$  being the equatorial radius)

$$R_0 = \frac{\mu J_2 r_e^2}{|q|^3} \left( \frac{1}{2} - \frac{3}{4} \sin^2 i + \frac{3}{4} \sin^2 i \cos 2(\omega + \varphi) \right)$$

where  $\varphi$  is the true anomaly. As a result, the system now has two small parameters (depending on the initial condition). One is due to the  $J_2$  effect, the other to the control:

$$\varepsilon_0 = \frac{3J_2 r_e^2}{2a_0^2}, \quad \varepsilon_1 = \frac{a_0^2 T_{\max}}{\mu M}.$$

Here,  $a_0$  is the initial semi-major axis,  $T_{\max}$  the maximum level of thrust, and  $M$  the spacecraft mass. We make a reduction to a single small parameter as follows: Defining  $\varepsilon := \varepsilon_0 + \varepsilon_1$  and  $\lambda := \varepsilon_0 / (\varepsilon_0 + \varepsilon_1)$ , one has

$$\begin{aligned} \frac{dI}{dt} &= \varepsilon_0 F_0(I, \varphi) + \varepsilon_1 \sum_{i=1}^m u_i F_i(I, \varphi), \\ &= \varepsilon \left( \lambda F_0(I, \varphi) + (1 - \lambda) \sum_{i=1}^m u_i F_i(I, \varphi) \right). \end{aligned}$$

There are two regimes depending on whether the  $J_2$  effect is small against the control ( $\varepsilon_0 \ll \varepsilon_1$  and  $\lambda \rightarrow 0$ ) or not ( $\varepsilon_0 \gg \varepsilon_1$  and  $\lambda \rightarrow 1$ ). The critical ratio on  $\lambda$  can be explicitly computed in metric terms.

**Proposition 3.** *In the average system of the two-body potential including the  $J_2$  effect,  $\bar{K} = \lambda \bar{H}_0 + (1 - \lambda) \bar{K}_0$  is a metric tensor if and only if  $\lambda < \lambda_c(I)$  with*

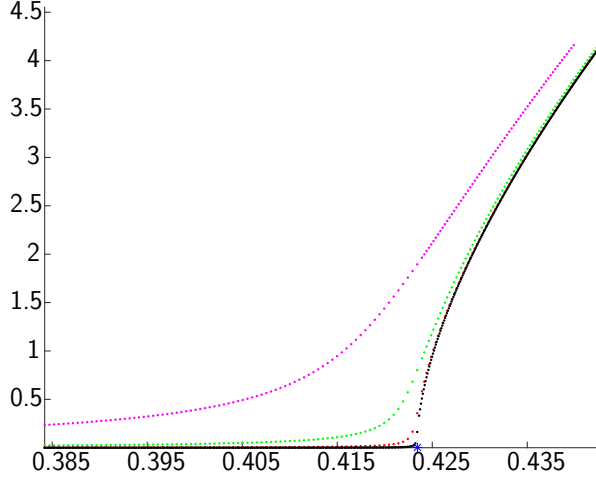


**Fig. 1** Value function  $\lambda \mapsto \tau_f(\lambda)$ ,  $\tau_d \rightarrow 0$  (averaged system). On this example,  $a = 30$  Mm,  $e = 0.5$ ,  $\omega = \Omega = 0$ ,  $i = 51$  degrees (strong inclination), and  $\lambda_c \simeq 0.4239$ . The value function is portrayed for  $\tau_d = 1e-2, 1e-3, 1e-4, 1e-5$ .

$$\lambda_c(I) = \frac{1}{1 + \bar{K}_0(I, \bar{F}_0^*(I))}.$$

The relevance of this critical ratio for the qualitative analysis of the original system is illustrated by the numerical simulations displayed in Figures 2 to 4. For a given initial condition  $I_0$  on the slow variables, we let the drift  $F_0$  alone act: We integrate the flow of  $F_0$  during a short positive duration  $\tau_d$ , then compute the trajectory of the averaged system to go from this point  $I(\tau_d)$  back to  $I_0$ . For  $\lambda < \lambda_c(I_0)$ , the tensor  $\bar{K}$  is a metric one, and this trajectory is a geodesic. As  $\tau_d$  tends to zero, the time  $\tau_f$  to come back from  $I(\tau_d)$  tends to zero when  $\lambda < \lambda_c(I_0)$ . For  $\lambda \geq \lambda_c(I_0)$ , finiteness of this time indicates that global properties of the system still allows to control it although the metric character of the approximation does not hold anymore. (See Figure 2.) The behaviour of  $\tau_f$  measures the loss in performance as  $\lambda$  approaches the critical ratio. This critical value depends on the initial condition and gives an asymptotic estimate of whether the thrust dominates the  $J_2$  effect or not. Beyond the critical value, the system is still controllable, but there is a drastic change in performance. As the original system is approximated by the average one, this behaviour is very precisely reproduced on the value function of the original system for small enough  $\varepsilon$ . (See Figures 3 to 4.)

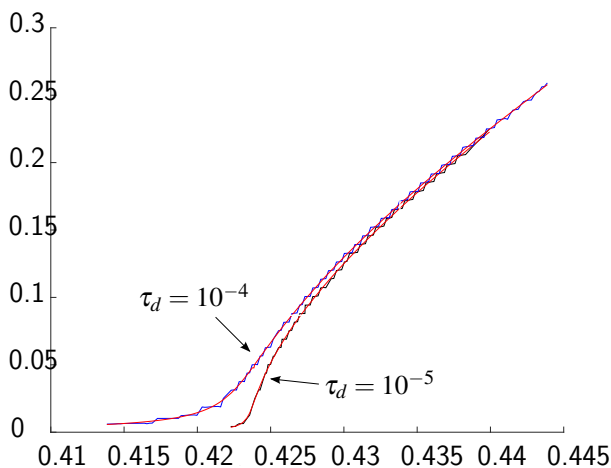


**Fig. 2** Value function  $\lambda \mapsto \tau_f(\lambda)$ ,  $\tau_d \rightarrow 0$  (original system,  $\varepsilon = 1e - 3$ ). On this example,  $a = 30$  Mm,  $e = 0.5$ ,  $\omega = \Omega = 0$ ,  $i = 51$  degrees (strong inclination), and  $\lambda_c \simeq 0.4239$ . The behaviour of the value function for the original system matches very precisely the behaviour of the averaged one. (See also Figure 4 for a even lower value of  $\varepsilon$ .)

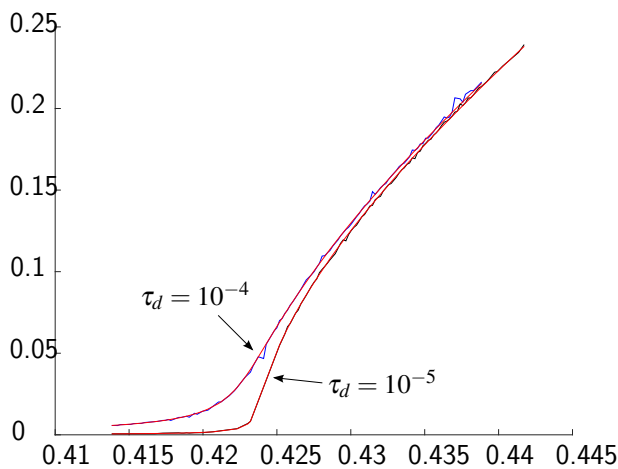


**Fig. 3** Value function  $\lambda \mapsto \tau_f(\lambda)$ ,  $\tau_d \rightarrow 0$  (original system,  $\varepsilon = 1e - 4$ ). On this example,  $a = 30$  Mm,  $e = 0.5$ ,  $\omega = \Omega = 0$ ,  $i = 51$  degrees (strong inclination), and  $\lambda_c \simeq 0.4239$ . The behaviour of the value function for the original system matches very precisely the behaviour of the averaged one.

## 2 Averaging control systems with two fast angles

### 2.1 A simple example

In order to illustrate our preliminary analysis of multiphase averaging for control systems, we consider an elementary dynamical system consisting of a scalar slow variable,  $I$ , and two fast variables,  $\zeta$  and  $\psi$ . The optimal control problem is

$$\begin{aligned} \min_{\sqrt{u_1^2 + u_2^2} \leq 1} t_f \quad \text{subject to :} \\ \frac{dI}{dt} = \varepsilon [\cos \zeta + \cos(\zeta - \psi) u_1 + u_2], \quad \frac{d\zeta}{dt} = I, \quad \frac{d\psi}{dt} = 1, \quad (4) \\ I(0) = I_0, \quad I(t_f) = I_f. \end{aligned}$$

We note that the frequency of  $\psi$  is constant. If one of the two frequencies is non-vanishing on the ambient manifold  $M$ , any problem with two frequencies can be recast into this form by means of a change of the time variable, as emphasized in [8]. The Hamiltonian associated to Problem (4) is

$$H = Ip_\zeta + p_\psi + \varepsilon \left[ p_I \cos \zeta + |p_I| \sqrt{1 + \cos^2(\zeta - \psi)} \right]. \quad (5)$$

The maximizing control is

$$u_1^{opt} = \frac{p_I}{|p_I|} \frac{\cos(\zeta - \psi)}{\sqrt{1 + \cos^2(\zeta - \psi)}}, \quad u_2^{opt} = \frac{p_I}{|p_I|} \frac{1}{\sqrt{1 + \cos^2(\zeta - \psi)}},$$

revealing that the sign of  $p_I$  determines the direction of the control vector, which imposes a secular drift to the slow variable. Numerical values used in all simulations are  $\varepsilon = 10^{-3}$  and  $I_0 = \sqrt{2}/2$ . Applying averaging theory to the extremal flow of this problem is questionable because the structure of this vector field differs from the one of conventional fast-oscillating systems. As in the case of one fast angle, the equation of motion of  $p_I$  includes the term  $p_\varphi \partial \omega / \partial I$  that may be of order larger than  $\varepsilon$ . Hence, adjoints of slow variables are not necessary slow themselves. We justify the application of averaging theory to System (14) by showing that, as in the case of a single fast phase discussed in the previous section, adjoints of fast variables remain  $\varepsilon$ -small for any extremal trajectory with free phases.

Consider the canonical change of variables  $\{I, p_I, \varphi, p_\varphi\} \rightarrow \{J, p_J, \psi, p_\psi\}$  such that

$$J = I, \quad \psi = \Omega(I) \varphi, \quad (6)$$

where the matrix-valued function,  $\Omega : M \rightarrow \mathbf{R}^{2 \times 2}$  is defined as

$$\Omega := \frac{1}{\|\omega(I)\|} \begin{bmatrix} \omega_1(I) & \omega_2(I) \\ -\omega_2(I) & \omega_1(I) \end{bmatrix}. \quad (7)$$

Symplectic constraints yield the transformation of the adjoints

$$p_I = p_J + p_\psi \frac{\partial \Omega}{\partial J} \Omega^T \psi, \quad p_\varphi = p_\psi \Omega(J), \quad (8)$$

so that the transformed Hamiltonian is

$$\tilde{H} = \|\omega(J)\| p_{\psi_1} + \varepsilon \underbrace{K\left(J, p_J + p_\psi \frac{\partial \Omega}{\partial J} \Omega^T \psi, \Omega^T \psi, p_\psi \Omega\right)}_{:= \tilde{K}(J, p_J, \psi, p_\psi)}. \quad (9)$$

Boundary conditions on the adjoints of fast variables require that  $p_\varphi(0) = 0$ . Evaluating the Hamiltonian at the initial time and normalizing the initial adjoints according to  $\|p_{I_0}\| = 1$ , one sets

$$\varepsilon h := \tilde{H}(t=0) = \varepsilon \underbrace{K\left(I_0, p_{I_0}, \Omega^T(I_0) \psi_0, 0\right)}_{O(1)}. \quad (10)$$

Hence,  $p_{\psi_1}$  can be evaluated at any time by solving the implicit function

$$p_{\psi_1} = \varepsilon \frac{h - \tilde{K}(J, p_J, \psi, p_\psi)}{\|\omega(J)\|} \approx \frac{h - \tilde{K}(J, p_J, \psi, 0)}{\|\omega(J)\|} \quad (11)$$

Equation (11) indicates that  $p_{\psi_1} = O(\varepsilon)$  when evaluated on a candidate optimal trajectory. As a consequence,  $p_J$  has an  $\varepsilon$ -slow dynamics, *i.e.*

$$\frac{d p_J}{d t} = - \underbrace{\frac{\partial \|\omega\|}{\partial J} p_{\psi_1}}_{O(\varepsilon)} - \varepsilon \frac{\partial \tilde{K}}{\partial J} = O(\varepsilon), \quad (12)$$

which justifies the averaging of the extremal flow. As before, we denote by  $\bar{K}$  the averaged Hamiltonian

$$\bar{K} := \frac{1}{4\pi^2} \int_{\mathbf{T}^2} K(I, p_I, \varphi, 0) \, d\varphi. \quad (13)$$

Here,  $p_\varphi = 0$  because the averaging is carried out by considering the limit of the function as  $\varepsilon$  approaches zero. Averaging the extremal flow yields

$$\begin{aligned}
 \frac{d\bar{I}}{dt} &= \varepsilon \frac{\partial \bar{K}}{\partial \bar{p}_I}, & \frac{d\bar{p}_I}{dt} &= -\varepsilon \frac{\partial \bar{K}}{\partial \bar{I}} - \bar{p}_\varphi \frac{\partial \omega}{\partial \bar{I}}, \\
 \frac{d\varphi}{dt} &= \varepsilon \frac{\partial \bar{K}}{\partial \bar{p}_\varphi} + \omega(\bar{I}), & \frac{d\bar{p}_\varphi}{dt} &= 0.
 \end{aligned} \tag{14}$$

## 2.2 Near-identity transformation of the initial state and costate

Changing the initial conditions of averaged trajectories allows one to reduce the drift between  $I(t)$  and  $\bar{I}(t)$ . Qualitatively, one defines a transformation that shifts the initial point of the averaged trajectory to the middle of the short-period oscillations of  $I(t)$ . The improvement obtained with this expedient is possibly negligible when compared to the estimate provided by Neishtadt theorem for systems with two fast angles [8], which considers the same initial conditions for the two trajectories. Nonetheless, the transformation of the initial variables plays a key role for the optimal control problem. (See [7] for a detailed discussion.) Figure 4 shows that  $p_I$  and  $\bar{p}_I$  exhibit a steady drift that largely exceeds the expected small drift when the original and averaged systems are integrated with the same initial conditions. In addition, trajectories of the original system strongly depend on the initial angles. We show in the sequel that transforming the adjoints of fast variables is sufficient to drastically reduce the drift of  $p_I$ .

The trigger at the origin of the drift of  $p_I$  is the wrong assessment of the averaged value of  $p_\varphi$ , as shown in the bottom of Figure 4. This error is of order  $\varepsilon$  but it induces a steady drift of  $\bar{p}_I$  of the same order of magnitude,

$$\frac{d\bar{p}_I}{dt} = \underbrace{-\bar{p}_\varphi \frac{\partial \omega}{\partial \bar{I}}}_{\varepsilon\text{-small error}} - \varepsilon \frac{\partial \bar{K}}{\partial \bar{I}}. \tag{15}$$

In turn, an  $\varepsilon$ -small error on  $\bar{p}_\varphi$  induces a steady drift of  $\bar{p}_I$  that is comparable with its slow motion. Transforming the initial adjoints of fast variables is sufficient to greatly mitigate this problem. More precisely, initial conditions of the averaged and of the original initial value problem are mostly the same, *i.e.*

$$I(0) = \bar{I}(0) = I_0, \quad p_I(0) = \bar{p}_I(0) = p_{I_0}, \quad \varphi(0) = \varphi_0, \tag{16}$$

except for the adjoints of fast variables, which are such that

$$\bar{p}_\varphi(0) = \bar{p}_{\varphi_0} \quad \text{and} \quad p_\varphi(0) = \bar{p}_{\varphi_0} + \nu_{p_\varphi}(I_0, p_{I_0}, \varphi_0, \bar{p}_{\varphi_0}), \tag{17}$$

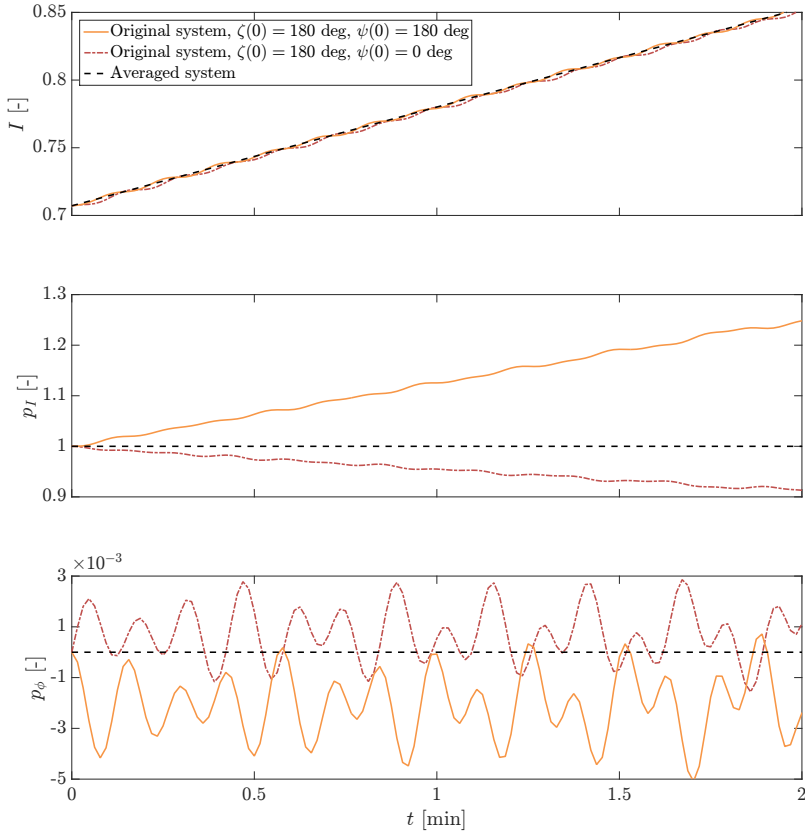


**Fig. 4** Numerical integration of the simple example. Trajectories of the original and averaged system emanate from the same point of the phase space. Initial adjoints are  $p_I(0) = 1$  and  $p_\psi(0) = p_\zeta(0) = 0$ .

where, assuming that  $I_0$  is in a non-resonant zone,  $v_{p_\varphi}$  is given by

$$v_{p_\varphi} = -i \sum_{0 < |k| \leq N} \frac{e^{ik \cdot \bar{\varphi}}}{k \cdot \omega(\bar{I})} \left[ -\frac{\partial K}{\partial \varphi} \right]^{(k)}. \quad (18)$$

As a result,  $p_\varphi$  oscillates with zero mean about  $\bar{p}_\varphi$ , and the drift between  $p_I(t)$  and  $\bar{p}_I(t)$  is drastically reduced.

Besides, changing  $p_\varphi$  is mandatory to have consistent trajectories of the averaged and original systems. Transforming the initial value of slow variables and their adjoints is less important, but it can further reduce the drift between these trajectories. Reconstructed trajectories (dash-dotted lines) of  $I$

and  $p_\varphi$  well overlap with their original counterpart, see Figure 5. Nevertheless, the reconstruction of  $p_I$  is wrong (in the very-specific case of the simple example,  $v_{p_I} = 0$ ). Again, the term  $p_\varphi \partial \omega / \partial I$  in the dynamics of  $p_I$  is responsible for this error. In fact, if short-period variations of  $p_\varphi$  are neglected, the Fourier expansion of the right-hand side is carried out by introducing  $\varepsilon$ -small errors in the evaluation of the  $\varepsilon$ -slow dynamics. The transformation of  $p_I$  should be carried out by including  $v_{p_\varphi}$  in the Fourier expansion, namely

$$v_{p_I} = -i \sum_{0 < |k| \leq N} \frac{e^{ik\bar{\varphi}}}{k \cdot \omega(\bar{I})} \left[ -\left(\bar{p}_\varphi + v_{p_\varphi}\right) \frac{\partial \omega}{\partial I} - \frac{\partial K}{\partial I} \right]^{(k)}. \quad (19)$$

Ongoing work is concerned with the extension of this analysis to resonant zones. When resonances of rather low order are crossed, one has to patch together resonant and non-resonant normal forms. Detecting properly where to patch these approximations will be the subject of further studies.

**Acknowledgements** Work supported by the French Space Agency (CNES R&T contract no. R-S13/BS-005-012); by Thales Alenia Space, Inria and UCA-JEDI Investissements d'avenir (ANR-15-IDEX-01, PEPS MSI); by the FMJH Program PGM0 and EDF-Thales-Orange (PGMO grant no. 2016-1753H). The authors thank Richard Epenoy (CNES) and Thierry Dargent (Thales Alenia Space) for many insightful exchanges.

## References

1. Bombrun, A.; Pomet, J.-B. The averaged control system of fast oscillating control systems. *SIAM J. Control Optim.* **51** (2013), no. 3, 2280–2305.
2. Bonnard, B.; Henninger, H.; Némcova, J.; Pomet, J.-B. Time versus energy in the averaged optimal coplanar Kepler transfer towards circular orbits. *Acta Appl. Math.* **135** (2015), no. 2, 47–80.
3. Caillaud, J.-B.; Dargent, T.; Nicolau, F. Approximation by filtering in optimal control and applications. *IFAC PapersOnLine* **50** (2017), no. 1, 1649–1654. Proceedings of the 20th IFAC world congress, Toulouse, July 2017.
4. Caillaud, J.-B.; Pomet, J.-B.; Rouot, J. Metric approximation of minimum time control systems. *HAL preprint* (2017), no. 01672001, 1–12.
5. Dahl, M. F. A brief introduction to Finsler geometry. Lecture notes, 2006. [math.aalto.fi/~fdahl/finsler/finsler.pdf](http://math.aalto.fi/~fdahl/finsler/finsler.pdf)
6. Dargent, T.; Nicolau, F.; Pomet, J.-B. Periodic averaging with a second order integral error. *IFAC PapersOnLine* **50** (2017), no. 1, 2892–2897. Proceedings of the 20th IFAC world congress, Toulouse, July 2017.
7. Dell'Elce, L.; Caillaud, J.-B.; Pomet, J.-B. Averaging optimal control systems with two fast variables *HAL preprint* (2018), no. 01793704, 1–18.
8. Lochak, P.; Meunier, C. *Multiphase averaging for classical systems*. Springer, 1988.

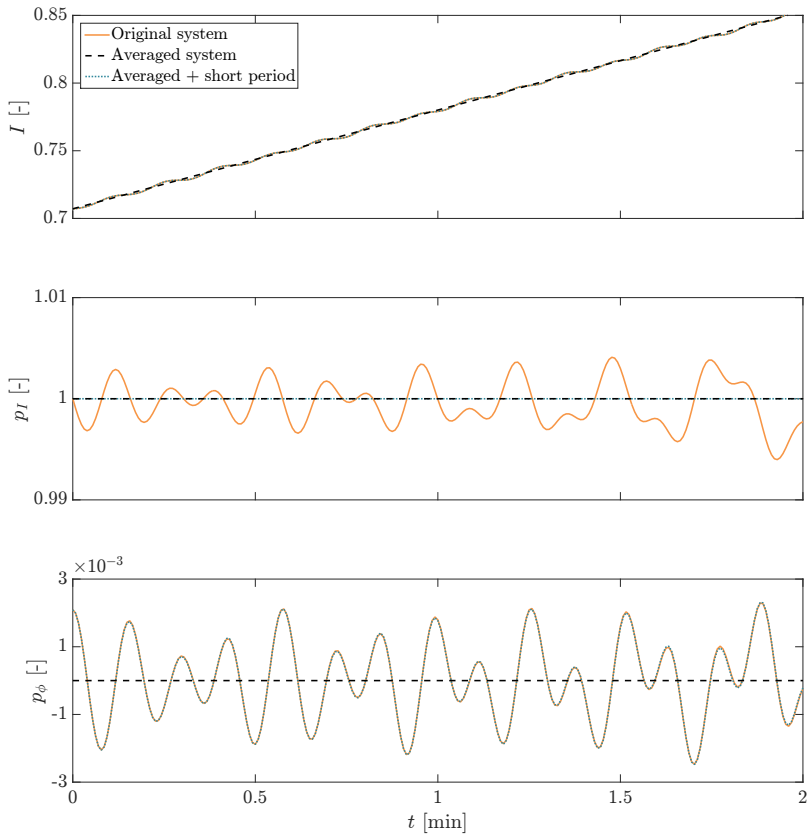


**Fig. 5** Reconstruction of short-period variations using an appropriate transformation of the initial state and costate.

# Light-induced self-organization in cold atomic clouds

Guillaume Labeyrie and Robin Kaiser

**Abstract** Patterns are ubiquitous in nature and have been extensively studied in biology, chemistry and physics including optics. We report here on experiments where pattern formation occurs in a cloud of laser cooled atoms. We identify three different mechanisms allowing spatial patterns to spontaneously emerge in either the atomic density, the excited state population, or the atomic spin state.

## 1 Experimental setup for self-organization in cold atoms

The typical setup used in these experiments is shown in [1](#). We prepare a cloud of cold  $^{87}\text{Rb}$  atoms in a magneto-optical trap (MOT) using large diameter trapping laser beams. The produced cloud is cold ( $\approx 100\ \mu\text{K}$ ), with a diameter larger than 1 cm, and contains up to  $10^{11}$  atoms. The optical density for light resonant with the atomic transition is large, typically 100. The ability to produce such large clouds is an important prerequisite to realize these experiments. Once the cloud is prepared, we release it from the trap by shutting down both MOT beams and magnetic field gradient. Shortly after release, the cloud is illuminated by a linearly-polarized, pulsed "pump" laser beam (pulse duration 1 ms to 1 ms) of waist 2 mm, which is frequency

---

Guillaume Labeyrie

Institut de Physique de Nice (INPHYNI), 06560 Valbonne, France e-mail: [guillaume.labeyrie@inphyni.cnrs.fr](mailto:guillaume.labeyrie@inphyni.cnrs.fr)

Robin Kaiser

Institut de Physique de Nice (INPHYNI), 06560 Valbonne, France e-mail: [robin.kaiser@inphyni.cnrs.fr](mailto:robin.kaiser@inphyni.cnrs.fr)

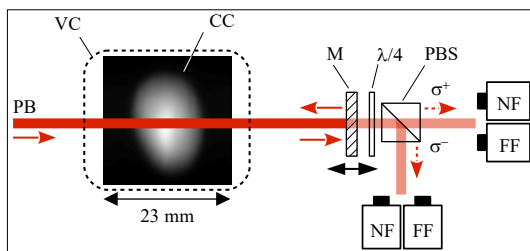


**Fig. 1** Experimental setup for pattern observation. VC: vacuum chamber. CC: cold cloud. PB: pump beam. M: mirror.  $\lambda/4$ : quarter-wave plate. PBS: polarizing beam-splitter.

detuned from the atomic transition by  $\delta$  (positive or negative). We use detunings larger than the atomic linewidth  $\Gamma$  (typically  $|\delta/\Gamma| \approx 10$ ) such that most of the pump beam is transmitted by the cloud. This transmitted beam is then retro-reflected by a mirror located at a distance  $d$  behind the cloud.

The cloud behaves as an optical medium with a nonlinear index of refraction. If a small fluctuation of this index occurs in the plane transverse to the beam propagation axis, a small phase fluctuation is imprinted on the transmitted beam. After propagation in free space over  $2d$ , this phase fluctuation turns into an intensity fluctuation due to diffraction. This intensity fluctuation reacts on the nonlinear index of the cloud (optical feedback), and leads to a spontaneous oscillation in the transverse plane above a certain intensity threshold. Thus, one observes the appearance of a spatially modulated light intensity distribution in the transverse plane, with an underlying spatially modulated atomic susceptibility. We observe these light patterns by imaging the beam's transverse cross-section at a distance  $2d$  after the cloud, using the small amount of light transmitted by the mirror as shown in 1. The field distributions can be recorded simultaneously in near-field (NF) and far-field (FF).

## 2 Different mechanisms for self-organization

In the course of this work, we observed different modes of self-organization depending on the experimental parameters. We demonstrated the existence of three distinct nonlinear mechanisms relying on different atomic degrees of freedom. In the following, we briefly describe these various mechanisms and the associated patterns.

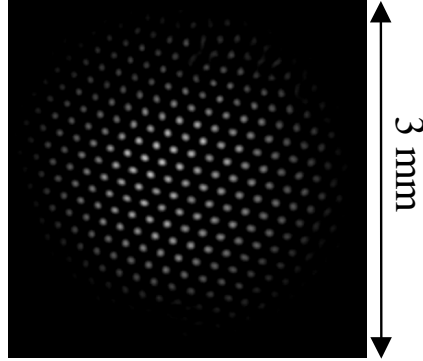


Fig. 2 Example of optomechanical patterns.

## 2.1 Optomechanical self-organization

This type of self-organization is observed for positive detunings, relatively low pump intensities ( $50 \text{ mW/cm}^2$ ) and pump pulse durations larger than  $100 \mu\text{s}$ . It relies on the dipole force exerted by the spatially modulated light on the cold atoms. Given sufficient time, the atoms spatially bunch into the potential wells, yielding a modulated index of refraction. Because the efficiency of this bunching process depends on the kinetic energy of the atoms, the intensity threshold for pattern formation depends of the temperature of the cloud in this situation. We show in 2 an example of self-organization in this case, where a nice hexagonal long range order is observed [1].

## 2.2 "Electronic" self-organization

To observe this type of self-organization we employ positive detunings as well, but higher pump beam intensities (above  $200 \text{ mW/cm}^2$ ) and much shorter probe pulses ( $\approx 1 \mu\text{s}$ ). In such a short time, the cold atoms cannot move over significant distances. Instead, the nonlinearity relies here on the saturation of the (quasi-2 level) atomic transition, which occurs when a significant amount of the population is transferred to the excited state. This is quantified by the so-called saturation parameter  $s = (I/I_{sat})/[1 + 4 \cdot (\delta/\Gamma)]^2$ . In this expression  $I$  is the pump laser intensity and  $I_{sat}$  an atomic parameter (here  $I_{sat} = 3.6 \text{ mW/cm}^2$ ). For  $s \ll 1$  the index of refraction is linear, for  $s \approx 1$  the index is Kerr-like and for  $s \gg 1$  the index saturates to 1. The observations reported in 3 are in agreement with this behavior. At low pump intensity (be-

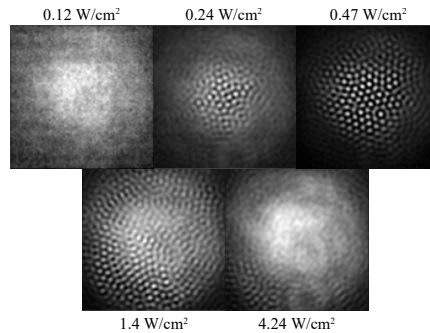


**Fig. 3** Behavior of electronic patterns versus pump intensity.

low threshold) nothing occurs, then upon increasing  $I$  patterns appear and develop, and disappear again at high intensities due to the saturation of the index of refraction [2].

### 2.3 *Spin self-organization*

This regime of self-organization is drastically different from the two previous ones. It requires a negative detuning, and an accurate cancellation of residual magnetic fields. Once this is achieved, we apply a weak ( $\approx 1$  G) magnetic field  $\mathbf{B}$  of controlled magnitude and direction, and observe the complex phase space shown in 4.

For  $B \approx 0$ , we observe structures with a square symmetry. The comparison of the images in the two circular polarization channels show that this is an anti-ferromagnetic state (AFM), with alternating domains with spin-up and spin-down atoms with equal populations [3, 4]. Increasing the longitudinal magnetic field  $B_z$  breaks the symmetry between  $s^+$  and  $s^-$  and results in a ferro-magnetic phase (FM) of hexagonal symmetry, where one spin orientation dominates. A further increase of  $B_z$  results in a different phase (“high- $B_z$  phase”), without long range order but with local hexagonal symmetry.

We also observe strikingly different behaviors versus transverse magnetic field. When the transverse magnetic field  $B_y$  (orthogonal to the input polarization) is increased, all patterns vanish. To the contrary, when  $B_x$  (parallel to the input polarization) is increased, a new phase (“coherence phase”) arises, without long-range order and with a peculiar symmetry. Both experimental observations and numerical simulations indicate that this phase is linked

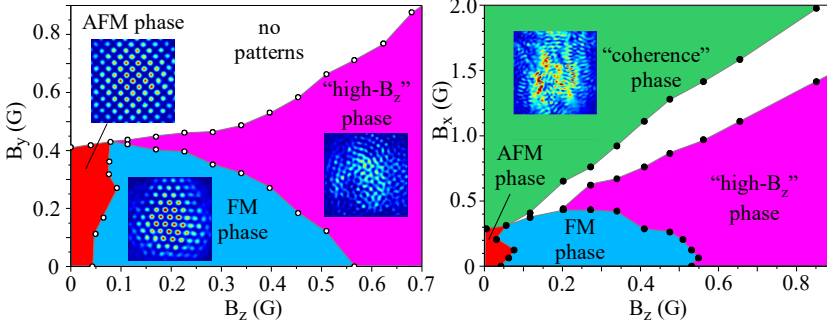


**Fig. 4** Magnetic phase-space of spin patterns.  $B_x$  is the transverse component of the magnetic field parallel to the input polarization,  $B_y$  the transverse component of the magnetic field orthogonal to the input polarization, and  $B_z$  the component of the magnetic field along the pump beam propagation.

to the presence of a spatially-modulated coherence between ground states induced by the  $s^+/s^-$  fields [4].

## References

1. Labeyrie G., Tesio E., Gomes P.M., Oppo G.-L., Firth W.J., Robb G.R.M., Arnold A.S., Kaiser R., and Ackemann T., Optomechanical self-structuring in a cold atomic gas, *Nature Photonics* **8**, 321 (2014).
2. Camara A., Kaiser R., Labeyrie G., Firth W.J., Oppo G.-L., Robb G.R.M., Arnold A.S., and Ackemann T., Optical pattern formation with a 2-level nonlinearity, *Phys. Rev. A* **92**, 013820 (2015).
3. Kresic I., Labeyrie G., Robb G.R.M., Oppo G.-L., Gomes P.M., Griffin, Kaiser R., and Ackemann T., Spontaneous light-mediated magnetism in cold atoms, *Communications Physics* **1**, 33 (2018)
4. Labeyrie G., Kresic I., Robb G.R.M., Oppo G.-L., Kaiser R., and Ackemann T., Magnetic Phase Diagram of Light-mediated Spin Structuring in Cold Atoms, *Optica* **5**, 1322 (2018).



# Eco-evolutionary dynamics in complex ecological communities

Flora Aubree, Vincent Calcagno

**Abstract** Natural ecosystems are complex assemblages composed of many species, interacting together both directly and indirectly, through their environment. The coupled population dynamics (growth, death and reproduction of species) and evolutionary dynamics (Darwinian natural selection acting on species attributes) in such systems can generate a wide range of behaviors. Ecology has long studied how ecosystem complexity should affect their stability and/or productivity, but evolutionary dynamics has received less attention. Using the mathematical framework of adaptive dynamics, we can study how ecological diversity impacts the evolutionary dynamics of ecosystems, and reciprocally, how evolutionary past can alter the diversity-functioning relationship in communities.

## 1 General background

Biodiversity is an important property of ecosystems that impacts several aspects of ecosystem functioning such as productivity [11], stability in the face of perturbations, and robustness to invasive species [7]. It is commonly expected that the more diverse a community, the more productive and robust it is, and there is some evidence that more diverse ecosystems provide more services [7] [8]. Studies of biodiversity-functioning (B-F) relationships are traditionally conducted from an ecological perspective, without explicit consideration of evolutionary processes, in particular Darwinian natural selec-

---

Flora Aubree · Vincent Calcagno  
Université Côte d'Azur, INRA, CNRS, Institut Sophia Agrobiotech, 400 route des Chappes, 06903 Sophia Antipolis, France. e-mail: [vincent.calcagno@inra.fr](mailto:vincent.calcagno@inra.fr)

tion and adaptation. However, it is increasingly clear that evolutionary dynamics play an important role in predicting the structure of natural communities and their response to environmental changes, even on the relatively short timescales relevant to human activities. It is therefore necessary to understand how evolutionary dynamics and ecological dynamics interact and how their interaction determines ecosystem properties. Theoretically, this requires moving from classical dynamical models in which species traits and parameters are treated as constant (or externally forced) to ones in which these parameters are themselves dynamic variables that change under the action of mutation and ecological interactions, and whose changes feedback on the ecological dynamics. Here we will briefly introduce one possible approach to this problem, and we will illustrate two applications of these concepts. The first investigates how the diversity (number of species) in a community impacts its evolutionary stability (possibility of diversification or not), with the finding that diversity often facilitates further diversification. The second explores how the evolutionary history of an ecological community (i.e., evolutionary “young” or “mature”) might change the expected relationships between diversity and ecosystem functioning (productivity, resilience to perturbations and invasions).

## 2 Modeling framework

We consider ecosystems containing a certain number  $s$  of interacting species, each characterized by its population density  $n_i$  and one ecological trait  $x_i$ ,  $i \in (1, s)$ . The ecological trait is taken to represent the ecological strategy of the species and determines its interactions with the environment and with the other species (“ecological niche”). Ecological dynamics are governed by a set of  $s$  ordinary differential equations of the form

$$\frac{dn_i}{dt} = r_i n_i g(n_1, \dots, n_s, x_1, \dots, x_s) \quad i \in (1, s), \quad (1)$$

with  $r_i$  the characteristic timescale of the species (intrinsic growth rate) and  $g$  some growth function.

The growth function is considered to be non-linear but sufficiently smooth, and can otherwise have different forms depending on the type of ecological interactions at play in the community (resource competition, interference, predation, etc.). An archetypal growth function is the generalized Lotka-Volterra model  $1 - \frac{1}{k(x_i)} \sum_{j \in (1, s)} a(x_i, x_j) n_j$ , where  $k(x_i)$  is the “carrying capacity” of species  $i$  and  $a(x_i, x_j)$  is the per-capita interaction coefficient of species  $j$  onto species  $i$ . Most standard scenarios for ecological interactions

can be described with appropriate functional forms for  $k$  and  $a$ , but some cannot fit the Lotka-Volterra form (see Section 4.1). It is assumed that the ecological system (1) eventually reaches a stable node as  $t \rightarrow \infty$ , at which some species shrink out to zero density (“extinct” species) and others equilibrate at equilibrium density  $n_i^*$  (“resident” species).

The above described ecological dynamics are supplemented by a process of evolutionary dynamics, whereby the species trait values  $x$  change through time under the action of Darwinian natural selection. In principle this implies at least adding to (1) a set of  $s$  equations for  $dx_i/dt$ . In practice, we use a slow-fast approximation known as adaptive dynamics [4], that we briefly introduce here. It is assumed that each species produces, at some (low) rate, mutant individuals with slightly deviant trait value  $x_m = x_i + \delta$ , where  $x_i$  is the trait of the parent and  $\delta$  is a random deviate with zero mean and vanishingly small variance. Since mutants are initially very rare they do not have a significant impact on the ecological dynamics of the resident species, and since mutations are infrequent, the resident species have time settle at their equilibrium abundances  $n_i^*$ . If the initial density of a mutant population is  $n_m$ , we define the *invasion fitness* of the mutant as

$$f(x_m) = \lim_{n_m \rightarrow 0} \left( \frac{1}{n_m} \frac{dn_m}{dt} \right), \quad (2)$$

If  $f(x_m) < 0$  the mutant population declines and disappears, whereas if  $f(x_m) > 0$  mutants increase in abundance and settle in the community (“invade”). One advantage of this approach is that fitness naturally emerges from the ecological dynamics specified in (1). Note that fitness is context dependent and depends on the composition of the entire community.

Mutant invasion implies that the whole system may be pushed to a totally different equilibrium. However, since mutants are almost identical to their parental species, mutant invasion generically results in a substitution of the parental species by the mutant population. In these conditions, species traits evolve continuously through time, at a rate proportional to the *selection gradients*, defined as

$$\nabla(x_i) = \left. \frac{df(x_m)}{dx_m} \right|_{x_m=x_i} \quad i \in (1, s), \quad (3)$$

If  $\nabla(x_i) > 0$ , evolution makes the species trait increase through time, if  $\nabla(x_i) < 0$  it makes it decrease.

The process describes gradual directional changes in species traits. Because of the slow-fast approximation, as trait values evolve the system tracks the (moving) ecological equilibrium defined from (1). As evolution proceeds, some species may go to extinction, i.e., the equilibrium may collide

with the boundary of their persistence domain. Another possibility is that some species reach a so-called *singular strategy* at which the selection gradient vanishes. In this case different possibilities exist. One is that the species reaches a fitness maximum, and its trait value thus represents an evolutionary end point (no further change). Another is that the species reaches a fitness minimum, in which case mutants on both sides (or at least on one side in some degenerate cases) can invade. In this case it is possible that mutant invasion does not imply mutant substitution: the mutant population may coexist with the resident population, and the two populations may subsequently diverge in trait space, thus effectively splitting the initial parental species into two daughter lineages. After a branching event, we need to add one equation to (1). This type of singular strategies are called *branching points*, and the process of branching is regarded as a model of species formation through ecological interactions (ecological diversification). It is possible to classify the different types of evolutionary dynamics around a singular strategy using the two derivatives  $d^2 f(x_m)/dx_m^2$  and  $d\nabla(x_i)/dx_i$ .

In the following applications we will use a set of different ecological models (particular instances of (1)) to avoid model-specific conclusions.

### 3 How diversity impacts evolutionary diversification

#### 3.1 Context and methods

It is well-understood, theoretically, that the more species in an ecological system, the less likely it should be for the system to settle at a dynamically stable equilibrium, and the less stable the equilibrium, if any, would be. A seminal paper by May [14], using the theory of random matrices, provided a general argument for this and elicited a long and fruitful debate on the relationships between species diversity and different types of ecological stability. The debate remained in the field of ecology though, and evolutionary stability, i.e., the tendency of evolutionary attractors to be fitness maxima (stable) or fitness minima (unstable), and thus the possibility of diversification, was disregarded. In parallel, evolutionary biology proposed the controversial hypothesis that species diversity could stimulate further diversification (the “diversity-begets-diversity” hypothesis), but this was not investigated using ecological theory.

We thus analyzed whether an ecological system of  $s$  species, as modeled in section 2, is more or less likely to be evolutionary unstable, i.e., to evolve toward branching points rather than fitness maxima, as the number of species  $s$  increases. To this end we simulated the evolutionary dynam-

ics of ecological communities, starting from different initial levels of initial diversity, from monomorphic ( $s = 1$ ) to diverse ( $s = 5$ ). We did this using three contrasted forms of ecological interactions, modeled as three different forms of the growth function  $g$ , all of the Lotka-Volterra family: symmetric competition of resources, asymmetric competition with interference, and a competition-colonization trade-off scenario, where better competitors are poorer at colonizing empty patches [1,12]. For each model, we systematically varied two key parameters controlling the modalities of ecological interactions [3].

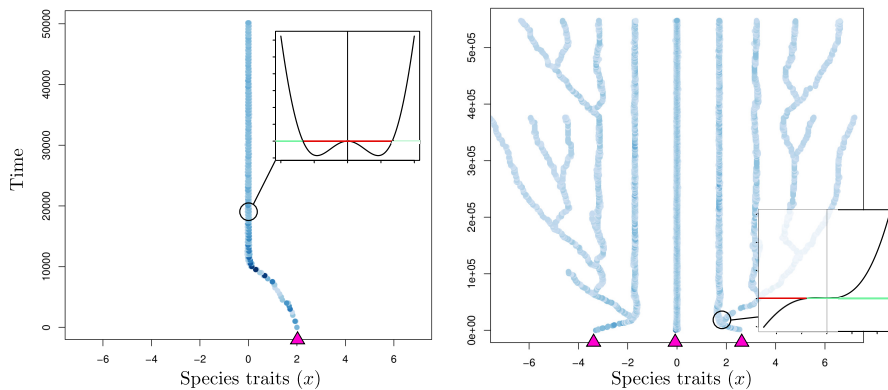


**Fig. 1** Diversity triggers diversification. Two example simulations are shown. Starting from one initial species, a fitness maximum is attained and no further evolution occurs (*left*). For exactly the same parameters, bringing in an initial diversity of three species unlocks the possibility of adaptive diversification and repeated evolutionary branchings occur and diversity explodes (*right*). Figure from [3].

### 3.2 Results

We found that for many parameter sets, adaptive diversification was impossible when starting from one species (i.e., evolutionary trajectories halted at fitness maxima) but became possible after some initial level of diversity was brought into the system (Fig. 1). For a given parameter set, in all three models, there generally existed a minimum level of diversity above which evolutionary branching became possible. In other words, increasing ecological diversity may unlock the possibility of further adaptive diversification, in a form of auto-catalysis. By studying the curvature of the fitness func-

tion around the evolutionary singularities ( $d^2f(x_m)/dx_m^2$ ), and how it varies as  $s$  increases, we could identify three components of natural selection that explained the evolutionary bifurcations (i.e., loss of evolutionary stability). From the three models we observed two general mechanisms explaining the positive effect of diversity on diversification, one operating mostly at low diversity levels and the other at higher diversity levels [3].

It is usually thought that a positive effect of diversity on diversification necessitates specific processes such as niche construction, cross-feeding or ecological facilitation. Our results indicate that the same standard ecological principles that predict a negative effect of diversity on diversification, can just as well predict a diversification-promoting effect of diversity. This might provide an explanation to patterns observed at different scales, such as the delayed onset of lizard adaptive radiations on some islands, or recent findings that diversification correlates positively with initial diversity in experimental microbial communities [3]. Importantly, they suggest that the loss of ecological diversity may drive ecosystems below the threshold level for diversification, compromising the recovery of diversity, even in the long term.

## 4 How evolutionary history impacts the diversity-functioning relationship

### 4.1 Context and methods

Studies of biodiversity-functioning (B-F) relationships are traditionally conducted from an ecological perspective, without explicit consideration of evolutionary processes. Yet, it is clear that by altering the trait distribution and thus species interactions, evolutionary history (intended here as the history of coevolution of species within an ecosystem) may have a non-negligible role in determining the existence, magnitude and shape of B-F relationships. Several studies have already been undertaken in that direction, looking at the impact of fast evolution on ecosystem properties [6], of environment changes on robustness [16] or of the species coevolution on ecological stabilities [10].

Here we propose to study whether B-F relationships could depend on the evolutionary history of ecosystems. Specifically, we will generate two types of communities: **random** (“young”) and **coevolved** (“mature”). In random communities species traits are drawn independently from an entropy-maximizing distribution. In coevolved communities, trait values are set at a (co-)evolutionary equilibrium, finding trait combinations that cancel all se-

lection gradients (eq.3) and are local attractors of evolutionary trajectories. This permits one to contrast communities with no evolutionary history at all with maximally coevolved (mature) ones. We did this for different levels of species richness  $s$  (1-10) and under five scenarios of ecological interactions (eq.3) representative of known species coexistence mechanisms. In addition to the three scenarios used in section 3 we considered two non-Lotka-Volterra scenarii: the tolerance-fecundity trade-off scenario [15] and the size-structured trophic chain scenario [9]. Three types of B-F relationships are then quantified: (a) **Total productivity** defined as the sum over species of the positive contributions to net growth rate (eq.1) ; (b) **Temporal stability** defined here as the asymptotic resilience (closest to zero eigenvalue of the Jacobian matrix of (1)); and (c) **Robustness to invasion** is assessed by two metrics: the probability of establishment of invasive species with random trait  $x_e$  (invasion resistance), and, for successful invasions, the expected number of resident species that are driven to extinction (invasion tolerance). For a range of parameter values, the B-F relationships were systematically compared between random and co-evolved communities.

## 4.2 Results

B-F relationships were affected by evolutionary history in all five scenarii. In random communities, productivity, as expected, increased with diversity in most cases, with the notable exception of the CC trade-off scenario (Figure 2). A history of coevolution had quantitative and qualitative effects on the diversity-productivity (D-P) relationships. Quantitatively, D-P relationships had smaller amplitudes in mature communities compared to random ones, to the point of being almost undetectable in the trophic chain scenario, and they have a much more concave shape. Qualitatively, coevolution can reverse the slope of the D-P relationship, as observed in the CC trade-off scenario. Overall, evolutionary history strongly affects the expected D-P relationship, with a general tendency of D-P relationships to be shallower, and more consistently positive in mature communities compared to random communities.

Asymptotic resilience decreased with diversity in all scenarii, as expected in such models, and irrespective of evolutionary history. In the CC, TF and trophic chain interactions, there was no appreciable difference in the shape of the diversity-stability (D-S) relationships. However, the shape change induced by the past evolutionary history in the niche and body size scenarii was notable. It changed from convex to sigmoid, respectively, in mature and random communities, and led to more stability for mature communities at

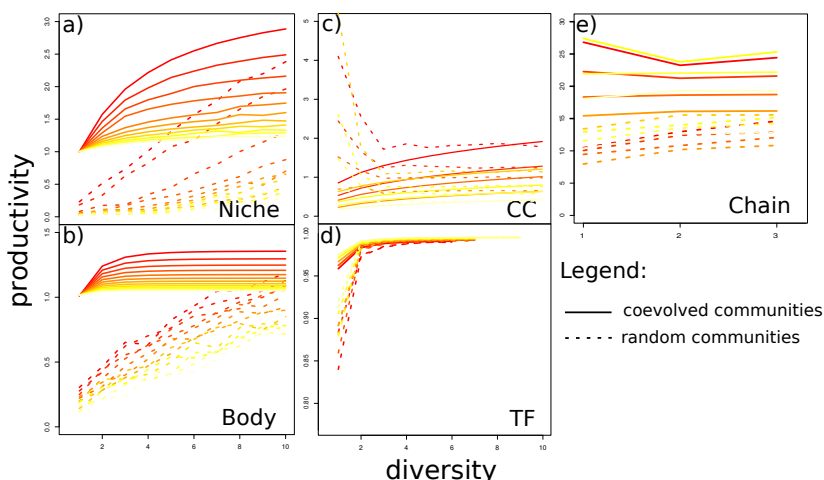


**Fig. 2** Productivity for the (a) *niche*, (b) *body size*, (c) *CC trade-off*, (d) *TF trade-off* and (e) *trophic chain* scenarii. Colors stand for the different model parameters varied.

high diversity. It resulted that the fast decrease for mature communities at low diversity slowed down at higher diversity, while the contrary occurred for random communities.

Invasion resistance was not drastically influenced by past evolutionary history: the invasion probability, which was decreasing with diversity as expected, was only slightly smaller in coevolved communities (except in the CC scenario where it was slightly higher). By contrast, for the invasion tolerance results clearly showed that coevolved communities were much less perturbed by invasive species than random ones: almost no species disappeared for all species richness explored, and the invasive species remained at a very low abundance compared to resident species. To the contrary, random communities lost a lot of species when invaded and the invasive species was more abundant. In sum, past evolutionary history did not impact clearly the probability of invasion, but changed considerably the response to an effective invasion.

To conclude, all scenarii of ecological interaction and all the observed functional properties were sensitive to the past evolutionary history. Natural unperturbed ecosystems and young (or recently perturbed) ecosystems did not behave and react the same. Those studies confirm that evolutionary history should be a parameter to consider while studying ecosystem functioning.

## 5 Conclusion

As is visible in the examples presented here, ecological and evolutionary dynamics have reciprocal interactions, and it may be insufficient to study them individually. Adaptive dynamics provides a useful method to incorporate adaptive evolution into ecological models and expand our theoretical understanding the dynamics of ecosystems. The approaches presented here can be expanded to relax some critical assumptions, such as the rarity of mutations and slow-fast approximation [2], the absence of spatial structure [13], the scalarity of species traits [5] and beyond.

## References

1. Calcagno, V., Mouquet, N., Jarne, P., and David, P.: Coexistence in a metacommunity: the competition-colonization trade-off is not dead. *Ecology Letters*, **9**(8), 897-907 (2006)
2. Calcagno, V., Dubosclard, M. and de Mazancourt, C.: Rapid exploiter-victim coevolution: the race is not always to the swift. *The American Naturalist*, **176**(2), 198-211 (2010)
3. Calcagno, V., Jarne, P., Loreau, M., Mouquet, N. and David, P.: Diversity spurs diversification in ecological communities. *Nature Communications*. **18** (2017)
4. Dercole, F. and Rinaldi, S.: Analysis of evolutionary processes: the adaptive dynamics approach and its applications: the adaptive dynamics approach and its applications. Princeton University Press. (2008)
5. Doebeli, M., and Ispolatov, I.: Complexity and diversity. *Science*, **328**(5977), 494-497 (2010)
6. Fussmann, G. F., Loreau, M. and Abrams, P. A.: Eco-evolutionary dynamics of communities and ecosystems. *Functional Ecology*, **21**: 465-477 (2007)
7. Hooper, D. U., Chapin, F. S., Ewel, J. J., Hector, A., Inchausti, P., Lavorel, S., Lawton, J. H., Lodge, D. M., Loreau, M., Naeem, S., Schmid, B., Setälä, H., Symstad, A. J., Vandermeer, J. and Wardle, D. A.: Effects of biodiversity on ecosystem functioning: a consensus of current knowledge. *Ecological Monographs*, **75**: 3-35 (2005)
8. Isbell, F., Calcagno, V., Hector, A., Connolly, J., Harpole, W. S., Reich, P. B., Scherer-Lorenzen, M., Schmid, B., Tilman, D., van Ruijven, J., Weigelt, A., Wilsey, B. J., Zavaleta, E. S. & Loreau, M.: High plant diversity is needed to maintain ecosystem services *Nature*. Nature Publishing Group, **477**, 199- (2011)
9. Loeuille, N. & Loreau, M.: Evolutionary emergence of size-structured food webs. *National Academy of Sciences*, **102**, 5761-5766 (2005)
10. Loeuille, N.: Influence of evolution on the stability of ecological communities. *Ecology Letters*, **13**: 1536- (2010)
11. Loreau, M., Naeem, S., Inchausti, P., Bengtsson, J., Grime, J. P., Hector, A., Hooper, D. U., Huston, M. A., Raffaelli, D., Schmid, B., Tilman, D. & Wardle, D. A.: Biodiversity and Ecosystem Functioning: Current Knowledge and Future Challenges *Science*. American Association for the Advancement of Science, **294**, 804-808 (2001)

12. Livingston, G., Matias, M., Calcagno, V., Barbera, C., Combe, M., Leibold, M. A., and Mouquet, N.: Competition-colonization dynamics in experimental bacterial meta-communities. *Nature communications*, **3**, 1234 (2012)
13. Massol, F., Calcagno, V., and Massol, J.: The metapopulation fitness criterion: proof and perspectives. *Theoretical population biology*, **75**(2-3), 183-200 (2009)
14. May, R. M.: Will a large complex system be stable?. *Nature*, **238** (5364), 413 (1972)
15. Muller-Landau, H. C.: The tolerancetextendashfecundity trade-off and the maintenance of diversity in seed size. *National Academy of Sciences*, **107**, 4242-4247 (2010)
16. Strona, G. & Lafferty, K. D.: Environmental change makes robust ecological networks fragile. *Nature Communications*, **7**, 12462- (2016)

# The Nice Cube (Nice<sup>3</sup>) nanosatellite project

F. Millour, S. Ottogalli, M. Maamri, A. Stibbe, F. Ferrero, L. Rolland, S. Rebeyrolle, A. Marcotto, K. Agabi, M. Beaulieu, M. Benabdesselam, J.-B. Caillau, F. Cauneau, L. Deneire, F. Mady, D. Mary, A. Memin, G. Metris, J.-B. Pomet, O. Preis, R. Staraj, E. Ait Lachgar, D. Baltazar, G. Bao, M. Deroo, B. Gieudes, M. Jiang, T. Livio de Miranda Pinto Filho, M. Languery, O. Petiot, A. Thevenon

**Abstract** CubeSats are tiny satellites with increasing capabilities. They have been used for more than a decade by universities to train students on space technologies, in a hands-on project aiming at building, launching and operating a real satellite. Still today, one shortcoming of CubeSats is their poor ability to transmit large amounts of data to the ground. A possible way to overcome this limitation relies on optical communications. Université Côte d’Azur is studying the feasibility of a students’ CubeSat whose main goal is to transmit data with an optical link to the ground at the moderate rate of 1 kb/s (or better). In this paper, we will present the current state of the project and its future developments.

## 1 Introduction, mission objectives

CubeSats are small satellites (“SmallSats” class) made of 10 cm-side cubes that form a “unit” (or a 1U CubeSat). A large number of units can be combined, although the bulk of current developments range from 1U (e.g. Robusta1B), 2U (Spacecube, X-cubesat), up to 3U (e.g. Picasat, Eyesat, NIMPH

---

All authors work at  
Université Côte d’Azur (see acknowledgements for details), e-mail: [fmillour@oca.eu](mailto:fmillour@oca.eu).

[1]). However today, we can start to see 12U CubeSat projects under development by several universities (for example the Grenoble/Toulouse ATISE project [2]). These SmallSats are getting more and more attention from the universities because they offer the possibility to teach space-related techniques to students on a hands-on experiment, with a budget that can be reached by a medium-size university.

CubeSats also get more and more attention from companies (e.g., Nexeya<sup>1</sup>, Planet Labs<sup>2</sup>) because they offer fast development cycles for new technologies with reduced costs compared to more “traditional” satellites. The drawbacks are an extremely small payload volume and mass, a lack of redundancy, and a perfectible reliability that can be mitigated by payload miniaturization and the use of satellite constellations, or “flocks” [3].

The consequence of this tiny size is the limited data transmission capacities that can be integrated into a CubeSat: most of the radio transmitters (67% of the 1630 radio emitter-receivers included in CubeSats<sup>3</sup>) use the amateur radio frequencies to transmit data (UHF – 437 MHz & VHF – 146 MHz), a few (6%) use S-band (2.2-3.4 GHz), some (25%) use X-band (10 GHz), and the remaining 2% use other frequencies. The use of radio-frequencies to transmit data from the satellite to the ground has some drawbacks, like the crowding of used frequencies (potentially producing interference), or the poor directivity of the radio beam (enabling hacking of the data reception), not to say the poor data rate of UHF and VHF (about 1 kb/s). In addition, considering the small available volume in the satellite, the UHF/VHF antennas have to be mechanically deployed, which is adding a risk to the success of the mission. Mitigating this risk by finding antenna schemes robust to deployment failure is an interesting track to look for.

To alleviate this poor data rate, an optical transmission chain (light source – beam launcher – telescope – photodiode) can be considered instead of a radiofrequency chain (transmitter – TX antenna – RX antenna – receiver). An optical transmission chain has some advantages over a radio chain: it has a high directivity, making it difficult to intercept, there is no need to allocate a frequency, and there is a potential to have a high-speed data link (several hundred of Mb/s [4])

---

<sup>1</sup> <https://www.nexeyaonline.com/small-sats-satellite-platforms>

<sup>2</sup> <https://www.planet.com>

<sup>3</sup> according to <http://www.nanosats.eu/index.html#figures>, consulted in June 2018

## 2 Mission description

The main goal of the Nice cube mission (Nice<sup>3</sup>) is to establish a data optical link between the satellite and the ground, while keeping it in a 1U CubeSat format.

The second goal of the mission is to demonstrate a high-enough transmission rate (higher than 1 Kb/s).

All the characteristics of the mission are derived from these two key aspects. Several CubeSat missions have already had a similar goal to produce a data optical link. Some (e.g., FitSat [5] or Equisat<sup>4</sup>) use arrays of LEDs to render the CubeSat visible from Earth with a small telescope or even the naked eye. They may communicate with the ground via Morse code [6]. Other missions (OCSD [4], Node [7]) embed a high-power LASER that is precisely pointed at the ground station. Finally, the C3PO [8,9] project, and other developments at the US Navy [10,11] have the objective of developing the Multiple Quantum Well technology (MQW) to produce a retro-reflecting modulator that can be embedded into a CubeSat. MQW technology allows one to establish an asymmetric optical link with a very high bandwidth.

For Nice<sup>3</sup>, a first assessment of technologies and available resources led us to favor retro-reflecting solutions that we will present in this paper. Other options will remain possible if retro-reflecting solutions do not converge fast-enough to a mature state (i.e., both space and ground segments are working).

## 3 Mission constraints

The first and main constraint of the mission is that it must fit into a 1U CubeSat. This constraint limits the available electrical power onboard and the payload space inside the satellite.

The second constraint, resulting from the main goal of the mission, is to establish a *successful* optical link between the satellite and the ground.

Remembering that the light source is aimed at the satellite from the ground (LASER), this means that the satellite must always present a face with the modulating retro-reflector to the ground station when flying over it, with a precision to be determined (but at least better than 10°). This can be achieved either by covering each 6 cube face with a retro-reflector (as in the design presented in Fig. 3), or using a passive or an active attitude control system that we plan to study in details during the project. At the same

---

<sup>4</sup> <https://brownspace.org>

time, the satellite must stay in orbit long enough to fulfill the main mission objectives, and it must be close enough and have a large enough reflection surface to establish the optical link with sufficient margins with the ground station.

The third constraint is the compliance to the LOS (Loi des Opérations Spatiales<sup>5</sup>), i.e., the satellite must de-orbit back to Earth in less than 25 years.

These three constraints are somewhat contradictory and we will find the optimum values for the orbit altitude in the coming months. The second and last constraints are being tested right now with the STELA<sup>6</sup> tool from CNES (see Table. 1), and an orbit ranging from 500 to 650 km seem to be relevant for this mission in order to both comply with the LOS and a typical mission duration of 1 year (in order to allow us some time to set up the satellite in flight, verify its good health, acquire the satellite with the optical ground station, and then perform the data transmission test itself).

**Table 1** Set of possible orbits for the CubeSat mission that satisfy the LOS. A first range of possible orbits for Nice<sup>3</sup> is between 500 and 650 km with a small eccentricity.

Altitude	400	500	600	650	700	800	900	1100	1200
Excentricité									
0	0,44	2,39	11,39	23,55	> 25 ans				
0,005	0,42	2,31	11,05	22,97	> 25 ans				
0,01	0,37	2,02	10,01	20,99	> 25 ans				
0,05	0	0,02	0,48	1,35	3,4	17,59	> 25 ans	> 25 ans	> 25 ans
0,1	0	0	0	0	0	0	0,13	11,11	> 25 ans

#### 4 First sets of definitions of the mission

The satellite mission contains both a ground station and command center, and the satellite itself. The satellite can be decomposed into a payload and a platform.

<sup>5</sup> <https://www.legifrance.gouv.fr/affichTexte.do?cidTexte=JORFTEXT000018931380>

<sup>6</sup> available at <https://logiciels.cnes.fr/fr/content/stela>

## 4.1 Description of the ground segment

The ground segment will be composed of 3 items: A command and control center, a radio ground station (probably UHF/VHF) for housekeeping telemetry, satellite remote control, and satellite position downlink, and the optical ground station itself, made of a fast-steering telescope and a lasercom setup.

The UHF/VHF ground station will be mounted with off-the-shelf hardware to provide the necessary two-way communications with the satellite. This main radio station will be designed as the project advances.

In the meantime, we started building a UHF SATellite Networked Open Ground Station (SATNOGS)<sup>7</sup> for demonstration purposes with the students of the Polytech Nice-Sophia Antipolis engineering school. The current state of this station is the following: some of the mechanical parts were printed on a 3D printer and assembled, the other parts of the assembly (trusses) being cut from off-the-shelf components. Then, the command electronics were tested and a PCB was designed to integrate an arduino, stepper motors control, endstops control, current sensor and temperature sensors. A first command code was also produced by the students (Fig. 1, left). On the other hand, a Yagi-Uda antenna tuned to 450 MHz was designed and tested (Fig. 1, right). The next steps are to integrate all the necessary parts (mount, antenna, SDR, arduino, raspberry pi), focus on a 437 MHz antenna, add a GPS, inertial measurement units, make it battery-operated, to provide a transportable ground station that can be easily demonstrated on conferences or shows.

To give an idea of the dimensions of the optical ground station, a first assessment of the light propagation was made, considering a 1 W LASER at 1550 nm wavelength, atmosphere disturbance (seeing) of 3", light diffraction, atmosphere absorption, etc. This assessment led us to consider a corner cube assembly with a 3 cm aperture on the satellite, a 20 cm aperture on the beam launching device (upwards LASER), and a 1.5 m telescope size for the reception of the reflected signal (downwards-reflected LASER). A typical signal-to-noise ratio of 6 (i.e.,  $\approx 40$  photons per cycle) may be achieved for a 100 kHz light modulation, giving spacious margins to achieve a data rate of 1 kb/s.

Note here that the corner cube return beam is aimed back directly, whatever the angle the cube makes relative to the ground station (as long as it is in the 10° misalignment range mentioned above).

All these figures need to be confirmed, but they give a first idea of the typical features of the mission. The MeO 1.5 m LASER telemetry telescope, located in the Calern plateau less than 50 km from Nice, and operated by the

---

<sup>7</sup> <https://satnogs.org>

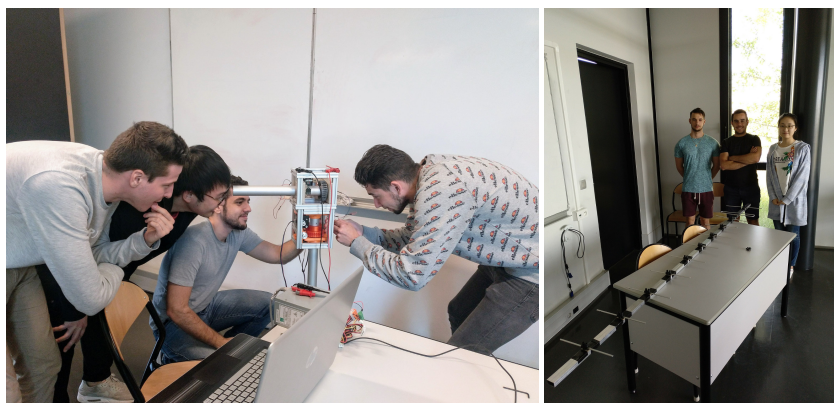


**Fig. 1** Current state of the SATNOGS ground station at Polytech Nice engineering school. On the left side, one can see a group of students working on the control electronics of the mount, and on the right side, one can see the Yagi-Uda antenna being designed by another group of students.

Côte d'Azur Observatory, is a prime candidate to serve as the optical ground station for Nice<sup>3</sup>.

## ***4.2 Description of the platform***

The platform will be comprised of:

- a mechanical structure holding the necessary electronics and the payload,
- an electrical procurement system composed of:
  - solar generators (solar panels),
  - energy storage (rechargeable batteries),
  - a power supply unit (PSU),
- an on-board computer (OBC)
- a radio-communications system composed of:
  - a radio emitter-receiver,
  - an antenna,
- and finally a thermal regulation system.

The platform may be built using commercial off-the-shelf elements from a well-known supplier, but we also investigate the possibility to collaborate

with another CSU that developed all these elements in-house, e.g., the Montpellier University CSU.

### 4.3 Description of the payload

The Nice<sup>3</sup> payload is composed of a retro-reflector, allowing the satellite to send back an optical beam to the emitter on the ground, and an optical modulator, which will encode the data meant to be sent from the satellite to the ground. The optical modulator is the centerpiece of the project, and we are investigating the possible options to achieve the necessary bandwidth of the mission ( $\geq 1$  Kb/s).

Retro-reflectors can come in several forms: prismatic retro-reflector (corner cubes); hollow corner cubes; ball lenses; cat's eyes; and finally, telecentric reflectors (see Figure 2). We are building an optical bench to measure characteristics of these different types of retro-reflectors, especially the above-mentioned  $10^\circ$  tolerance to misalignment. Once they have been characterized, we will select one type of reflector for the mission, based on their acceptance angle, overall reflectivity, optical quality, etc.

We consider that a retro-reflector with an aperture larger than 3 cm cannot fit in the satellite, so this is our maximum size.

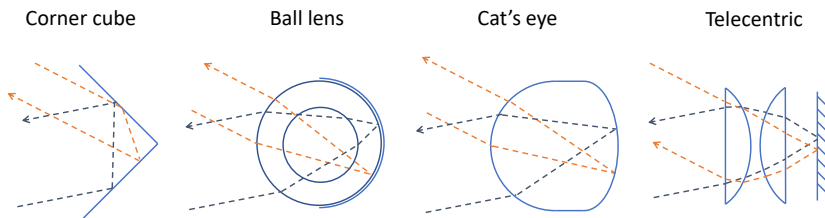


Fig. 2 Different types of retro-reflectors that will be considered for the mission.

Optical modulators, which act here as optical shutters, can come in several flavors too: Liquid crystal devices, being in transmission (LCD shutter from Thorlabs) or in reflection (LCOS from Hamamatsu); Texas Instrument's Digital Light Processor (DLP); Boston Micromachine's modulating reflector (MRR); tip/tilt mirrors mounted on piezoelectric actuators (made by Cedrat Technologies and flown in PicSat); and finally, Multiple Quantum Well tech-

nology (MQW) developed by Arianegroup and the US Navy. These different devices have different response times that are listed in Table 2

**Table 2** Optical modulators considered in the project and their typical characteristics.

Modulator	Active area	Max. frequency	Power	Mass	space-ready?
LCD	20 x 20 mm	2 kHz	300 mW	100 g incl. mount	No
LCOS	16 x 12 mm	120 Hz	35 W <sup>8</sup>	-	No
DLP	10 x 6 mm	4KHz	91 mW	-	No
MRR	∅14 mm	200 kHz	10 $\mu$ W	300 g incl. mount	No
Piezo actuator	-	10 kHz	0.75 W	12 g without mirror	Yes
MQW	-	$\geq$ 10 MHz	-	-	-

We have three possible optical configurations depending on the type of modulator and the type of retro-reflector chosen for the mission.

Depending on choices made on the way, the mission is designed (attitude control vs. no attitude control), we will have two different satellite configurations: one without attitude control and 6 modulating retro-reflectors (1 per cube face), and one with an attitude control and just 1 retro-reflector.

The payload may also include a GNSS receiver (e.g. GPS or GALILEO) to locate the satellite in real time by sending its position to the ground via a radio link, and a high-power LED in order to locate the satellite even when it is not illuminated by the Sun.

Based on these elements, we designed a first version of the Nice<sup>3</sup> satellite, using only off-the-shelf elements, and hollow corner cubes (see Fig. 3).

In this design, the light modulators are embedded in one of the corner cube faces. No attitude control was considered for this first design, leading us to place one corner cube on each of the satellite face. We placed an additional generic PC104 electronics board on the satellite stack to figure the modulators control electronics. We also placed a GNSS receiver and its antenna, in order to send the satellite position to the ground via radio link.

Drilling a hole on each satellite face to let the corner cube go through lead to the necessity to remove one solar cell from the solar panels. The consequent deficit of power (0.5 W instead of 1 W typical) may be mitigated by using solar cells with a different shape, or deployable solar generators.

In this preliminary phase, the integration of a radiolink based on Low-Power Wide Area Network (LP-WAN) has been also investigated. A wireless link over 702km has been already demonstrated at 868MHz using a sounding balloon and LoRa technology [12]. Several geometries have been proposed for CubeSat UHF radio links, including Dipole, Yagi, helical or parabolic structures. All these solutions require mechanical deployment to enable the RF communication, which can be risky. We involved students

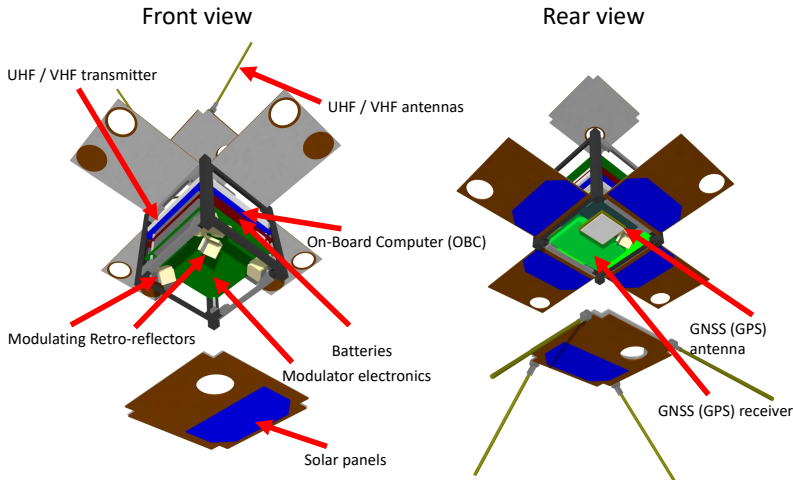


**Fig. 3** Preliminary design of a possible satellite fulfilling several aspects of the mission.

from Polytech Nice Sophia Antipolis to design a custom antenna based on a microstrip patch using one face of the CubeSat, and with four deployable panels. This antenna was manufactured by the students (see Fig. 4) and characterized in a Starlab station. A realized peak gain of 5.4 dBi was achieved. This solution, using a patch antenna, is mitigating the mechanical deployment risk, as a gain of already 4 dBi will be obtained in case of deployment failure. This  $\approx 900$  MHz antenna is a first step. The next step will include the design of an antenna in the radio amateur bands.

## 5 Conclusion

We are about to finish the phase 0 of the Nice<sup>3</sup> CubeSat mission. During these first 6 months, students worked on the project and made significant progress in our understanding of the context and difficulties of building a satellite. We have today a set of first boundaries for the satellite mission. This will enable us to progress further in the mission specifications in the coming months.

Students working on this project come from many backgrounds. They have come from university master's programs, like MAUCA, but also from engineering schools, like Polytech Nice Sophia Antipolis, and of course from other training programs, like optics BTS. The acknowledgments below list

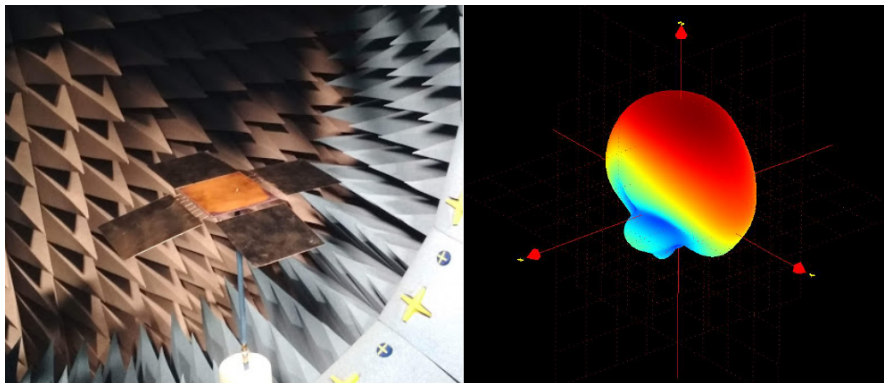


**Fig. 4** Left: microstrip patch deployable antenna prototype on the characterization bench. Right: measured 3D radiation pattern at 900MHz of this antenna.

further the training programs that closely follow the project. Making a satellite project with students is an exciting experience and we are preparing for the end of the phase 0 with enthusiasm.

### *Acknowledgments*

*This project is supported by the Université Côte d'Azur (UCA), the Côte d'Azur Observatory (OCA) and the Centre National des Études Spatiales (CNES).*

*The Centre Spatial Universitaire (CSU) of the Université Côte d'Azur (UCA) offers students practical training as part of courses from the Astrophysics master's program (MAUCA) or the Geophysics master's course (master 3G) of UCA, from the Mines Paristech and Polytech Nice-Sophia Antipolis engineering schools, as well as professional experience in research laboratories and institutes: Lagrange, Geoazur, LEAT, I3S, CEMEF, Inphyni and INRIA.*

*The authors would like to thank the joint laboratory between Université Côte d'Azur, CNRS and Orange, "Centre de Recherche Mutualisé pour les Antennes" (CREMANT), for its support in the microstrip patch antenna characterization.*

### **References**

1. Arnaud Fernandez, Amadou Gadio, F Destic, Julien Sommer, A Rissons, Christophe Viallon, Nicolas Nolhier, Olivier Llopis, Éric Tournier, Jean-Guy Tartarin, S Lizy-

- Destrez, J Chaix, and O Gilard. The NIMPH Project. In *7th CubeSat Symposium*, Liège, Belgium, September 2015. von Karman Institute for Fluid Dynamics, University of Liege.
2. E. Le Coarer, M. Barthelemy, A. Vialatte, M. Prugniaux, G. Bourdarot, T. Sequies, P. Monsinjon, R. Puget, and N. Guerneau. ATISE: a miniature Fourier-transform spectro-imaging concept for surveying auroras and airglow monitoring from a 6/12U cubesat. In *ICSO 2016*, BIARRITZ, France, October 2016.
  3. Christopher Boshuizen, James Mason, Pete Klupar, and Shannon Spanhake. Results from the planet labs flock constellation. 2014.
  4. Siegfried Janson and Richard Welle. The nasa optical communication and sensor demonstration program. 2013.
  5. Takushi Tanaka, Yoshiyuki Kawamura, and Takakazu Tanaka. Overview and operations of cubesat fitsat-1 (niwaka). In *Recent Advances in Space Technologies (RAST), 2013 6th International Conference on*, pages 887–892. IEEE, 2013.
  6. Takushi Tanaka, Yoshiyuki Kawamura, and Takakazu Tanaka. Development and operations of nano-satellite fitsat-1 (niwaka). *Acta Astronautica*, 107:112 – 129, 2015.
  7. Emily Clements, Raichelle Aniceto, Derek Barnes, David Caplan, James Clark, Iñigo del Portillo, Christian Haughwout, Maxim Khatsenko, Ryan Kingsbury, Myron Lee, et al. Nanosatellite optical downlink experiment: design, simulation, and prototyping. *Optical Engineering*, 55(11):111610, 2016.
  8. C Quintana, Q Wang, D Jakonis, X Piao, G Erry, D Platt, Y Thueux, A Gomez, G Faulkner, H Chun, et al. High speed electro-absorption modulator for long range retroreflective free space optics. *IEEE Photonics Technology Letters*, 29(9):707–710, 2016.
  9. Benoît d’Humières, Bruno Esmiller, Yann Gouy, Emilie Steck, Crisanto Quintana, Graham Faulkner, Dominic O’Brien, Fabian Sproll, Paul Wagner, Daniel Hampf, et al. The c3po project: A laser communication system concept for small satellites. In *Free-Space Laser Communication and Atmospheric Propagation XXIX*, volume 10096, page 1009611. International Society for Optics and Photonics, 2017.
  10. William S Rabinovich, Peter G Goetz, Rita Mahon, Lee Swingen, James Murphy, G Charmaine Gilbreath, Steven C Binari, and Eugene Waluschka. Performance of cat’s eye modulating retro-reflectors for free-space optical communications. In *Free-Space Laser Communications IV*, volume 5550, pages 104–115. International Society for Optics and Photonics, 2004.
  11. G Goetz Peter, S Rabinovich William, Rita Mahon, L Murphy James, S Ferraro Mike, R Suite Michele, R Smith Walter, B Xu Ben, R Burris Harris, I Moore Christopher, et al. Modulating retro-reflector lasercom systems at the naval research laboratory. In *Military Communications Conference, 2010-Milcom 2010*, pages 1601–1606. IEEE, 2010.
  12. Thomas Telkamp and Laurens Slats. <https://www.thethingsnetwork.org/article/ground-breaking-world-record-lorawan-packet-received-at-702-km-436-miles-distance>Ground breaking world record! LoRaWAN packet received at 702 km (436 miles) distance. 2017.



## Modelling complex systems in Archaeology: general issues and first insights from the ModelAnSet project

Frédérique Bertoucello, Marie-Jeanne Ouriachi, Célia  
Da Costa Pereira, Andrea Tettamanzi, Louise  
Purdue, Daniel Contreras, Dennis Fox, Nobuyuki  
Hanaki, Rami Ajroud, Jérémy Lefebvre

---

Frédérique Bertoucello  
Université Côte d'Azur, CNRS, CEPAM - UMR 7264 CNRS, Nice. e-mail: [frederique.  
bertoucello@cepam.cnrs.fr](mailto:frederique.bertoucello@cepam.cnrs.fr)

Marie-Jeanne Ouriachi  
Université Côte d'Azur, CNRS, CEPAM - UMR 7264 CNRS, Nice

Célia Da Costa Pereira  
Université Côte d'Azur, CNRS, I3S - UMR 7271 CNRS, Nice

Andrea Tettamanzi  
Université Côte d'Azur, CNRS, I3S - UMR 7271 CNRS, Nice

Louise Purdue  
Université Côte d'Azur, CNRS, CEPAM - UMR 7264 CNRS, Nice

Daniel Contreras  
SWCA Environmental Consultants, Salt Lake City, UT, USA; IMBE, Aix-Marseille Univer-  
sité, Aix-en-Provence

Dennis Fox  
Université Côte d'Azur, Université Nice Sophia Antipolis, ESPACE - UMR 7300 CNRS,  
Nice

Nobuyuki Hanaki  
Université Côte d'Azur, Université Nice Sophia Antipolis, GREDEG - UMR 7321 CNRS,  
Nice

Rami Ajroud  
Université Côte d'Azur, CNRS, I3S - UMR 7271 CNRS, Nice

**Abstract** Complexity theory provides useful concepts for archaeological issues related to the understanding of past societies and their environment. More specifically, Agent-Based Modelling is a relevant tool to explore scenarios and to test hypotheses about the impacts of complex socio-environmental interactions on the transformations of ancient settlement systems evident in archaeological records. After a short historiography of complex systems modelling in Archaeology, this paper focus on the mains issues of archaeological simulation models. As a case study, we briefly present the model under development within the ModelAnSet project supported by UCA<sup>JEDI</sup> Complex Systems Academy of Excellence. Agent-Based Modelling is used to explore the respective impacts of environmental and social factors on the settlement pattern and dynamics during the Roman period in South-Eastern France.

## 1 Archaeology and Complex Systems

Interest for system and complexity theories is not new in Archaeology: it follows the deep renewal of the concepts and methodologies of the discipline brought by the New Archaeology movement, which developed at the end of the 1960's in the US and England [1–3]. The New Archaeology provides a quantitative and systemic approach, where past societies are considered as systems formed by many interacting components. Instead of explaining cultural change and the transformation of societies by external influence, as it was usual in classical Archaeology, New Archaeology considered that change results from the interactions between the components of the system. As a processualist movement, the New Archaeology focusses on dynamics and seeks to identify regularities on archaeological records, in order to define general rules in the functioning of past societies.

During the 1980's the interest for complex system approaches slackened under the influence of the post-processualists critics against the New Archaeology, pointing out especially its lack of attention to the context (historical, social, environmental, etc.) in the particular evolutions of societies and to the role of the individuals as active agents of these evolutions.

The renewal came at the end of the 1990's under the influence of both conceptual and technical developments [4–7]. Complex Adaptive Systems, as a strand of complexity theory, provided relevant concepts to study long-term social changes [8], while increasing computing capacity and the de-

velopment of platforms for Cellular Automata and Agent-Based Modelling eased the use of these tools by archaeologists [9]. By focusing on the role of interactions between the systems components and on the way these micro-level interactions generate new macro-level properties and structures of the system, Complex Adaptive Systems theory is particularly well suited to consider questions that are perennial in Archaeology, such as the question of origin (for example: How urban centers arose from scattered settlements? How chiefdom developed from a previously egalitarian social organisation? etc.). The concepts of emergence and self-organisation, which are key-concepts in complexity theory, also led to new approaches to the question of innovation, which is central in the study of socio-systems, whether it is technical, cultural or societal innovation [10]. In other words, complexity theory provides a relevant framework to address the question of change, which is fundamental in historical sciences.

## 2 Why model in Archaeology?

It is worth recalling that Archaeologists, like other scientists, have always used models, even the most discursive informal explanation for “how” or “why” something happened in the past, is already a model [6]. But archaeological data present some specificities which invite one to turn to more formal models. Indeed, what we observe in Archaeology are remains of processes but not the processes that produced these remains. Archaeologists can thus only observe snapshots of the past, but no dynamics. We must therefore infer past dynamics (processes, behaviour) from a static archaeological record [11]. The usual means to do this are to compare the patterns in the archaeological record with the patterns expected from the supposed underlying process or behaviour. The selection of candidate underlying processes or behaviour is usually based on common sense, previous knowledge, other sources of information (ancient texts for example), ethnographic analogies and environmental regularities, or in some very specific cases, experimental archaeology [12]. But to prove or disprove an interpretation is difficult in Archaeology as, like in other social sciences, the popperian model of theory testing by experimentation and refutation is not applicable, except for very specific and narrow topics [13]. A theory is then usually – and never absolutely – confirmed by the accumulation of convergent indices, while the discovery of contradictory elements will dismiss it. This explains why concurrent interpretations and theories about the same phenomenon can coexist in Archaeology as in many social sciences. In this context, models are very useful tools to test our hypothesis and theories by looking at the dynamic

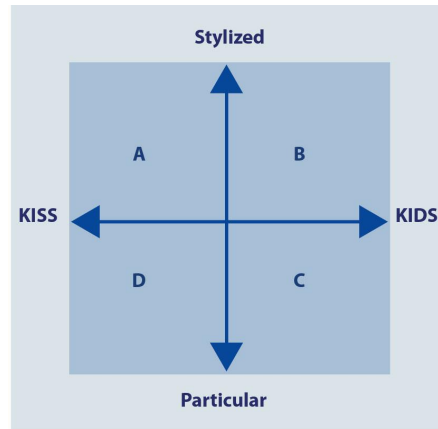
consequences of these theories, as simulation models help identifying which processes or behaviour could have created the archaeological patterns we observe. The idea is not to reproduce past reality, which is out of reach, but to select within our hypothesis which ones are the most plausible. In that sense, models are tools to think, not only to test hypotheses but also to elaborate them. They provide a testing of an hypothesis of process more than a proof of the existence of process (“c’est une mise à l’épreuve plus qu’une preuve”: [14]).

### 3 Agent-Based Modelling

Within the range of available simulation tools, Agent-Based Modelling is the most developed in Archaeology [12, 15]. Some reasons are technical, ABM being more flexible than, for example, Dynamical Systems Models as it does not require formal mathematical expression of the model and uses algorithmic formalism that is closer to natural language, and thus more accessible to social scientists. Another advantage of ABM concerns the model outputs: ABM allows one to explore the outcome of behaviour aggregated at a coarse-grained spatial and temporal resolution, which fits the resolution of the archaeological records. But more fundamentally, ABM is particularly well suited to explore the evolution of past societies, which involves complex interactions between social processes and natural phenomena, such as climatic change: agents interact between each other and also with their environment, and ABM is particularly relevant to model these interactions and feedback, and their effects on the system dynamics. This usually requires the combination of several sub-models (social, palaeoclimatic, or palaeoenvironmental, for example), leading to very complex models, for example, the Artificial Anasazi model [16], the Village Ecodynamics Project ([9, 17] or the *ENKIMDU* Model [18]. Another interest of ABM is that it allows to take into account “cognitive” or “deliberative” agents and not only rule-based reactive agents, a possibility that opens very interesting perspectives to differentiate agents’ behaviour according to their knowledge, beliefs, desires and goals [19]. ABM thus has the potential to model long-term social change without losing sight of the individual actions that underly it. In that sense, ABM might help reconcile processual interest in societal systems with post-processual concern for human agency [15].

However, these modelling practices remain the minority in Archaeology and concern a small quantitative community, interested in specific issues such as human evolution, evolutionary Archaeology or long-term socio-natural studies. In France, their development started recently, through the

**Fig. 1** The descriptive grid to classify models of spatial systems according to their level of abstraction and simplification (figure published in Banos *et al.* 2017, p. 102 and reproduced with the authorisation of A. Banos and L. Sanders)



collaboration of archaeologists and geographers who share common interests in the long-term evolution of settlement systems, such as in the ANR project, TransMonDyn [20].

#### 4 Abstraction vs Singularity; Simplification vs Realism

If models are used to test hypotheses about the processes supposed to have generated the observed archaeological patterns, validation of the model implies to compare the simulated outputs with archaeological records. This requires a rather good match between the model and “reality”. But too realistic models are not necessarily better. Firstly because they might suggest that the model is an exact replica of real world, which is never the case as modelling always require simplification and schematisation. This is particularly critical in Archaeology where the observed records are only partial remains of past reality. In addition, there is a risk that such a specific and detailed model does not bring any new knowledge than the ones entered as inputs. There is indeed a tension amongst complex systems models between, on the one hand, simplification and abstraction and, on the other hand, realism and singularity. These opposite polarities in the modelling practices have been formalized by Lena Sanders and Arnaud Banos [21]. They proposed a descriptive grid to classify models of spatial systems according to the level of abstraction of the modelled phenomenon, from the most particular to the most stylized, and to the level of simplification of the model itself, which can be evaluated according to the KISS and KIDS principles (see Fig. 1).

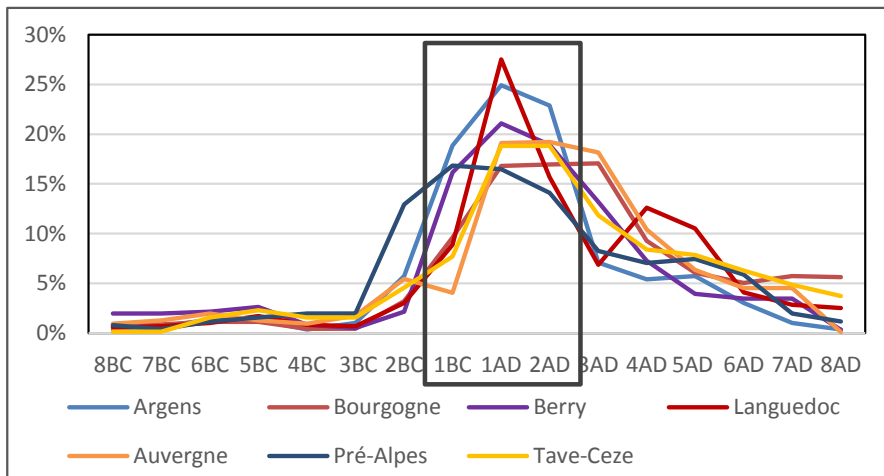


**Fig. 2** % of settlements per century in 7 micro-regions of Southern and Central France (© ArchaeDyn, ANR-08-BLAN-0157-01, 2008-2012).

The “Keep It Simple, Stupid!” or KISS principle, stated by Robert Axelrod [22], claims that the complexity of a model lies in the results of the simulation, not on the hypotheses, which must be as simple as possible and reflect the main fundamental processes of the simulated phenomenon. To the contrary, the “Keep It Descriptive, Stupid!” or KIDS principle, developed by Bruce Edmond and Scott Moss in reaction to the previous, focus on the hypotheses, which must be closer to reality in order to be able to explain the simulated results [23]. These type of models are thus more complex than KISS models.

## 5 The ModelAnSet project

These polarities can also be viewed as various steps in the building process of a model itself and we will take as an example the model we are building within the ModelAnSet project (Modelling the role of socio-environmental interactions on Ancient Settlement Dynamics), supported by UCA<sup>JEDI</sup> Complex Systems Academy of Excellence. Agent-Based Modelling is used to explore the respective roles of environmental and social factors in the evolution of the settlement pattern and dynamics during the Roman period in South-Eastern France. The initial motivation to develop the model was to better understand which processes could explain two typical characteris-

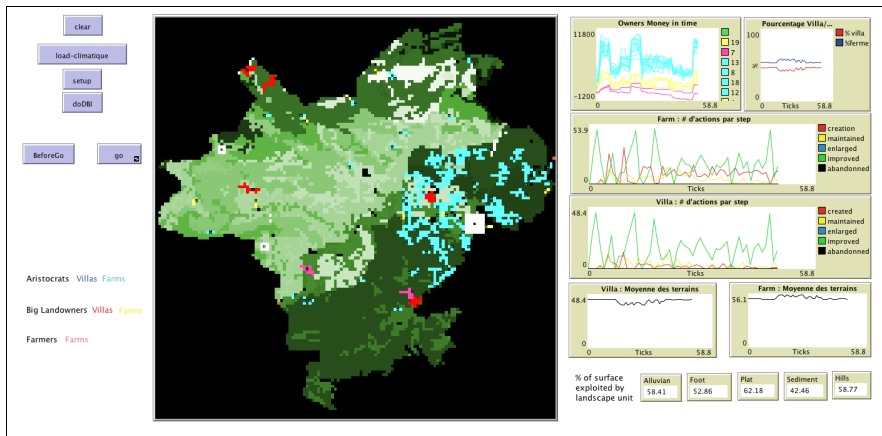


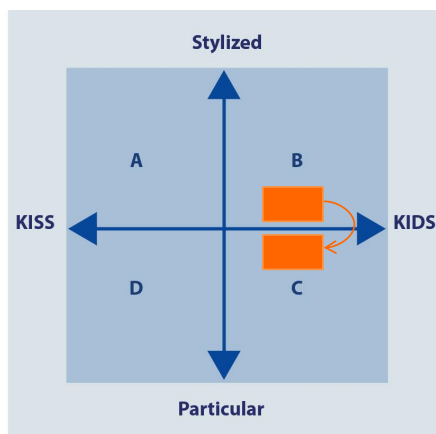
Fig. 3 Implementation of the ModelAnSet ABM on the NetLogo platform (1<sup>st</sup> version, Jérémy Lefebvre and Rami Ajroud, January 2018)

tics of Gallo-Roman settlement pattern during the first three centuries of the Christian era. Archaeological records evidence a strong increase in the number of rural settlements in Gaul from the 1<sup>st</sup> c. BC, followed by a steep decrease in the 2<sup>nd</sup> c. AD (see Fig. 2).

This is concomitant with the development of a new type of rural settlement, the *villa*, which conveys from Rome new ways of life and land-exploitation to the conquered provinces. Our aim is to test the impact of social and natural processes on these evolutions through the simulation of the behaviour of Gallo-Roman landowners, who were the main actors of land exploitation and settlement.

According to historical and archaeological data, we defined different behaviours of the landowners according to their socio-economical status and their perception of land rentability. We consider that the main factors influencing land rentability to be climatic change, which impacts land fertility, and the macro-economical context that impacts the economical power of the landowners. These parameters were also defined from multidisciplinary sources of knowledge. According to their economical power and the rentability of their rural exploitations, agents (the landowners) can make various decisions about their exploitations: they can enlarge, improve or maintain them without change, or abandon them or create a new exploitation, either a farm or a *villa*. Thus, repeated landowner decision-making produces a changing macro-level settlement pattern, in terms of number, type and spatial location of the settlements. The model includes feedback between agents' behaviour and the properties of their environment, as they

**Fig. 4** Position of the ModelAnSet model on Banos and Sanders graph to classify models of spatial systems according to their level of abstraction and simplification (figure adapted from Banos *et al.* 2017, p. 102 and published with the authorisation of A. Banos and L. Sanders)



can improve land productivity but also degrade it by over-exploitation. Although the hypotheses to test are rather generic, they were instantiated in a specific geographical context, which is the territory of the Roman colony of *Forum Iulii*, actual Fréjus in the South-East of France (Var department ; see Fig. 3).

This instantiation helped calibrate some model parameters (for example, defining the relative proportions of towns, *villas* and farms in the settlement system) and will mainly allow us to place the simulation in a realistic environment based on the actual landscape of this area. As environmental factors play an important part in the model dynamic, we assume that this effort towards environmental realism is required to be able to compare the model results with the archaeological records, although this instantiation is not fully implemented yet in the ABM.

If we go back to the Banos and Sanders graph, we can thus place our model towards the descriptive side of it, closer to the KIDS principle. In its present version, which uses a virtual environment made of 5 environmental units randomly situated, the model is still rather stylized, and can then be placed in the B quarter of the graph, but when the realistic environment will be implemented, the model will definitely increase its singularity, moving to the C quarter (see Fig. 4).

## Conclusion

In a discipline such as Archaeology, where dynamics cannot be observed, simulation models are the only tools allowing us to generate processes and

test their relevance to produce the observed archaeological records. This requires a certain amount of realism for the models, although a good fit between the modelling results and the observed patterns is not a sufficient proof as different processes can create similar patterns. Rather than offering an absolute validation, models allow us to reduce the range of candidate processes by focussing on the most effective ones. This is what we seek with the ABM under development within the ModelAnSet project.

## References

1. Flannery K.: Archaeology systems theory and early Mesoamerica, *In: Meggers B.J.* (ed.). *Anthropological Archaeology in the Americas*, Washington, D.C., Anthropological Society of Washington, p. 67-87 (1968)
2. Clarke D.L.: *Analytical Archaeology*, London, Methuen, p. 684 (1968)
3. Clarke D.L. (ed.): *Models in Archaeology*, London, Methuen (1972)
4. Van der Leeuw, S., McGlade J. (eds): *Time, Process and Structured Transformation in Archaeology*, Routledge, London (1997)
5. Kohler T.A., Gummerman G. (eds.): *Dynamics in Human and Primate Societies: Agent-based Modeling of Social and Spatial Processes*, Santa Fe Institute Studies in the Sciences of Complexity. Oxford University Press, New York (2000)
6. Kohler T.A., van der Leeuw S. (eds.): *Model-Based Archaeology of Socionatural Systems*, SAR Press, Santa Fe (2007)
7. Bentley A., Maschner H.D.G.: *Complex Systems and Archeology. Empirical and theoretical applications*, *Foundations of Archaeological Inquiry*, University of Utah Press, p. 160 (2003)
8. Wood, J. J., Matson R. G.: Two models of sociocultural systems and their implications for the archaeological study of change. *In: Renfrew C.* (ed.) . *The Explanation of Culture Change*. London, Duckworth, p. 673-683 (1973).
9. Kohler T.A.: *Complex Systems and Archaeology. In: Hodder, I. Archaeological Theory Today* (2nd ed.), Polity Press, Cambridge (2012)
10. Lane D., Pumain D., van der Leeuw S., West G. (eds.): *Complexity Perspectives in Innovation and Social Change*, Springer, Methodos Series (2009)
11. Binford L. R.: *Bones: Ancient Men and Modern Myths*, Academic Press, New York (1981).
12. Lake M.W., 2015: Explaining the Past with ABM: on Modelling Philosophy. *In: Wurzer G., Kowarik K., Reschreiter H.* (eds.). *Agent-Based Modeling and Simulation in Archaeology* (Advances in Geographic Information Science). Springer-Verlag, Berlin p. 3-36 (2015)
13. Fusco G., Bertonecello F., Candau J., Emsellem K., Huet T., Longhi C., Poinat S., Primon J.-L., Rinaudo C.: Faire science avec l'incertitude : réflexions sur la production des connaissances en Sciences Humaines et Sociales. Actes de la Table ronde "Incertain et connaissances en SHS : production, diffusion, transfert. Juin 2014, Nice (2015) <https://halshs.archives-ouvertes.fr/halshs-01166287>
14. Tannier C., Franc A., Ouriachi M.-J., Zadora-Rio E.: Entre modèles et récits, les transitions dans les systèmes de peuplement. *In: Sanders L.* (ed.). *Peupler la terre. De la préhistoire à l'ère des métropoles*. Tours, Presses Universitaires François Rabelais p. 387-407 (2017).

15. Lake M.W.: Trends in Archaeological Simulation, *Journal of Archaeological Method and Theory* **21**, p. 258–287 (2014)
16. Axtell R.L., Epstein J.M., Dean J.S., Gumerman G.J., Swedlund A.C., Harburger J., Chakravarty S., Hammond R., Parker J., Parker M.: Population growth and collapse in a multiagent model of the kayenta anasazi in long house valley, *PNAS*, **99** (Suppl 3), 7275 (2002)
17. Kohler T.A., Johnson C.D., Varien M., Ortman S., Reynolds R., Kobti Z., Cowan J., Kolm K., Smith S., Yap L.: Settlement ecodynamics in the prehispanic central Mesa Verde region. In: Kohler T. A., van der Leeuw S. (eds.). *The model-based archaeology of socrionatural systems*, SAR Press, Santa Fe, NM, p. 61–104 (2007).
18. Wilkinson T.J., Christiansen J., Ur J., Widell M., Altaweel M.: Urbanization within a dynamic environment: modeling Bronze Age communities in upper Mesopotamia, *American Anthropologist* **109** (1), p. 52–68 (2007)
19. Bratman M.: *Intentions, Plans, and Practical Reason*, Harvard University Press, Cambridge (1987).
20. Sanders L. (ed.): *Peupler la terre. De la préhistoire à l'ère des métropoles*, Tours, Presses Universitaires François Rabelais, p. 527 (2017)
21. Banos A., Sanders L.: Modéliser et simuler les systèmes spatiaux en géographie. In Varenne F, Silberstein M. (dir). *Modéliser et Simuler - Epistémologies et pratiques des modèles et des simulations*. Paris, Matériologiques, p. 833-863 (2013).
22. Axelrod R.: *The Complexity of Cooperation: Agent-Based Models of Competition and collaboration*, Princeton, Princeton University Press, (1997)
23. Edmonds B., Moss S.: From KISS to KIDS in Multi-Agent and Multi-Agent Based Simulation, *Lecture Notes in Computer Science*, **3415**, 130-144 (2005)
24. Banos A., Le Néchet F, Ouriachi M.-J., Franc A.: Simuler des transitions : une introduction aux modèles spatio-temporels, In Sanders L. (ed.). *Peupler la terre. De la préhistoire à l'ère des métropoles*. Tours, Presses Universitaires François Rabelais, p. 89-110 (2017)
25. Kohler T.A., Varien M.D. (eds.): *Emergence and Collapse of Early Villages: Models of Central Mesa Verde Archaeology*, University of California Press, Berkeley, (2012). (<http://www.ucpress.edu/ebook.php?isbn=9780520951990>)

# Enhancing magnetic separation of nanoparticles

Pavel Kuzhir, Hinda Ezzaier, Jessica A. Marins,  
Cécilia Magnet, Yaroslava Izmaylov, Cyrille Claudet

**Abstract** This paper briefly reviews our recent advances in the magnetic separation of nanoparticles, which has long been considered challenging because of their strong Brownian motion. We show that field-induced phase separation enhances significantly the efficiency of nanoparticle magnetic separation that is expected to give rise to numerous emerging applications of magnetic nanoparticles

---

P. Kuzhir

Institut de Physique de Nice (INPHYNI), CNRS UMR 7010, UCA, Parc Valrose, 06108  
Nice cedex 2, France, e-mail: [Pavel.Kuzhir@unice.fr](mailto:Pavel.Kuzhir@unice.fr)

H. Ezzaier

Institut de Physique de Nice (INPHYNI), CNRS UMR 7010, UCA, Parc Valrose, 06108  
Nice cedex 2, France, e-mail: [ezzaier.hinda@gmail.com](mailto:ezzaier.hinda@gmail.com)

J.A. Marins

Institut de Physique de Nice (INPHYNI), CNRS UMR 7010, UCA, Parc Valrose, 06108  
Nice cedex 2, France, e-mail: [jessica.alves-marins@inphyni.cnrs.fr](mailto:jessica.alves-marins@inphyni.cnrs.fr)

C. Magnet

Institut de Physique de Nice (INPHYNI), CNRS UMR 7010, UCA, Parc Valrose, 06108  
Nice cedex 2, France, e-mail: [Cecilia.Magnet@unice.fr](mailto:Cecilia.Magnet@unice.fr)

Y. Izmaylov

Institut de Physique de Nice (INPHYNI), CNRS UMR 7010, UCA, Parc Valrose, 06108  
Nice cedex 2, France, e-mail: [yaroslava.izmaylov@inphyni.cnrs.fr](mailto:yaroslava.izmaylov@inphyni.cnrs.fr)

C. Claudet

Institut de Physique de Nice (INPHYNI), CNRS UMR 7010, UCA, Parc Valrose, 06108  
Nice cedex 2, France, e-mail: [cyrille.claudet@inphyni.cnrs.fr](mailto:cyrille.claudet@inphyni.cnrs.fr)

## 1 Introduction

Magnetic separation is a process in which magnetizable particles are extracted from a suspending liquid by means of magnetic field gradients. Apart from the classical application to ore beneficiation [1], magnetic separation has been finding new, emerging applications in water purification [2] and in the separation of living cells or biological molecules [3]. The basic idea is to attach pollutant molecules, biomolecules or cells to magnetic particles and extract them from the suspending liquid using an externally applied non-uniform magnetic field that creates a magnetic force on particles making them move in the direction of the magnetic field gradient. In most existing applications, magnetic micron-sized particles are used, providing an easy magnetic separation with moderate magnetic fields, while the use of nanoparticles is considered to be inefficient because of their strong Brownian motion. This is a real technological barrier for many biological and environmental applications because small nanoparticles have a high specific area and would capture larger amounts of molecules by unit suspension volume as compared to microbeads; this would allow either an enhancement of the biomolecule detection or reduction of the amount of reagents necessary for bioanalysis or water purification. Magnetic separation efficiency of nanoparticles is especially low in microfluidic devices relevant for most biomedical applications because it is difficult to realize high magnetic fields in a compact geometry of these devices.

However, a few years ago, we showed that the magnetic separation of nanoparticles can still be efficient if they undergo a field-induced phase separation manifested by appearance of long micron-sized needle-like aggregates containing millions of nanoparticles [4, 5]. The capture efficiency of such a phase separating system is related to the aggregate size scale rather than to the size of individual nanoparticles. To benefit from the phase separation to enhance the magnetic separation of nanoparticles, one needs to know: (a) the range of magnetic field intensity and nanoparticle concentration at which the phase separation takes place; (b) how fast the phase separation is in comparison to magnetic separation; (c) what is the optimal geometry of the magnetic separator providing a maximal capture efficiency of nanoparticles. These points impose a detailed study of (a) the phase separation equilibrium with establishment of the phase diagrams; (b) kinetics of field-induced nanoparticle aggregation; (c) capture of nanoparticles on magnetizable collectors of a microfluidic magnetic separator. In this paper, we briefly review these points and show how basic physical concepts allow designing a very efficient magneto-microfluidic separation system expected to give a considerable improvement of high sensitivity immunoassays.

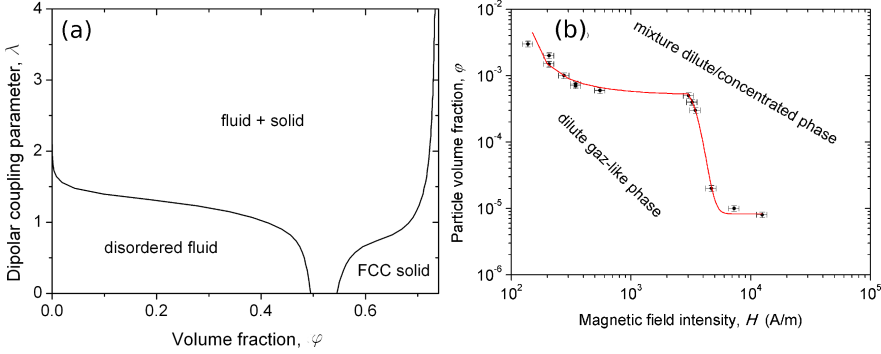


**Fig. 1** Theoretical (a) and experimental (b) phase diagrams of a suspension of magnetizable nanoparticles showing diluted phase (disordered fluid), a concentrated phase (fcc solid) and a mixture of both phases (fluid + solid). Only one binodal curve is accessible in experiments and this curve corresponds to the onset of field-induced aggregation. (a) is reprinted from Magnet et al. *Phys Rev E* **89**, 032310 (2014) with kind permission of American Physical Society and (b) is reprinted from Ezzaier et al. *J. Chem. Phys.* **146**, 114902 (2017) with kind permission of American Institute of Physics.

## 2 Phase equilibrium

Let us consider a homogeneous suspension of Brownian magnetizable nanoparticles of a diameter  $d$  dispersed in a liquid. If this suspension is subjected to a uniform external magnetic field of an intensity  $H$ , the nanoparticles acquire a magnetic moment  $m$  and undergo dipolar interactions between them. If the particle concentration and the applied magnetic field are strong enough, the suspension will undergo a phase separation, i.e., the nanoparticles will form dense needle-like aggregates (concentrated phase) separated by a suspending liquid containing a small amount of particles (dilute phase). The phase separation is governed by two dimensionless parameters – the nanoparticle volume fraction  $\phi$  and the dipolar coupling parameter  $\lambda$  defined as a ratio of the dipolar interaction energy to the thermal agitation energy  $k_B T$ :

$$\lambda \sim \frac{m^2}{\mu_0 k_B T d^3} \sim \frac{\mu_0 H^2 d^3}{k_B T}, \quad (1)$$

where  $\mu_0 = 4\pi \times 10^{-7}$  H/m is the magnetic permeability of vacuum.

The dilute and concentrated phases, as well as their mixture, are mapped onto a  $\lambda$ - $\phi$  phase diagram shown in Fig. 1a with the boundaries between phases (binodal curves) calculated by equating chemical potentials and osmotic pressures in both phases [6].

As inferred from Fig. 1a, the dilute phase occupies the space below the left binodal curve, the concentrated phase is below the right binodal curve, while the mixture of two phases is between these curves. The left binodal curve shows at which critical dipolar coupling parameter (or, equivalently, critical magnetic field) the nanoparticles start to aggregate and thus bears the important information for the magneto-microfluidic separation (Sec. IV). This curve was also measured experimentally by direct optical observation of the aggregation of a nanoparticle suspension subjected to different external magnetic fields [7]. As nanoparticles, we used nanoclusters of a medium size of the order of 50 nm dispersed in water and composed of a dozen smaller iron oxide nanoparticles assembled by a double layer oleic acid surfactant [8]. The same nanoparticles have been used for all experiments presented in the current paper. The shape of the experimental binodal curve, shown in Fig. 1b, exhibits some similarities with the left binodal curve of Fig. 1a calculated theoretically. However, the theory underestimates the critical magnetic field of the onset of aggregation, likely because of attractive van der Waals interactions between nanoparticles ignored in the theory.

### 3 Kinetics of aggregation

The field-induced phase separation described in Sec. 2 has a certain time-scale, important for a proper design of the magneto-microfluidic separation system. Experimentally, kinetics of phase separation or, equivalently, kinetics of nanoparticle aggregation has been studied by optical observation of a nanoparticle suspension sandwiched between two glass plates and subjected to an external magnetic field of a given intensity  $H$  [7]. Starting from some time elapsed from the moment of the magnetic field application, one observes appearance of black stripes aligned with the direction of the applied magnetic field and corresponding to bulk needle-like aggregates of a length of the order of a hundred of microns and a width of the order of a few microns. The effect of the particle volume fraction  $\varphi$  and of the applied magnetic field  $H$  on the aggregation state of the suspension is inspected in Fig. 2 where snapshots of the suspension microstructure are shown at a given elapsed time  $t = 20$  min but for different  $\varphi$  and  $H$ . As expected, the aggregate length and thickness seem to increase significantly with increasing magnetic field and particle concentration thanks to enhancement of magnetic interactions between nanoparticles.

To quantify the kinetics of aggregation, the time dependence of the aggregate average length  $L$  is inspected in Fig. 3 for the magnetic field intensity  $H = 2.75$  kA/m and for three different particle volume fractions. The experi-

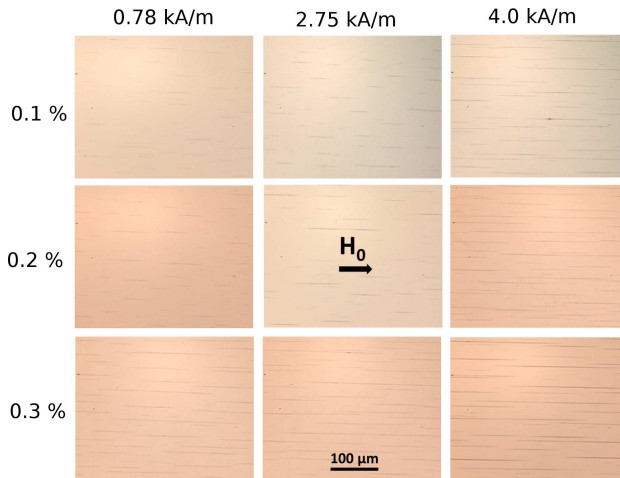


**Fig. 2** Snapshots of the suspension microstructure at the fixed elapsed time  $t = 20$  min and different intensities  $H$  (or  $H_0$ ) of the applied magnetic field and different particle volume fractions  $\varphi$  (reprinted from Ezzaier et al. *J. Chem. Phys.* **146**, 114902 (2017) with kind permission of American Institute of Physics).

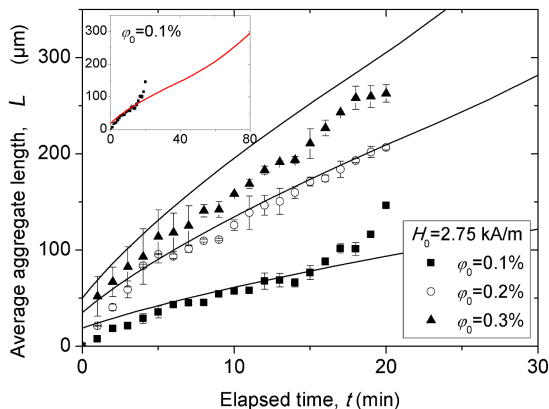
mental curves show an initial sublinear increase of the aggregate length with time, followed by a change in the slope at  $t \approx 10 - 15$  min and by a stronger increase. From the theoretical point of view, a stage of aggregate growth (by diffusion and magnetophoretic migration of nanoparticles towards primary nuclei) is expected at shorter times providing a sublinear section of  $L(t)$ -dependency, while a coalescence regime (merging of aggregates due to their dipole-dipole interaction) is expected at longer times providing a stronger than linear increase of the aggregate size. Transition between two regimes is supposed to take place when the aggregation rate of the coalescence stage becomes larger than that of the aggregate growth stage; such a transition results in a change of the slope of the  $L(t)$ -curves. Our theoretical model (solid curves on Fig. 3) fits at least semi-quantitatively to the experiments. As inferred from the figure inset, the change of the slope is predicted at higher elapsed times than those observed in experiments.

The most important issues for magnetic separation (Sec. 4) are the time-scales  $t_G$  and  $t_C$  of the aggregate growth and coalescence stages, respectively:

$$t_G \sim \frac{d^2}{D_n \Delta_0} \left( \frac{V_m}{d^3} \right)^{4/7}; \quad t_C \sim \frac{\eta}{\Phi \mu_0 M^2}, \quad (2)$$

where  $D_n$  is the nanoparticle diffusion coefficient;  $\Delta_0 = \varphi - \varphi'(\lambda)$  is the initial supersaturation of the suspension corresponding to the difference of the

**Fig. 3** Experimental (symbols) and theoretical (lines) dependencies of the average aggregate length on elapsed time for the applied magnetic field  $H = 2.75$  kA/m at different particle volume fractions. The inset shows the same dependency for  $\varphi = 0.1$  vol.% in an extended timescale (reprinted from Ezzaier et al. J. Chem. Phys. **146**, 114902 (2017) with the kind permission of the American Institute of Physics).



particle volume fraction and the critical volume fraction  $\varphi^*(\lambda)$  at the onset of aggregation (left binodal curve on Fig. 1a or the curve on Fig. 1b);  $V_m$  is the maximum aggregate volume in the aggregate growth regime corresponding to vanishing supersaturation;  $\eta$  is the suspending liquid viscosity;  $M$  and  $\Phi$  are the magnetization of aggregates and their volume fraction in the suspension, respectively. Both estimations using Eq. 2 and experiments show that the shortest timescale giving the aggregate length of the order of  $10 \mu\text{m}$  is about 1 min. Thus, we have to design the magnetic separation system in such a way that the particle traveling time has to be larger than  $t \sim 1$  min such that the nanoparticles have enough time to aggregate under the action of the applied field.

## 4 Magnetic separation

Ordered arrays of magnetizable micropillars are considered to be one of the most effective geometries for the separation of magnetic micron sized particles in microfluidic scale [9, 10]. We have shown that such system provides an acceptable capture efficiency of magnetic nanoparticles undergoing field-induced aggregation [4]. A sketch of a microscale channel equipped with an array of nickel micropillars is presented in Fig. 4. Micropillar arrays were grown on a glass substrate by electroplating and soft photolithography. In experiments an aqueous suspension of iron oxide nanoparticles of a desired concentration  $\varphi$  was pushed through the channel at a desired speed  $u$  using

**Fig. 4** Microfluidic channel with a micropillar array (reprinted from Ezzaier et al. *J. Magn. Magn. Mater.* **459**, 350 (2018) with the kind permission of Elsevier)

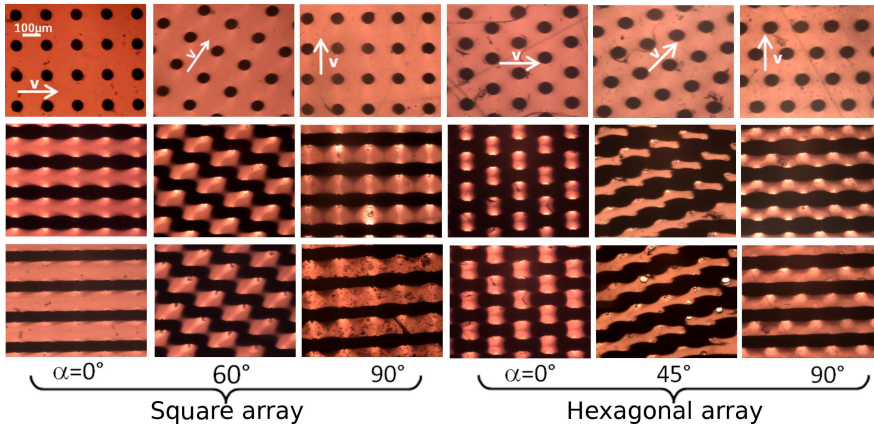
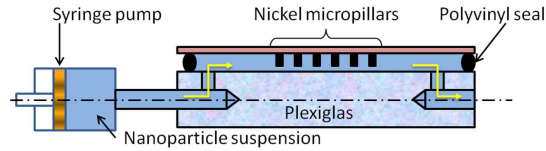
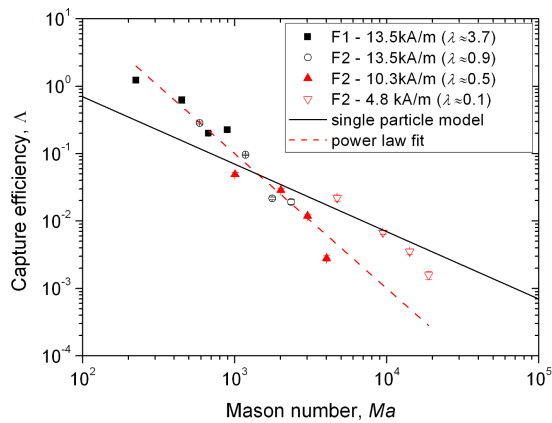


**Fig. 5** Snapshots of nanoparticle deposits around micropillars (reprinted from Ezzaier et al. *J. Magn. Magn. Mater.* **459**, 350 (2018) with the kind permission of Elsevier)

a syringe pump and in the presence of an external magnetic field of a given intensity  $H$ .

Once the field was applied, the nickel micropillars became magnetized and started to attract magnetic nanoparticles and separate them from the suspending liquid (water) building particle deposits around the micropillars. Snapshots of nanoparticle deposits were recorded over time and some of them are shown in Fig. 5. The upper row of snapshots shows the top view of the micropillar arrays without captured nanoparticles, the middle and the bottom rows show nanoparticle deposits at the flow speed  $u = 0.71$  mm/s and 2.14 mm/s, respectively, at an applied magnetic field  $H = 13.5$  kA/m, nanoparticle volume fraction  $\varphi = 0.3$  vol.% and elapsed time  $t = 60$  min. Different columns correspond to different directions between the flow and the magnetic field, characterized by an angle  $\alpha$ . Qualitatively, the flow intensity and orientation influence the shape of the deposits that evolve to a straight pattern with increasing speed in the case of a square array with  $\alpha = 0^\circ$  [bottom left snapshot in Fig. 5] or to honeycomb pattern in the case of hexagonal array at  $\alpha = 0^\circ$  [4<sup>th</sup> column from the left on Fig. 5].

**Fig. 6** Mason number dependency of the capture efficiency at different dipolar coupling parameters  $\lambda$  and fixed values of  $\varphi = 0.3\%$ ,  $\alpha = 0^\circ$  and for the square array (reprinted from Ezzaier et al. J. Magn. Magn. Mater. **459**, 350 (2018) with the kind permission of Elsevier).



Quantitatively, experimental dependencies of the deposit area  $S$  on elapsed time  $t$  were obtained by image processing of the snapshots. The slope of the experimental  $S(t)$  curves was related to the capture efficiency – the key parameter characterizing the separation performance – defined as  $\Lambda = \ln(\varphi_{in}/\varphi_{out})$ , with  $\varphi_{in} = \varphi$  and  $\varphi_{out}$  being the nanoparticle volume fractions at the channel inlet and outlet respectively [11]. It has been shown that the most important parameter affecting the capture efficiency is the Mason number, defined as the ratio of hydrodynamic to magnetic forces acting on nanoparticles:

$$\text{Ma} = \frac{6\eta u D}{\beta \mu_0 H^2 d^2}, \quad (3)$$

where  $D = 50 \mu\text{m}$  is the micropillar diameter and  $\beta \approx 0.9$  is the magnetic contrast factor of nanoparticles. Mason number dependency of the capture efficiency  $\Lambda$  is plotted in Fig. 6 for three different values of the applied magnetic fields  $H$  and two different average diameters  $d$  of nanoparticles (samples F1 with  $d = 68 \text{ nm}$  and F2 with  $d = 42 \text{ nm}$ ).

Variations of  $d$  and  $H$  result in a variation in the dipolar coupling parameter [Eq. 1] in the range  $0.1 \leq \lambda \leq 3.7$ . Three experimental  $\Lambda$  versus  $\text{Ma}$  curves, corresponding to  $\lambda \leq 0.5$ , are gathered along a straight line in log-log scale and fitted by a scaling law  $\Lambda \propto \text{Ma}^{-2}$  (dashed line on Fig. 6), while the fourth curve with  $\lambda \approx 0.1$  shows a weaker Mason number dependency. Experiments show that nanoparticle suspensions undergo phase separation with appearance of bulk aggregates at  $\lambda \geq 0.5$  and  $\varphi = 0.3\%$ . Intense shear flows around the micropillars can disrupt nanoparticles from aggregates such that the aggregate size is expected to be a decreasing function of the Mason number. The combination of this effect with increasing convective

flux transporting the aggregates could explain a strong decrease of the capture efficiency with Mason number ( $\Delta \propto \text{Ma}^{-2}$ ) for  $\lambda \geq 0.5$ . Our theoretical model predicts a quite similar behavior ( $\Delta \propto \text{Ma}^{-1.7}$ ) [4]. Notice that in the considered range of the Mason numbers, the nanoparticle travel time is typically larger than the aggregation timescale  $\tau \sim 1$  min estimated in Sec. 3. This leaves enough time to the nanoparticle to form micron-sized aggregates that are efficiently captured by micropillars. However, nanoparticle suspensions do not exhibit phase separation at  $\lambda=0.1$  and  $\varphi = 0.3\%$ . In this case, the capture efficiency of individual nanoparticles is only defined by a compromise between convective and magnetophoretic fluxes resulting in a theoretical scaling law  $\Delta \propto \text{Ma}^{-1}$  [4] (solid line on Fig. 6), which fits reasonably well to experimental points for  $\lambda=0.1$  (triangles on Fig. 6). The effects of the particle concentration, magnetic field orientation and array geometry (square or hexagonal) are analysed in details in [11].

## 5 Conclusions

In this work, we have briefly reviewed magnetic separation of nanoparticles on a microfluidic scale. In the presence of an applied uniform magnetic field, the nanoparticle suspension may undergo a phase separation, fully governed by the particle volume fraction  $\varphi$  and the dipolar coupling parameter  $\lambda$  and accompanied by appearance of bulk needle-like aggregates. Such field-induced aggregation strongly enhances the capture efficiency of magnetic particles on ordered arrays of magnetizable micropillars, especially if the particle traveling time is larger than the aggregation timescale. The capture of such aggregates by micropillars depends mostly on the ratio of hydrodynamic-to-magnetic forces: the Mason number. Besides this, tuning the array's geometry and magnetic field orientation allows for the generation of particular patterns of nanoparticle deposits around the micropillars minimally affected by the flow and providing a maximized retention capacity. This could be useful for development of microscale magnetic separators for biomedical applications. In particular, we are currently working on nanoparticle-based magneto-microfluidic immunoassays with enhanced sensitivity.

We acknowledge the financial support of French government piloted by ANR in framework of the Future Investments UCA<sup>JEDI</sup> project, ANR-15-IDEX-01.

## References

1. Svoboda J.: *Magnetic Techniques for the Treatment of Materials*, Kluwer Academic, Dordrecht (2004)
2. Ambashta R.D., Sillanpää M.: Water purification using magnetic assistance: A review, *J. Hazardous Materials* **180**, 38 (2010)
3. Zborowski M., Chalmers J.J.: *Magnetic cell separation*, Elsevier, Amsterdam (2008)
4. Orlandi G., Kuzhir P., Izmaylov Y., Marins J. A., Ezzaier H., Robert L., Doutre F., Noblin X., Lomenech C., Bossis G., Meunier A., Sandoz G., and Zubarev A.: Microfluidic separation of magnetic nanoparticles on an ordered array of magnetized micropillars *Phys. Rev. E* **93**, 062604 (2016)
5. P. Kuzhir, C. Magnet, H. Ezzaier, A. Zubarev, G. Bossis: Magnetic filtration of phase separating ferrofluids: From basic concepts to microfluidic device *J. Magn. Magn. Mater.* **431**, 84 (2017).
6. C. Magnet, P. Kuzhir, G. Bossis, A. Meunier, S. Nave, A. Zubarev, C. Lomenech, and V. Bashstovoi: Behavior of nanoparticle clouds around a magnetized microsphere under magnetic and flow fields *Phys. Rev. E* **89** 032310 (2014).
7. Ezzaier H., Alves Marins J., Razvin I., Abbas M., Ben Haj Amara A., Zubarev A., Kuzhir P.: Two-stage kinetics of field-induced aggregation of medium-sized magnetic nanoparticles *J. Chem. Phys.* **146**, 114902 (2017).
8. Magnet C., Kuzhir P., Bossis G., Meunier A., Suloeva L., Zubarev A.: Haloing in bimodal magnetic colloids: The role of field-induced phase separation *Phys. Rev. E* **86** 011404 (2012).
9. Deng T., Prentiss M., Whitesides G.M.: Fabrication of magnetic microfiltration systems using soft lithography *Appl. Phys. Lett.* **80**, 461 (2002)
10. Palfreyman J.J., van Belle F., Lew W.-S., Mitrelias T., Bland J. A. C., Lopalco M., Bradley M.: Hybridization of Electrodeposited Magnetic Multilayer Micropillars *IEEE Trans. Magn.* **43**, 2439 (2007)
11. Ezzaier H., Marins J. A., Schaub S., Amara B. H., Kuzhir P.: Capture of magnetic nanoparticles on ordered magnetizable arrays: A parametric study *J. Magn. Magn. Mater.* **459**, 350 (2018)

# Semiconductor lasers: coherence and localized states

Stéphane Barland, Massimo Giudici,  
Gian Luca Lippi

**Abstract** Semiconductor lasers are tiny optoelectronic devices that are routinely used in countless applications ranging from computer pointing devices to optical data transmission. In addition to this, they can also serve as a versatile experimental platform for the exploration of dynamical systems and complex phenomena. In the following we discuss two phenomena that can take place (in markedly different situations) at the laser light emission threshold: the emergence of coherence and the formation of optical localized states.

## 1 Introduction

Semiconductor lasers are ubiquitous in modern life and the fundamental mechanisms that govern their light emission properties are most of the time completely transparent to the user. However, in spite of their robustness and apparent simplicity, those devices rely on delicate processes of interaction between light and matter. Among these, the one which is at the origin

---

Stéphane Barland

Université Côte d'Azur, CNRS, Institut de Physique de Nice. e-mail: [stephane.barland@univ-cotedazur.fr](mailto:stephane.barland@univ-cotedazur.fr)

Massimo Giudici

Université Côte d'Azur, Institut de Physique de Nice. e-mail: [massimo.giudici@inphyni.cnrs.fr](mailto:massimo.giudici@inphyni.cnrs.fr)

Gian-Luca Lippi

Université Côte d'Azur, Institut de Physique de Nice. e-mail: [gian-luca.lippi@inphyni.cnrs.fr](mailto:gian-luca.lippi@inphyni.cnrs.fr)

of their name is the process of light amplification by stimulated emission of radiation. In this process, energy supplied to matter (in most cases via the application of an electrical current) is converted into light. Thus, light is amplified and matter is de-excited, which of course implies a nonlinear mutual interaction. Since light that is generated by this process constantly escapes the laser (it is a light emitting device), this amplification process must be strong enough to overcome the exiting light flow. This balance implies the existence of an energy input *threshold* for the stationary emission of laser light. This simplified description hides a profound analysis of the laser threshold, which proves it to be an example of phase transition in a system out of thermodynamical equilibrium, since energy is constantly flowing in and out. Thus, semiconductor lasers can be used as model systems for the analysis of very general phenomena that can take place at phase transitions. In the following, we illustrate this approach by discussing two specific phenomena: the emergence of *coherence* and that of *localized states*.

## 2 Collective behavior of small systems: threshold crossing in micro- and nanolasers

A change in macroscopic state is a feature that occurs in a multitude of physical and non-physical systems. In everyday life this can be observed, for instance, in the change between ice and liquid water, or in the ordered state (magnetic) vs. the disordered state (non-magnetic) in iron. Lasers belong to this same class of phenomena even though their property, unlike the two previous examples, may not be intuitively associated with a phase transition. One basic feature, which is common to the first two systems, is the large number of “elements” that participate in the interaction: in the case of water and iron, the atomic density is so large that even a tiny volume (say  $1\text{mm}^3$ ) includes upwards of  $10^{18}$  atoms (or molecules), thus justifying the so-called thermodynamic limit, i.e., the limit of infinite system size. In lasers the “elements” are the number of modes of the electromagnetic field resonant in the cavity<sup>1</sup> volume (i.e., in three dimensions): this number, though not quite as large as that of the previous examples, easily amounts to  $10^5 - 10^6$  even for a tiny semiconductor laser (e.g., a laser pointer), thus the thermodynamic limit still represents a good approximation [1].

Recent progress in miniaturization has led to the investigation of phenomena at the nanoscale, opening up new questions rooted in the finite size of the sample where the collective behavior is sought. Lasers play a substantial role in this quest thanks to their comparatively already small number of

---

<sup>1</sup> cavity: an optical resonator, in many cases consisting of mirrors facing each other.

constituents compared to solids or liquids. As such, they play a double role of model system on the one hand, and of actual devices on the other hand, on which one can experiment and understand the modifications that the finite size brings to the collective behavior. In addition to the fundamental aspects of small sample behavior, nanolasers (i.e., lasers with submicrometric cavity volumes) are very appealing, for instance, as candidates for sources of coherent light directly integrated into future all-optical chips to replace today's electronics, but also as probes at the cellular scale for biomedical applications. However, in order to obtain a "correct" lasing behavior (i.e., coherent light) these nanodevices have to undergo the phase transition typical of their larger counterparts. This is easier said than done: the technological construction progress has certainly led to sub-wavelength light emitting sources but the questions on their "phase transition" have remained largely unanswered for the past thirty years. Two main elements are responsible for this failure: the lack of instrumentation capable of giving a thorough characterization of laser output at the very low photon flux emitted by a nanodevice, and the difficulty in setting up and treating models capable of handling a finite, but not small, number of components (here, emitters and cavity modes).

Rather than tackling the problem of the smallest devices, for the past few years we have been working on the characterization, both experimental [2] and numerical [3], of increasingly smaller lasers, starting from the usual macroscopic ones and leading towards the nanoscale. This choice presents the double advantage of following the gradual evolution of the features of the phase transition away from the thermodynamic limit, while allowing for a complete experimental characterization, thanks to the use of the most advanced instrumentation, still usable at the photon flux levels typical of the mesoscopic scale (intermediate between the macro- and the nanoscale) [4]. Our main findings, presented in detail in [4] together with other results on this topic, can be summarized by Fig. 1, which shows the "unfolding" of the laser threshold – i.e., the sharp transition of the macroscopic device (blue sketch in the bottom right corner of the figure) – into an ensemble of points. Each distinctive point is characterized by a physical feature and occurs at well-separated values of the energy supplied to the device – all points collapse together onto a single value for the power supplied to the device in macroscopic systems. Point B corresponds to the emergence of coherent oscillations between the two main variables that describe the physics of lasers (photon number and population inversion); point C to the largest amplitude self-induced oscillations in the output power and point D to the reaching of fully coherent emission (the Poisson statistics typical of *proper* lasing). Point A corresponds to desultory and uncorrelated laser pulses, interspersed with exclusively spontaneous photons, which precede the true continuous emission lasing. It is important to realize that these different regimes correspond

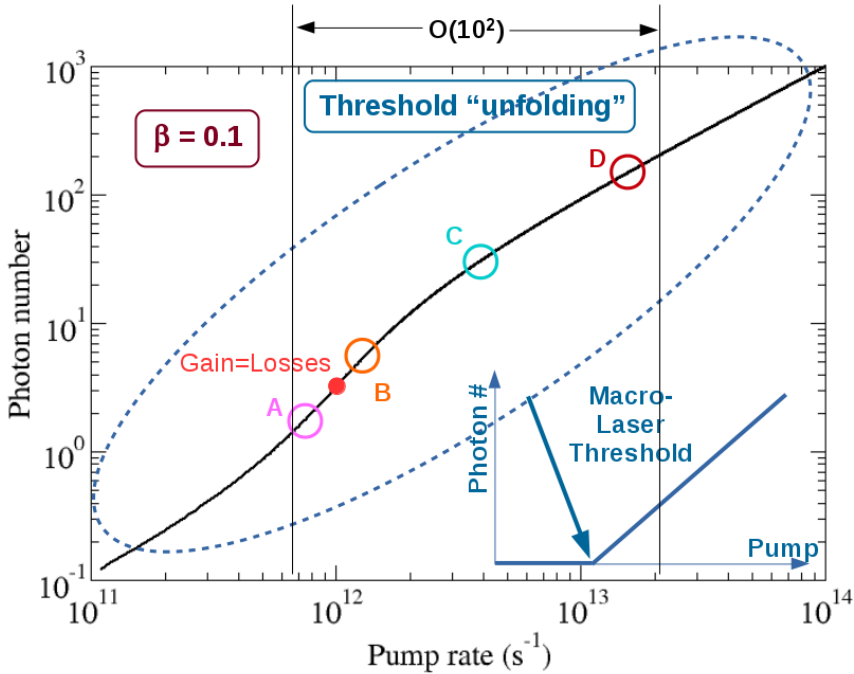


**Fig. 1** Schematic of the principle of the response – output number of photons – of a nanolaser ( $\beta = 0.1$ : fraction of the spontaneous emission coupled into the lasing mode) to external excitation – number of excited emitters per second (pump rate). The average photon lifetime in the cavity is taken to be  $10^{-11}$ s, thus at any time there are a few tens or hundred emitters excited, whence the relatively small number of photons available. The blue diagram, bottom right, represents the schematic shape of the response of a macrolaser, with its characteristic break in the line (threshold) of laser output. For the nanolaser the curve is smooth and threshold “unfolds” into an ensemble of separate points, as discussed in the text. The red point corresponds to the balance between the gain (from the external energy input) and losses, one of the criteria used to identify the macrolaser threshold.

to independent characterizations of threshold given for macroscopic lasers and collapse into a single point in large systems.

One important feature of these small devices is that they can also serve as generic models systems for complex systems. One example taken from everyday life is the dynamics of applause [5]. We know from experience that large groups can spontaneously produce synchronized clapping but that in smaller groups – barring previous agreements or signals in the crowd – synchronization does not easily occur (the group size could be mapped into the pump rate in Fig. 1). As an analogy, we could connect the first regime (A)

with the clapping of a few isolated people in an audience, (B) with the starting of applause that becomes more vigorous, yet disorderly, in (C) and may eventually reach synchronization (D). Of course this is only an analogy, but the information that can be gathered from a simpler system (in a laser there is no influence of group psychology or other *external* effects) may help identifying basic features that are common to many other complex systems as a function of system size.

### 3 Localized states

The spontaneous formation of spatial structures is a fascinating phenomenon whose understanding made a giant leap with the seminal work of Alan Turing on the chemical basis of morphogenesis in the biological realm [6]. Since that work, the dominant role of spatial coupling and nonlinear interactions in the formation of spatial structures has been established in many contexts such as liquid crystals, chemical reactions, solidification or fluid dynamics to name a few (see *e.g.*, [7]). With that in mind, one can expect that semiconductor lasers, out of equilibrium systems where (diffracting) light and (diffusing) matter interact nonlinearly, can support the formation of spatial structures. One particularly interesting case is that of so called *localized structures*, which can be generally viewed as domains of finite size enclosed by stationary fronts [8]. Such structures have been observed in a variety of systems, from plant ecology to nonlinear optics [9]. Of course, such structures whose formation is dominated by nonlinearity and which are only mildly influenced by boundary conditions can only exist in systems whose spatial extension is large enough. Thus, in contrast to the case discussed above in section 2 where the laser device was chosen to have an extremely small spatial extension, here we consider semiconductor lasers that are large enough to host optical localized states. In this specific context we focus much less on the statistical or spectral properties of the electric field and a very efficient description of the device can be obtained by considering the mean field dynamics, which describes the slowly varying amplitude of a coherent electric field without considering spontaneous emission. Then, the laser phase transition described in section 2 is described in terms of a supercritical Hopf bifurcation. On the other hand, localized states appear as a result of a *subcritical* bifurcation since they must connect asymptotically to some other stable solution. This can be achieved in a variety of ways and we have demonstrated experimentally the existence of optical localized states in several configurations, including applying an external forcing [10] or inserting in the laser

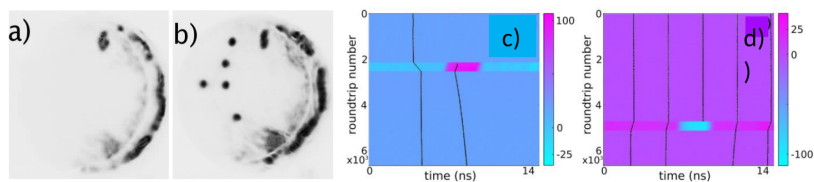


**Fig. 2** Generation of localized states in a broad area semiconductor laser. a) stable homogeneous solution. Full width of the image is 200 micrometers. b) bistable and mutually independent localized states consisting of high light intensity emission can be addressed by suitable optical perturbations. From [10] c,d): Temporal localized states generation in the output of a semiconductor laser. Localized states in the cavity are represented by the black trace while the bias current pulse used for writing the localized state is represented in color code. Panel c) writing of a temporal localized states by an electrical pulse in the pumping current starting from a situation where one localized state was present before the addressing pulse. Panel d) shows the erasing of one temporal localized state by a negative electrical pulse from a situation where five localized states were present. From [12].

device an element whose optical absorption varies with the amount of light it receives [11].

### 3.1 Localized states along propagation direction

One common point of those experiments is that the spatial extension of the device was *transverse* to the direction of propagation of the field. In more recent works we have addressed the question of whether the concept of localized states can be extended to the time domain or, equivalently, to the propagation direction of the electromagnetic field where localized states appear in the form of pulses of light. In this context, the system size is given by the longitudinal dimension of the resonator and the notion of large-aspect ratio can be formulated by requiring that the cavity round-trip time  $T$  must be much larger than the active material timescales  $\tau$ . We have implemented temporal localized states in a passively pulsing mode-locked semiconductor external cavity lasers in the limit  $T \gg \tau$ , see Fig. 2 c,d). For the proper system parameter the bifurcation from stationary solution to mode-locked pulsing occurs subcritically, thus leading to a favorable situation for generation of localized states [13].

These results pave the way towards observation of spatio-temporal localized structures, also called Light Bullets. Since the pioneer work of Silberberg in the beginning of '90, these light bullets have been actively sought in the last 25 years. Despite the efforts made, robust light bullets have never

been observed experimentally because the equilibrium between nonlinearities and spatio-temporal mechanisms spreading the pulse is very fragile. Beyond their fundamental interest, light bullets are very attractive for their applications. In particular, when used as fundamental bits for information processing, they are forecasted to enable reaching a THz bandwidth. The above described results suggest that dissipative light may be obtained in a broad-area semiconductor laser coupled to a distant saturable absorber. In a dissipative environment light bullets will be robust and individually addressable, thus allowing for three dimensional optical buffering of light bits.

### 3.2 Spatially extended or delayed systems

As described above, localized states can form in spatially extended media. However, we have recently been extending this idea to the case of *delayed* dynamical systems, which is a scheme which can be explored experimentally very conveniently with semiconductor lasers. In practice, the approach is to consider the semiconductor laser as a nonlinear node of essentially vanishing spatial extension (therefore, modeled as a low dimensional dynamical system) and to place in front of it a mirror that will reinject into the nonlinear node some of the light it has emitted some time before. Such a configuration can be conveniently modeled by adding to the nonlinear node a delayed term which represents this optical reinjection. It was shown many years ago [14] that a simple nonlinear node near a supercritical Hopf bifurcation can, in the presence of delayed feedback, give rise to convective-type instabilities and that large classes of delayed dynamical systems can be mapped onto an evolution rule for a spatially extended system with drift and diffusion. The extension of these results to other situations (vicinity of subcritical bifurcations for instance) is nontrivial and fascinating, with the observation in [15] of front dynamics very similar to those observed in spatially extended media. In [16,17], we have demonstrated experimentally that repulsive front interactions, which would normally lead to one phase filling the whole delayed system, can be tamed by pinning fronts to a temporal modulation. We have developed similar arguments in the neighborhood of a saddle-node on a circle bifurcation, *i.e.*, in a case where the nonlinear element is a "neuron-like" *excitable* node, subject to a delayed retro-action. In that case, we have observed attractive and repulsive interactions as well as elastic collisions of localized states of light [18,19]. Although mathematical demonstrations are lacking, our results strongly suggest that very similar mechanisms of homoclinic snaking can be invoked to describe the stability property of localized states in spatially extended and delayed systems.

## 4 Conclusion

In the preceding pages we have briefly reviewed some recent research topics that can be conveniently addressed using semiconductor lasers as an experimental platform. Of course, the ideas put forward here are far from exhaustive and many other general phenomena can be studied on these devices. Due to the typical time scales of semiconductor lasers (nanosecond and below), very large experimental data sets can be collected relatively easily, rendering these experiments particularly appealing for the analysis of low- or high-dimensional chaos, synchronization, slow-fast dynamics, phase transitions, stochastic phenomena, dissipative solitons and rare or extreme events. In addition, the ubiquity of these devices in modern data transmission systems also make them ideal candidates for the design of novel data processing schemes, which leverage nonlinear optical dynamics. In this direction, the chase of light bullets as three dimensional light bubbles able to carry optical information, or the exploration of neuromimetic optical dynamics for bio-inspired optical information processing are current research projects at the Institut de Physique de Nice.

## References

1. V. Degiorgio and M.O. Scully. Analogy between the laser threshold region and a second-order phase transition. *Phys. Rev. A*, 2:1170–1177, 1970.
2. T. Wang, G.P. Puccioni, and G.L. Lippi. Dynamical buildup of lasing in mesoscale devices. *Sci. Rep.*, 5:15858, 2015.
3. G.P. Puccioni and G.L. Lippi. Stochastic simulator for modeling the transition to lasing. *Opt. Express*, 23:2369–2374, 2015.
4. T. Wang, G.P. Puccioni, and G.L. Lippi. Threshold dynamics in meso- and nanoscale lasers: why vertical cavity surface emitting lasers? *Proc. SPIE*, 10682:106820Q, 2018.
5. Zoltán Néda, Erzsébet Ravasz, Yves Brechet, Tamás Vicsek, and A-L Barabási. Self-organizing processes: The sound of many hands clapping. *Nature*, 403(6772):849, 2000.
6. Alan Mathison Turing. The chemical basis of morphogenesis. *Philosophical Transactions of the Royal Society of London. Series B, Biological Sciences*, 237(641):37–72, 1952.
7. Mark C Cross and Pierre C Hohenberg. Pattern formation outside of equilibrium. *Reviews of modern physics*, 65(3):851, 1993.
8. P. Couillet. Localized patterns and fronts in nonequilibrium systems. *International Journal of Bifurcation and Chaos*, 12(11):2445–2457, 2002.
9. Mustapha Tlidi, K Staliunas, Krassimir Panajotov, AG Vladimirov, and MG Clerc. Localized structures in dissipative media: from optics to plant ecology, 2014.
10. S. Barland, J. Tredicce, M. Brambilla, L. A. Lugiato, S. Balle, M. Giudici, T. Maggipinto, L. Spinelli, G. Tissoni, T. Knödel, M. Miller, and R. Jäger. Cavity solitons as pixels in semiconductor microcavities. *Nature*, 419:699–702, 2002.
11. P. Genevet, S. Barland, M. Giudici, and J.R. Tredicce. Cavity soliton laser based on mutually coupled semiconductor microresonators. *Physical Review Letters*, 101(12):123905, 2008.

12. P Camelin, J Javaloyes, M Marconi, and M Giudici. Electrical addressing and temporal tweezing of localized pulses in passively-mode-locked semiconductor lasers. *Physical Review A*, 94(6):063854, 2016.
13. M. Marconi, J. Javaloyes, S. Balle, and M. Giudici. How lasing localized structures evolve out of passive mode locking. *Physical Review Letters*, 112(22):223901, 2014.
14. Giovanni Giacomelli and Antonio Politi. Relationship between delayed and spatially extended dynamical systems. *Physical review letters*, 76(15):2686, 1996.
15. Giovanni Giacomelli, Francesco Marino, Michael A. Zaks, and Serhiy Yanchuk. Coarsening in a bistable system with long-delayed feedback. *EPL (Europhysics Letters)*, 99(5):58005, 2012.
16. Francesco Marino, Giovanni Giacomelli, and Stephane Barland. Front pinning and localized states analogues in long-delayed bistable systems. *Phys. Rev. Lett.*, 112(10):103901, Mar 2014.
17. Francesco Marino, Giovanni Giacomelli, and Stephane Barland. Splitting in the pinning-depinning transition of fronts in long-delayed bistable systems. *Phys. Rev. E*, 95(5):052204, May 2017.
18. Bruno Garbin, Julien Javaloyes, Giovanna Tissoni, and Stéphane Barland. Topological solitons as addressable phase bits in a driven laser. *Nature communications*, 6, 2015.
19. B. Garbin, J. Javaloyes, S. Barland, and G. Tissoni. Interactions and collisions of topological solitons in a semiconductor laser with optical injection and feedback. *Chaos: An Interdisciplinary Journal of Nonlinear Science*, 27(11):114308, 2017.



# Index of keywords

Actinides .....	53	Ecosystems .....	123
Adaptive dynamics .....	123	Elastica .....	9
Agent-Based Modelling .....	146	Electromagnetic .....	87
Anisotropy .....	9	ElectroMagnetic Compatibility .....	87
Archaeology .....	146	Evolutionary stable strategies .....	123
Atmospheric jets .....	69	Experimental predictions .....	35
Atoms .....	59	Flow chemistry .....	77
Averaging .....	105	Geometric approach .....	9
Bifurcations .....	35	Geophysics .....	25
Biophysical modelling .....	35	Gibbs distributions .....	35
Bubble formation .....	45	Heat flux .....	17
Buckling .....	9	Honeycomb-like material .....	9
Capillary Equation .....	45	Instabilities .....	165
Chaotic cavity .....	87	Interpolation .....	1
Chaotic systems .....	25	Kinetic theory .....	95
Coherence between ground states ..	117	Kinetics of aggregation .....	155
Cold atoms .....	117	Laser .....	133, 165
Collective phenomena .....	165	Light modulation .....	133
Collisional relaxation .....	95	Line arrangement .....	1
Complex systems .....	146	Long Period Fibre Grating .....	17
Condensed matter .....	59	Long range interactions .....	95
Cubesat .....	133	Macromolecular synthesis .....	53
Data analysis .....	35	Macromolecules .....	53
Data assimilation .....	25	Magnetic nanoparticles .....	155
Data rate .....	133	Magnetic separation .....	155
Delayed systems .....	165	Meteorology .....	25
Dynamic stability .....	123	Microfluidics .....	155
Dynamical systems .....	35	Millifluidic technology .....	77
Ecological diversity .....	123		

Minimum time	105	Retina	35
Multicatalysis	77	Retroreflector	133
Multilevel splitting algorithms	69	Reverberation chamber	87
Multistability	165	Reversible Compression	9
		Roman period	146
Nanoparticles	53	Satellite	133
Natural selection	123	Self-organization	117
Nonlinear optics	69	Semiconductor lasers	69, 165
Nuclear toxicology	53	Sensors	17
Nudging	25	Settlement dynamics	146
		Slow-fast control systems	105
Oceanography	25	Socio-environmental interactions	146
ODE	123	Splines	9
One-pot synthesis	77	Splitting type	1
Optical Fibre	17	Statistical physics	35, 95
Optical rogue waves	69	Strongly correlated systems	59
Optomechanical self-organization	117	Student project	133
Organic chemistry	77	Superfluids	59
Organic synthesis	77	Sustainable chemistry	77
Out of equilibrium physics	69	Symmetry breaking	9
		Tandem reaction	77
Parameter estimation	25	Telecommunications	133
Patch antenna	133	Telescope	133
Patterns	117, 165	Temperature	17
Photonics	17, 165	Ultracold gases	59
Photons	59	Vision	35
Physics	59	Weather forecast	25
Polycarbonate honeycomb	9	X-ray spectroscopy	53
Polynomial	1		
Projective plane	1		
Quasi-static compression	9		
Random matrix theory	87		
Rare and extreme events	69		

## Index of contributors

- A**
- Agabi, Karim ..... 133  
 Ait Lachgar, Essam ..... 133  
 Ajroud, Rami ..... 146  
 Amraoui, Samira ..... 25  
 Antoniotti, Sylvain ..... 77  
 Aubree, Flora ..... 123  
 Auroux, Didier ..... 25
- B**
- Baltazar, Danielle ..... 133  
 Barland, Stéphane ..... 165  
 Batrouni, George ..... 59  
 Beaulieu, Mathilde ..... 133  
 Benabdesselam, Mourad ..... 133  
 Benetti, Fernanda ..... 95  
 Bertoncetto, Frédérique ..... 146  
 Blum, Jacques ..... 25
- C**
- Caillau, Jean-Baptiste ..... 105, 133  
 Calcagno, Vincent ..... 123  
 Cauneau, François ..... 133  
 Cessac, Bruno ..... 35  
 Claudet, Cyrille ..... 155  
 Contreras, Daniel ..... 146
- D**
- Da Costa Pereira, Célia ..... 146  
 Dell'Elce, Lamberto ..... 105  
 Den Auwer, Christophe ..... 53
- Deneire, Luc ..... 133  
 Deroo, Mathis ..... 133  
 Di Giorgio, Christophe ..... 53  
 Dimca, Alexandru ..... 1
- E**
- Elizarov, Nelli ..... 77  
 Ezzaier, Hinda ..... 155
- F**
- Faugeras, Blaise ..... 25  
 Ferrero, Fabien ..... 133  
 Flottat, Thibaut ..... 59  
 Fox, Dennis ..... 146
- G**
- Galligo, André ..... 9, 45  
 Gao, Baolong ..... 133  
 Gieudes, Benjamin ..... 133  
 Giorgi, Pascal D. .... 77  
 Giudici, Massimo ..... 165
- H**
- Hanaki, Nobuyuki ..... 146  
 Hébert, Frédéric ..... 59
- I**
- Izmaylov, Yaroslava ..... 155
- J**
- Jiang, Meiyao ..... 133

**K**

Kaiser, Robin .....	117
Kuhl, Ulrich .....	87
Kuzhir, Pavel .....	155

**L**

Labeyrie, Guillaume .....	117
Lahrouch, Florian .....	53
Languery, Maxime .....	133
Lefebvre, Jérémy .....	146
Legrand, Olivier .....	87
Léost, Laurane .....	53
Lesage, Frédéric .....	17, 45
Lippi, Gian Luca .....	165
Livio de Miranda Pinto Filho, Tito ..	133

**M**

Maamri, Manel .....	133
Mady, Franck .....	133
Magnet, Cécilia .....	155
Marcos, Bruno .....	95
Marcotto, Aurélie .....	133
Marins, Jessica .....	155
Mary, David .....	133
Memin, Anthony .....	133
Metris, Gilles .....	133
Millour, Florentin .....	133
Minjeaud, Sebastian .....	45
Mortessagne, Fabrice .....	87

**O**

Ottogalli, Sébastien .....	133
----------------------------	-----

Oubaha, Khalid .....	87
Ouriachi, Marie-Jeanne .....	146

**P**

Petiot, Olivier .....	133
Pomet, Jean-Baptiste .....	105, 133
Preis, Olivier .....	133
Purdue, Louise .....	146

**R**

Rajchenbach, Jean .....	9
Rebeyrolle, Solène .....	133
Richter, Martin .....	87
Rolland, Lucie .....	133
Rouot, Jérémy .....	105
Rousselet, Bernard .....	9

**S**

Simonnet, Eric .....	69
Staraj, Robert .....	133
Stibbe, Arthur .....	133

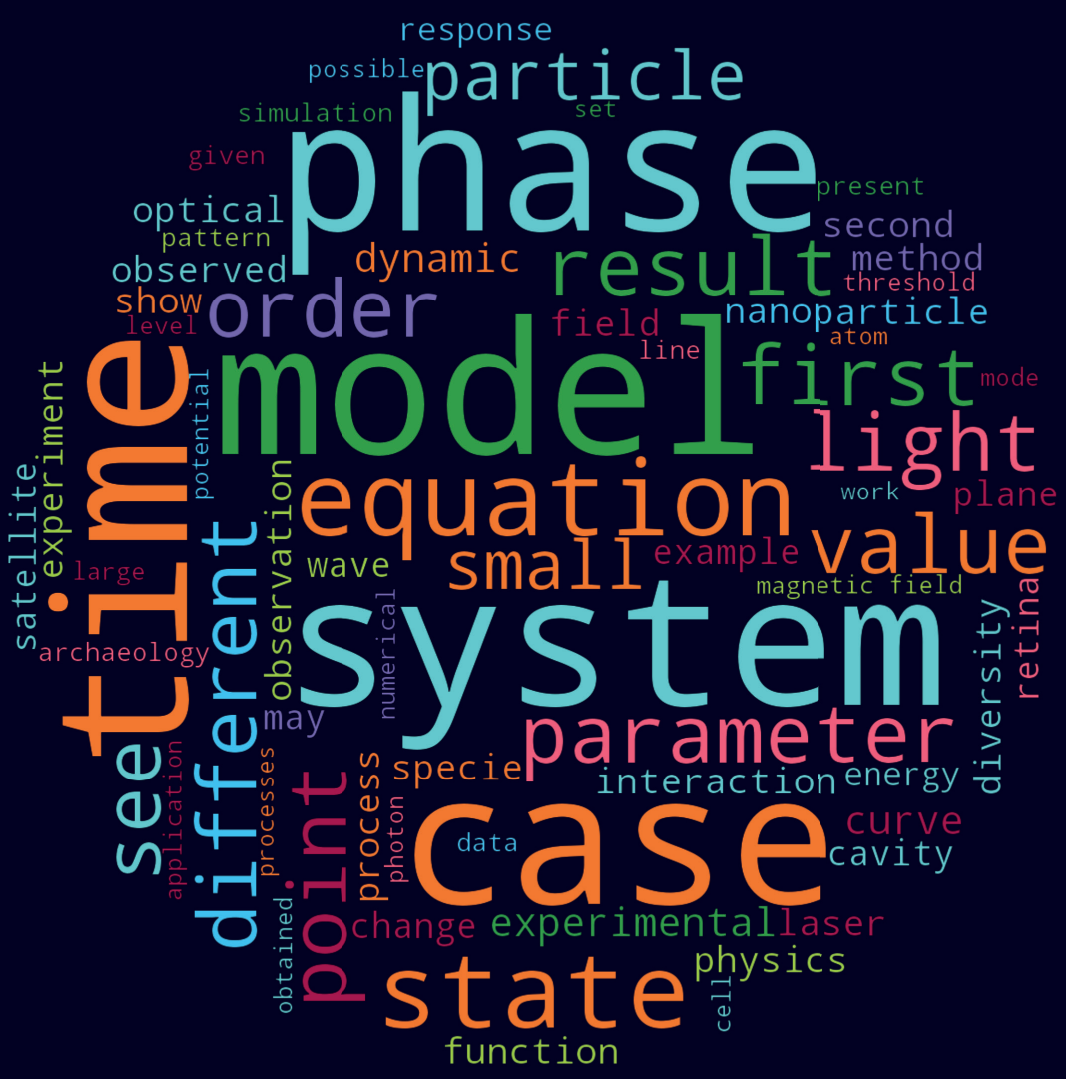
**T**

Tettamanzi, Andrea .....	146
Thevenon, Anthony .....	133
Tissoni, Giovanna .....	69

**Y**

Yeromina, Alexandra .....	77
---------------------------	----





Publisher: Université Côte d'Azur - Complex Systems Academy of Excellence, Nice  
 Printed by: Centre de Production Numérique Universitaire - Université Nice Sophia Antipolis  
 Avenue Joseph Vallot, 06103 Nice, France  
 First published: December 2018  
 Registration: December 2018  
 © Université Côte d'Azur - All rights reserved  
 Print ISBN: 978-2-9565650-0-0  
 ePDF ISBN: 978-2-9565650-1-7

